Project No. 09-779

Development of Diffusion Barrier Coatings and Deposition Technologies for Mitigating Fuel Cladding Chemical Interactions (FCCI)

Fuel Cycle R&D

Dr. Kumar Sridharan
University of Wisconsin, Madison

In collaboration with:
Idaho National Laboratory

Frank Goldner, Federal POC
James Cole, Technical POC

NEUP Nuclear Energy University Programs
U.S. Department of Energy

FINAL REPORT FOR NEUP PROJECT

PROJECT TITLE: DEVELOPMENT OF DIFFUSION BARRIER COATINGS AND DEPOSITION TECHNOLOGIES FOR MITIGATING FUEL CLADDING CHEMICAL INTERACTIONS (FCCI)

PROJECT ID: 09-779

PERIOD COVERING: 10/1/09 TO 9/30/12

Kumar Sridharan (PI), Todd Allen (Co-PI), Vahid Firouzdor (lead post-doctoral research fellow)
(University of Wisconsin)
James Cole (Idaho National Laboratory)

Students/Student Interns: Lucas Wilson, Jamieson Brechtl, Brandon Semerau, Ben Hauch, Ankita Bhutani, Hwasung Yeom

Project Contact: Kumar Sridharan
kumar@engr.wisc.edu

This Page Intentionally Left Blank

Executive Summary/Abstract

The Advanced Fuel Cycle Initiative (AFCI) is considering the Sodium-Cooled Fast Reactor (SFR), a fast neutron spectrum reactor for transmutation of spent nuclear fuel for reducing radiotoxicity and waste lifetime. Because of the higher dpa (displacements per atom) and temperatures encountered in SFR compared to light water reactors (LWR), higher conductivity metallic uranium-based fuels and ferritic-martensitic steel claddings have been selected for SFR. One of the significant challenges with this type of fuel-cladding combination is the inter-diffusion between the fuel and cladding material, particularly at the intended high burnup levels. This phenomenon known as fuel cladding chemical interaction (FCCI) can lead to the formation of lower melting point compounds at the fuel-cladding interface and a loss in effective thickness of the cladding wall. To mitigate FCCI, diffusion barrier coatings and liners are being considered. Research on such diffusion barrier materials have recently been performed at Idaho National Laboratory (INL) and Korea Atomic Energy Research Institute (KAERI).

The present project was aimed at developing nanofluid-based electrophoretic deposition (EPD) process for depositing candidate material diffusion barrier coatings. Nanofluid refers to suspensions of nanoparticles in a liquid medium. A wide range of coating materials were investigated including titanium-dioxide, yttria-stabilized zirconia (YSZ), vanadium-oxide, and pure metals titanium, zirconium, and vanadium. Limited studies were also performed with titanium-nitride deposition. A number of liquids for preparing suspensions were investigated, and a solution consisting of acetylacetone and additive triethanolamine showed most promising results. Coating structures and morphologies were examined in detail and optimized using a wide range of process parameters such as nanoparticle size and concentration, solution chemistry, and current and voltage settings. Post-coating sintering temperatures and times were investigated for promoting coating densification and interface bonding. YSZ, titanium-dioxide, and titanium formed the best coatings, however we have reported results with the other materials since they did show promise and warrant further investigation.

To evaluate the efficacy of these coating materials for FCCI mitigation, diffusion couple tests were performed with cerium as surrogate for uranium against both the steel and the coatings. These tests were performed at temperatures between 550°C to 600°C which is below the iron-cerium eutectic temperature. YSZ, titanium-dioxide, and titanium coatings exhibited excellent diffusion barrier performance as measured by inter-diffusion lengths using SEM-EDS analysis. Vanadium-oxide, vanadium, and zirconium, also provided indications of good diffusion resistance, but the results are not conclusive because of poor quality of the coatings. Nevertheless diffusion couple tests were performed with these coatings and we have reported these results as well.

An engineering challenge for developing coatings/liners for FCCI mitigation is the ability to deposit coatings on the inside surface of claddings which can be several feet in length and have an inner diameter as small as 4mm. One of the highlights of this project was to demonstrate that coatings could be successfully deposited on the inner surfaces of cladding geometries with the EPD process by using a co-axial electrode configuration and a flowing nanofluid.

Modeling of fuel center-line temperature changes as a result of coating addition were performed using two approaches. The initial configuration model which takes into account the presence of liquid sodium in the gap between the fuel and the cladding and the swelled fuel model that considers a scenario where the swelled fuel makes contact with the cladding after pushing away the liquid sodium. In both these cases it was determined that the fuel center-line temperature rises only marginally and should not be a concern. It is noted here that typical coating thicknesses being targeted were 5 μm to 10μm for oxide coatings and up to 25 μm for metallic coatings.

Finally, experiments were performed to deposit coatings using water-based nanofluid boiling approach. These studies, performed only with titanium-dioxide nanofluids, involved immersing

preheated samples in boiling nanofluid heated to various temperatures. Surface boiling leaves behind a coating deposit due to water evaporation. Particle size and concentration, sample/nanofluid temperature, and effects of hydrophobicity and hydrophilicity of the powders were investigated as variables in this study. While high deposition rates were achieved, the coatings were non-uniform and lacked the microstructural and structural integrity of the EPD coatings. We have reported these results because they may advance the understanding of the enhancements in critical heat flux of claddings' outer surface that have been observed in other studies.

The project has provided a rich scientific environment for training and educating students. Over the three-year term of the project two Masters degrees were awarded and four undergraduate students were involved in this project. A post-doctoral research associate was actively involved throughout the project. The personnel represented a mix of nuclear engineering and materials science and engineering backgrounds. The work was performed in collaboration with Idaho National Laboratory. The findings of this research are being disseminated quite extensively in the scientific community in forums such as *The Metallurgical Society Conference* and *DoE-NE* meetings, and scientific journals. We will continue to publish and present this work in the coming years. A list of these publications and presentations at the time of this report is listed below:

Publications:

"Development of Diffusion Barrier Coatings for Mitigation of Fuel-Cladding Chemical Interactions", V. Firouzdor, L. Wilson, K. Sridharan, B. Semerau, B. J. Hauch, J. Brechtl, and T.R. Allen, *Key Engineering Materials*, vol. 507, 2012, p.3.

"Development Protective Pure Titanium Coating using Electrophoretic Deposition Method for Mitigation of Fuel-Cladding Chemical Interactions", V. Firouzdor**,** J. Brechtl, L. Wilson, B. Semerau, K. Sridharan, and T.R. Allen, *Surface and Coating Technology*, accepted (in press).

"Development of Diffusion Barrier coating using Electrophoretic Deposition of Yitria-stablized Zirconia (YSZ) for Mitigation of Fuel-Cladding Chemical Interactions", V. Firouzdor**,** J. Brechtl, L. Wilson, B. Semerau, K. Sridharan and T.R. Allen, *Journal of Nuclear Materials*, accepted (in press).

"Electophoretic Deposition of Diffusion Barrier Titanium Oxide Coatings for Mitigation of Fuel-Cladding Chemical Interactions", V. Firouzdor, J. Brechtl, L. Wilson, B. Hauch, K. Sridharan, and T.R. Allen, to be published.

Presentations:

"Development of Diffusion Barrier Coatings and Deposition Technologies for Mitigating Fuel Cladding Chemical Interactions", *Fuel Cycle Research and Development Conference*, Gaithersburg, MD, October 2010 (invited talk given by PI).

"Development of Diffusion Barrier Coatings for the Mitigation of Fuel-Cladding Chemical Interactions (FCCI)" presented at the International conference on Electrophoretic Deposition, Puerto Vallarte, Mexico (2011) and The Metallurgical Society (TMS) Annual Conference, Orlando, FL (2012).

Work cited at the planning meeting for "*Coatings for Claddings Workshop*" held at Oak Ridge National Laboratory, February, 2012.

We thank the U.S. Department of Energy-NE (NEUP program) for providing funding for this project.

TABLE OF CONTENTS

I. INTRODUCTION AND RESEARCH MOTIVATION…….. 1

II. ELECTROPHORETIC DEPOSITION (EPD) PROCESS……. 3

II.A. EPD Coating of Oxides……. 3

II. B. EPD Coatings of Specific Materials…….. 6

Titanium Oxide Coatings…….. 6

Yttria-Stabilized Zirconia (YSZ) Coatings…….. 7

Vanadium Oxide Coatings……. 9

Metallic Coatings……. 9

III. EXPERIMENTAL SYSTEMS USED IN THE PRESENT RESEARCH……. 10

III.A. EPD of Flat Samples……. 10

III.B. Coaxial Configuration for Depositions on the Inner Surface of Cladding Sections…….. 11

IV. SAMPLE PREPARATION AND PREPARATION OF NANOFLUIDS…….. 12

V. GENERAL DEPOSITION PROCEDURES……. 14

VI. Diffusion Couple Studies……. 14

VII. RESULTS AND DISCUSSION……. 16

VII. A. Temperature Constraints on T91 Steel…….. 16

VII.B. Electrophoretic Deposition……. 17

Titanium Dioxide Coatings……. 17

Yttria-Stabilized Zirconia Coatings…….. 31

Vanadium Oxide Coatings……. 40

Titanium Coatings……. 43

Zirconium Coatings……. 51

Vanadium Coatings……. 53

Titanium Nitride Coatings……. 57

VII.C. Electrophoretic Deposition on the Inner Surface of Cladding Sections using the Coaxial Electrode Configuration…….. 59

VII.D. Diffusion Couple Experiments……. 60

Initial Experiments…….. 60

Titanium Dioxide Coatings…… 63
Yttria-Stabilized Zirconia Coatings…… 66
Vanadium Oxide Coatings…….. 69
Titanium Coatings…… 71
Zirconium Coatings…….. 73
Vanadium Coatings…….. 76
VII.E. Thermal Models…….. 79
Basic Approach…….. 79
Initial Configuration Model…… 81
Swelled Fuel Model…… 81
Results of Modeling…… 82
VII.F. Nanofluid Boiling Experiments to Prepare Coatings…….. 85
VIII. REFERENCES CITED…… 90

I. Introduction and Research Motivation

The major goals of United States Advanced Fuel Cycle Initiative (AFCI) are the development of (i) reprocessing technologies that separate all transuranic elements and (ii) advanced burner reactors (ABR), a fast reactor that consumes these reprocessed fuels while generating power. The main objective of these programs is to reduce the radiotoxicity, decay heat, and volume of waste generated that needs long term geologic storage.

The Sodium Cooled Fast Reactor (SFR) is one type of Gen IV reactor design that has the capability to transmutate nuclear waste [1, 2]. The SFR system features a fast-spectrum, sodium-cooled reactor and a closed fuel cycle for efficient management of actinides and conversion of fertile uranium. One of the most appealing aspects of SFR is its fast neutron spectrum (≥1MeV neutron energy). Current light water reactors operate in the thermal neutron spectrum (~0.025MeV). A fast neutron reactor can reduce the total radiotoxicity of nuclear waste, and dramatically reduce the waste's lifetime from tens of millennia (from transuranic isotopes) to a few centuries. This is because the neutron absorption cross-section of the long-lived transuranics increases significantly in a fast neutron spectrum compared to a thermal spectrum. Once the neutrons are absorbed, the probability of fission increases significantly. Thus, the fission products that are shorter lived exhibit less total radiotoxicity.

Sodium coolant also has several safety advantages over current light water reactors. The sodium coolant has high thermal conductivity, allowing the fuel to remain at low operating temperatures. Unlike water-cooled reactors, sodium reactors operate at near atmospheric pressure, and therefore with increased safety. The passive safety features of SFR have been demonstrated by tests performed at the Experimental Breeder Reactor 2 (EBR II) test program at Idaho National Laboratory (INL). In the first test, the main primary cooling pumps were shut off with the reactor at full power. In the second test, flow in the secondary cooling system was stopped again with the reactor at full power. In each instance, the reactor shut itself down without human intervention. These tests show that a SFR will shut down using inherent features of the reactor which are independent of human controls.

Metallic fuels are being considered as fuel for SFR. They have high thermal conductivity, proliferation resistance, and good compatibility with sodium, and are easier to fabricate. Ferritic-martenistic steels are the choice of material for cladding [3]. These steels have good swelling resistance up to 200 dpa, have high thermal conductivity and low thermal expansion coefficient. HT9 has been adopted for the US fast reactor program, but newer materials such as T91, T92, and ODS steels have also shown promising results. HT9, for example, allows for fuel irradiation to burnups greater than 200 GWd/MTHM (or 20 at%). A crucial concern here however is the reaction between actinide elements in a metallic fuel such as uranium and plutonium and the inner surfaces of the ferritic–martensitic steel cladding [4, 5]. This phenomenon is known as Fuel Chemical-Cladding Interaction (FCCI) and is accompanied by the formation of lower melting point eutectic compounds. For example, eutectic regions form above 650ºC in the U-Pu-Fe system and 725ºC in the U-Fe system. Additionally, FCCI reduces the effective cladding thickness so that the mechanical integrity of the cladding gradually decreases as burnup increases. This decreases the structural strength limits over the lifetime of the fuel.

To mitigate FCCI, a barrier liner or coating, which prevents both the fuel and cladding elements from inter-diffusing has been proposed. Researchers at Korea Atomic Energy Research Institute (KAERI) have performed two studies where diffusion couples were performed with elemental diffusion barriers [4, 5]. In each case a F/M steel was coupled with U-Zr at 800ºC for 25 hours. This is above the normal operating temperature of 650ºC and the higher temperature was selected to evaluate the diffusion characteristics in a relatively short period of time and to simulate conditions in the presence of plutonium.

In the first study, 20-30 µm foils of Zr, Nb, Ti, Mo, Ta, and V were tested as the candidate materials for diffusion barrier. These studies showed that vanadium acted as an excellent diffusion barrier while zirconium and titanium performed poorly. The unreacted thickness of vanadium after annealing was 23 µm (initial thickness 26µm) whereas the uranium diffused completely through the 25 µm titanium and zirconium foils. However, recent studies at INL using cerium or lanthanum as surrogates for uranium have shown zirconium to be a promising candidate barrier material. These results can be explained by examination of the binary phase diagrams of the foil/uranium system and the solubility of uranium in the barrier elements. The ideal diffusion barrier should have low uranium solubility, not form intermediate phases with uranium, and not have a eutectic melting temperature lower than the Fe-U eutectic temperature. Neither titanium nor zirconium form eutectic compounds with uranium. The V–U binary system has a eutectic point at 1040°C, which is much higher than the Fe-U eutectic point. The solubility of uranium in vanadium is lower than 4 wt% at about 800ºC, whereas uranium has extended solubility in zirconium and titanium. This solubility analysis explains why the titanium and zirconium performed poorly.

In the second study, the researchers performed similar experiments with multiple layers of vapor deposited zirconium, a mix of zirconium and chromium, and a mix of zirconium and chromium with a thin 150 nm layer of titanium to act as a buffer layer. The total thickness was 6 µm in each case. As in the previous studies, the uncoated samples showed severe diffusion, but this was mitigated by the 6 µm zirconium layer. Without coating, several phases were formed on the fuel side including $U(Fe,Cr)_2$ and $Zr(Fe,Cr)_2$ and other intermediate phases. There were also traces of uranium and zirconium on the steel side and the entire diffusion length was nearly 1 mm. These phases were not present with the zirconium coated sample. After diffusion, the barrier remained 90% zirconium, with traces of uranium, iron, and chromium. 1.2% zirconium was found in the steel, but uranium was less than 1%. This study concluded that vapor deposited zirconium is a good diffusion barrier.

With the above background, this project was aimed at developing and investigating the nano-fluid based electrophoretic deposition process for the deposition of thin oxide and metallic diffusion barrier coatings on T91 ferritic steel steel substrates. Diffusion couple tests using cerium as surrogate for uranium, were used to evaluate the efficacy of these materials as diffusion barriers. One of the engineering limitations of many coating processes is that they are line-of-sight and cannot be used to effectively deposit coatings on the inside surfaces of long tubular cladding geometries. We have demonstrated that it is possible to uniformly coat the inside surfaces claddings using the nano-fluid based electrophoretic deposition process.

II. ELECTROPHORETIC DEPOSITION (EPD) PROCESS

II.A. EPD Coating of Oxides

Electrophoretic deposition (EPD) is a colloidal processing technique which has been used to fabricate solid oxide fuel cells (SOFC), micro-laminate and functionally graded materials, ceramic matrix/ceramic-fiber composites [6], porous layers as membranes [7], and thermal barrier coatings [8]. EPD is similar in many ways to electroplating, with the difference that electroplating uses an ionized solution whereas EPD uses a colloidal suspension comprised of small particles (≤ 200nm) of the coating material dispersed in a liquid. As a result of certain additives in the liquid, the nano-particles acquire a surface charge in the colloidal suspension and are directed and deposited on an electrode by an electric field. A schematic illustration of the EPD process is shown in Figure 1. In keeping with terminology used in recent literature we define nanofluid as a fluid with a homogeneous dispersion of nanoparticles.

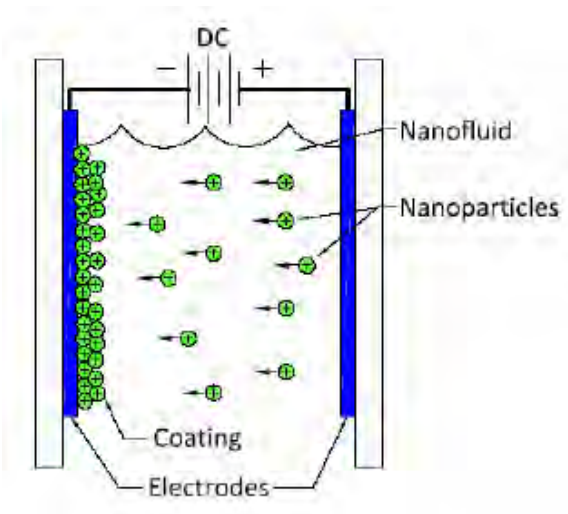

Figure 1. A schematic of electrophoretic deposition (EPD) process.

Electrophoretic deposition combines two processes: electrophoresis and deposition. During electrophoresis charged particles suspended in a solvent are accelerated under the influence of an electrical field toward an electrode of opposite polarity. During deposition, the particles assemble on the electrode to form a coating [6, 9, 10-13]. All colloidal particles that can form stable suspensions and carry charge can be used for electrophoretic deposition. This includes materials such as polymers, pigments, dyes, ceramics and metals. Homogeneous deposits with high mechanical strength and low surface roughness can only be obtained by using well dispersed suspensions [14].

Water is not commonly used as a solvent as it undergoes hydrolysis when more than 1.2 V is applied. Hydrolysis, the splitting of water into its components hydrogen and oxygen, causes gas evolution at the electrodes which is inevitable at field strengths high enough to produce coatings in reasonable times. This causes bubbles to be trapped within the deposit unless special procedures are adopted [15]. For these reasons, organic solvents are commonly used for electrophoretic deposition.

According to the Darjanguin, Laundau, Verway and Overbeek (DVLO) theory, the stability of a colloid depends on the balance of all forces and the total potential energy of particle interactions [16]. Therefore, in order to obtain a stable colloid, a high surface charge/zeta potential is required to induce a high repulsive force between particles [17, 18]. Zeta potential is the electrokinetic potential in colloidal systems. From a theoretical standpoint, the zeta potential is the electrical potential at the interfacial double layer (DL), i.e. the location of the slipping plane relative to a point in the bulk fluid away from the interface. In other words, this is the potential difference between the dispersion medium and the stationary layer of fluid attached to the dispersed particle [17, 18]. A general, but simplified equation for the weight of coating deposited, w, in an EPD process as first determined by Hamaker is as follows [19]:

$$w = f\frac{2}{3}C\varepsilon_0\varepsilon_r\zeta\left(\frac{1}{\eta}\right)\left(\frac{E}{L}\right)t \qquad \textbf{Equation (1)}$$

In this equation "C" is the particle concentration, "ε_0" the permittivity of free space, "ε_r" the relative permittivity of the solvent, "ζ" the zeta potential, and "f" the related correction factor with a value between 0 and 1 accounting for the fact that not all particles brought to the electrode are incorporated in the deposit. "η" is the viscosity of the suspension medium, "E" the applied electric field strength, "L" the distance between the electrodes and "t" is the deposition time [19].

Additives have been used in practice to stabilize colloidal suspensions. An additive can stabilize the suspension in two ways: steric repulsion and electrostatic stabilization. Steric repulsion involves adding polymers that adsorb onto the nanoparticles to prevent them from coming into close contact. At large separations, the van der Waals forces are too weak to cause agglomeration. Additives can also work through charge stabilization. This process works by the addition of a charged species to the mixture, thereby changing the concentration of ions in the system.

The more common method of stabilization is electrostatic (charge) stabilization, and it works in two ways. The additional charge adsorbed on the particles increases the repulsive energy between the particles which minimizes particle agglomeration. Also, since the particles are more highly charged, they will be more affected by the applied electric field. The particles in a nanofluid can acquire charge in four ways [20].

1. Selective adsorption of ions onto the solid particle from the liquid.
2. Dissociation of ions from the solid phase into the liquid.
3. Adsorption or orientation of dipolar molecules at the particle surface.
4. Electron transfer between the solid and liquid phase due to differences in work function forces between neighboring particles.

Several methods for charging oxides in organic solvents have been discussed in literature. In each case, a reaction occurs between the solvent and oxide particles or additive to cause the production of positive ions which in most cases are protons. These ions are then adsorbed onto the particle's surface and the charged particles are available to be influenced by the applied electric field and undergo electrophoresis.

The charging mechanisms of oxides (specifically yttria-stabilized zirconia, YSZ) in acetylacetone (ACAC) with additives have been explained by Xu et al. [21]. This study examined the EPD deposits with Fourier Transform Infrared Spectroscopy (FTIR) and showed that H_2O and CO_2 were present in these coatings. These compounds adsorbed on the particle surface from the atmosphere or trace impurities in ACAC and must be taken into account for the charge producing reactions. In a colloid with YSZ dispersed in ACAC, the dipole of the –OH group on the YSZ surface tends to capture protons from ACAC to form a positive charge on the particle surface, as shown in Equation (2). Moreover, the chemical reaction between YSZ and ACAC (Equation 3) is also thought to release a large number of protons. Both of these assist in creating a positive zeta potential for particles [21].

$$(Zr[-OH])_{surface} + CH_3COCH_2COCH_3 \rightarrow (Zr-OH_2)^+{}_{surface} + (CH_3CO)_2CH^- \quad \textbf{Equation (2)}$$

$$ZrO_2 + 4ACAC \rightarrow Zr(ACC)_4 + 2H^+ + 2OH \quad \textbf{Equation (3)}$$

The addition of acetic acid and triethanolamine (TEA) into acetylacetone suspensions has also been studied. The particle zeta potential increased through further adsorption of protons ionized by the acid. With the addition of TEA into the suspension, the lone pair of electrons on the residing nitrogen atom tend to capture H^+ from ACAC and form compounds $NH^+(CH_2CH_2OH)_3$ (equation 4) or $NH_2^{2+}(CH_2CH_2OH)_3$. This N–H bond was confirmed by FTIR. These radicals may tend to adsorb to YSZ particle surfaces, which would increase the particle surface charge and account for the high positive zeta potential in TEA containing suspensions. Thus, this study found that the addition of either organic acid or alkali both promoted positive zeta potentials resulting in the 'U'-shape trend of the ζ–pH relationship [21].

$$N(-R-OH)_3 + ACAC \rightarrow HN^+(-R-OH)_3 + ACAC^- \quad \textbf{Equation (4)}$$

Other groups have added iodine to organic suspensions. Chen and Liu [22] have studied the effect of iodine on acetone, acetylacetone, ethanol, and ethanol-acetone based suspensions. Ii was found that protons were produced when iodine reacted with acetylacetone (equation 5) and ethanol (Equation 6). Aruna and Rajam found that protons were also the product of the acetone-iodine reaction (Equation 7) [23].

$$CH_3CH_2COCH_2COCH_2CH_3 + I_2 \leftrightarrow ICH_2CH_2COCH_2COCH_2CH_2I + 2H^+ \quad \textbf{Equation (5)}$$

$$CH_3CH_2COCH_2COCH_2CH_3 + I_2 \leftrightarrow ICH_2CH_2COCH_2COCH_2CH_2I + 2H^+ \quad \textbf{Equation (6)}$$

$$CH_3COCH_3 + 2I_2 \leftrightarrow ICH_2COCH_2I + 2H^+ + 2I^- \quad \textbf{Equation (7)}$$

In addition to charge stabilization, steric stabilization inhibits the coagulation of suspensions. Usually steric additives are relatively long organic molecules that extend out into the solution. Steric effects arise from the fact that each atom within a molecule occupies a certain amount of space. If atoms are brought too close together, there is an associated cost in energy due to

overlapping electron clouds. In a sterically stabilized colloid, this energy offsets the van-der-Waals attractive forces, preventing coagulation [18]. Charge stabilization is more effective than steric stabilization for EPD because the charge gained on the particles promote stability and also allows particles to be more easily influenced by an applied electric field. A sterically stabilized solution can exist with little charge, and is therefore undesirable for EPD. Unfortunately, there is little literature on sterically stabilized organic suspensions used for EPD.

II. B. EPD Coatings of Specific Materials

Titanium Dioxide Coatings

Electrophoretic deposition of TiO_2 has been an area of interest in recent years and several experimental conditions have been used to successfully produce TiO_2 coatings. The most commonly used solvent in these studies was acetylacetone, but successful deposits were also achieved with acetone, isopropanol, ethanol, and methanol. Additives that have been used to stabilize the colloid suspension include: iodine, water, acetone, acetylacetone, and other organic molecules.

Boccaccini et al prepared TiO_2 coatings on three dimensional SiC fiber (Nicalon R-type) and carbon fiber substrates [24]. Colloidal suspensions of commercially available TiO_2 nanoparticles in acetylacetone with addition of iodine were used. The EPD parameters (i.e., deposition time and voltage) were optimized for each fiber type. Strongly adhered TiO_2 deposits with high particle packing density were obtained.

In the study by Kaya et al optimum deposition voltage of 10V and 2 minute deposition times were suggested for suspension of TiO_2 nanoparticles in acetylacetone with iodine additions [25]. Sintering at 800ºC for 2 hours resulted in TiO_2 coatings with uniform nonporous structure, with biomedical and photocatalytic applications, although the microstructural images do not show complete densification.

Moskalewicz et al deposited TiO_2 coatings on Ti-6Al-7Nb alloy substrates. The solvent solution used was acetylacetone additions of iodine [26]. The optimal concentration of the components in the solution was determined to be: TiO_2: 2g, iodine: 0.15g and acetylacetone: 200 ml. Detailed microstructural characterization performed on cross section thin foils by TEM revealed that the coating was composed of TiO_2 nano-crystals.

Santillan et al studied the effect of rheology of TiO_2 colloidal suspensions on the quality of coatings [27]. TiO_2 nanoparticle suspensions (concentration 0.3–2.5 wt%) in acetylacetone with and without iodine were used at different shear rates. For the suspension with 1 wt% TiO_2 containing iodine, a shear-thickening flow behavior was observed over the whole shear rate range investigated. The maximum solid fraction was experimentally determined from a linear relationship between solid concentration and viscosity. Using a suspension with 1 wt% concentration, high quality TiO_2 deposits on stainless steel planar substrates were obtained by EPD under constant voltage conditions. A pH of 5 was determined the optimum value in terms of suspension stability and coating quality.

Dor et al studied EPD of TiO_2 in methanol, ethanol, and isopropanol with small additions of acetylacetone, acetone, de-ionized water and iodine [28]. They showed that the zeta potential of all three suspensions was approximately +40 mV, indicating that the particles are positively charged implying stable suspensions. They also concluded that the density of the EPD coating decreases as the coating thickness increases, especially for coatings thinner than 10µm. The solvent used was shown to influence the deposition rate, but the solvent was not found to affect the density of the coating.

Wu et al studied the EPD of TiO2 particles in ethanol [29]. It was shown that the stabilization and charging of the nanoparticles in suspensions can be achieved using organic molecules, such as dopamine and alizarin yellow (AY) dye, which were adsorbed on the oxide nano-particles.

Yttria-stabilized Zirconia (YSZ) Coatings

There is ample literature on the EPD of YSZ because of its applications in fuel cell industry. YSZ can be used as a solid electrolyte, meaning that it conducts oxygen ions, but inhibits the transfer of electrons. In order to achieve a dense coating a number of solvents have been used including acetylacetone, ethanol, isopropanol, and n-propanol. Additives to promote EPD include water, phosphate ester, poly(vinyl butyral), acetic acid, and triethanolamine (TEA).

The EPD behavior of YSZ suspended in various ratios of ACAC and ethanol has been investigated by Xu et al [30]. Even though YSZ deposition on the substrate was achieved with all of the compositions of suspension solvents, microstructural studies of the deposited material suggest that depositions in the suspension with a 1:1 ratio of ethanol to acetylacetone produce the most homogeneously packed green deposits that will form dense coatings upon sintering at 1300ºC for 3 hours. At the low current densities used in this study (0.10 and 0.25 mA/cm2), changing the powder concentration for a given solvent did not generate an appreciable difference in deposition rates, even though a difference was observed at the higher current density of 0.40 mA/cm2.

In another study [21], the influence of pH on particle packing in YSZ coatings electrophoretically deposited from an ACAC based suspension was investigated. The pH of the suspension was adjusted by addition of acetic acid or triethanolamine (TEA) base. The adjustment of pH in YSZ–ACAC suspension was used to control the agglomeration of particles and suspension stability. The zeta potential increased with the addition of either organic acid or alkali and enhanced the repulsion between YSZ particles due to the adsorption of protons or alkali molecules, respectively. The increased electrostatic repulsion reduced the particle coagulation and stabilized the suspension. The suspension properties at different pH were explained by estimating the electrostatic interactions between particles. It was observed that suspensions with less particle agglomeration led to denser packing of particles.

Electrophoretic deposition experiments have been performed under constant voltage conditions from suspensions in ethanol, isopropanol, and mixed ethanol–isopropanol solvents by Zhitomirsky and Petric [31]. The use of phosphate ester as a dispersant enabled the formation of cathodic deposits from stable suspensions. Crack free and adherent deposits were

obtained using poly(vinyl butyral) additive. The electro-deposition process has been quantified in experiments performed at constant current and constant voltage modes, while varying the solvent content and concentration of the additives. A higher deposition rate was observed in ethanol compared to that in an isopropanol solvent. It was shown that the increase in concentration of dispersant and binder could result in a decreased deposition rate in the constant voltage mode due to an increase in suspension conductivity. These results were utilized for optimization of bath composition and deposit morphology and dense coatings were formed after sintering at 1300ºC.

Jia et al. reported the preparation of YSZ film by EPD for SOFC using isopropanol as solvent and iodine as dispersant [32]. Although the zeta potential of YSZ particles is only 2 mV in pure isopropanol, the value of zeta potential increased as the iodine concentration was increased and a maximum potential of 15 mV is attained at 0.5 g/l. This phenomenon suggests that protons (H+) are formed by the reaction between iodine and isopropanol as discussed in the previous section.

In the study conducted by Aruna and Rajam the EPD behavior of YSZ suspended in different ratios of acetone and ethanol with addition of iodine has been investigated [23]. It was noted that the suspension composition has a strong influence on the mass and nature of the deposit. All the compositions exhibited a maximum weight and hence maximum thickness for the deposits at 30V/cm except in pure acetone and pure ethanol. For pure acetone and ethanol, 20V/cm was sufficient to get a maximum deposit weight. Although YSZ deposition on the substrate was achieved with all of the compositions of solvent, microstructural studies of the deposited material suggest that depositions in the suspension with a 3:E and 2:2 ratio of acetone to ethanol produced homogeneously packed green films without cracks. Chen and Liu also reported the preparation of YSZ films on LSM ($La_{0.85}Sr_{0.15}MnO_3$) and LSM–YSZ substrates by EPD using acetylacetone, acetone, ethanol and mixture of acetone and ethanol [22].

Matsuda et al. fabricated bi-layered electrolytes using EPD of YSZ in ethanol followed by Sm_2O_3-doped CeO_2 (SDC) in phosphate ester (PE)-added ethanol onto the graphite coated NiO–YSZ substrate [33]. This same group has also reported direct EPD of YSZ electrolyte film onto porous NiO–YSZ substrate using ethanol as solvent [34]. Hosomi et al. reported the fabrication of YSZ electrolyte film on non-conducting porous NiO–YSZ composite substrate using acetone and ethanol solvents separately [35].

Besra et al. reported the EPD of YSZ on non-conducting porous NiO–YSZ substrate using ACAC as the solvent and a mechanism has been proposed for the deposition [36, 37]. The porous structure of the substrate allowed EPD to be performed even though the surface was non-conducting. Negishi et al. [38] demonstrated the feasibility of applying EPD technique to fabricate solid oxide fuel cells (SOFC) including preparation of one ended tubular lanthanum-manganite substrate and multilayers of anode/electrolyte/cathode as a single firing process. An acetone solvent with isopropanol or iodine addition was used to fabricate these coatings.

There are also reports on the deposition of YSZ powder suspended other solvents. Matsuda et al. and Hosomi et al. formed EPD deposits using n-propanol as a solvent [39, 40]. Wang et al.

have reported EPD of YSZ and aluminum using 1:1 ratio of ethanol and ACAC [41]. Basu et al. used glacial acetic acid as the solvent for the preparation of dense YSZ coatings by EPD on open end LSM (lanthanum strontium manganite) tubes [42].

Vanadium Oxide Coatings

Literature on EPD of vanadium-oxide coatings is more limited than the other oxide coatings. Shea et al. used an aqueous solution to electrophoretically deposit V_2O_3 onto HT9 steel substrates [43]. Menezes et al. used sol gel processing to produce the 15nm vanadium pentaoxide (V_2O_5) particles which were then deposited using EPD. The deposition occurred over a relatively long time period varying between 60 and 240 minutes. An ethanol solution was used to deposit V_2O_5 coatings that were approximately 1.5 µm in thickness [44].

Metallic Coatings

Although EPD of metals is not as common as ceramics, some relevant research has been performed in this area. Much of this research was performed decades ago, and the studies are not focused specifically on deposition of the metals desired for FCCI application such as zirconium, vanadium, or titanium.

Pearlstein et al. attempted EPD with mostly aluminum flake and powders (less than 44µm), as well as titanium and tungsten [45]. Several solvents were utilized, and aluminum deposits were formed from the following: chloroform, sec-butyl alcohol, butyraldehyde, tert-amyl alcohol, n-hexane, n-heptane, cyclohexane, ethylbenzene, toluene, xylene, monochlorobenzene, n-butylamine, and ethylene dichloride. The butylamine based colloid also produced deposits with the best physical strength and had the highest deposition rate. This group also produced pure titanium deposits from colloids composed of acetone with the addition of butylamine. Tungsten deposits could be formed from pure acetone based colloids.

Gutierrez et al. studied the deposition of several metals including B, Dy, Zr, Au, Nb, Mo, W, Re, and compounds NbSn, ZrH, ThC, UC, NpC, PuC, (ZrU)C, UWC, UO2, UMoC, TaO2, and both W-UO2, and Mo-UO2 composites [46]. This study concentrated on the deposition of Nb from a nitromethane suspension with addition of ammonium hydroxide. Benzoic acid and zein, a corn protein, was used as a binder to increase adhesion of the coating. It was claimed that zirconium was deposited from a similar solution, but the specific details were not provided.

Mizuguchi et al also performed studies on the electrophoretic deposition of metals [47]. W, Mo, Ni, A1, Zn, and Ru were successfully deposited from a colloid composed of particles suspended in acetone, nitrocellulose, and a small amount of strong base and strong acid. Nitrocellulose charges the particles through steric and charge stabilization, and also acts as a binder.

III. Experimental Systems used in the Present Research

III.A. EPD of Flat Samples

A simple apparatus was designed for successfully conducting EPD experiments and deposit coatings. The bulk of the apparatus is made of Teflon, which was held together by plastic screws. Platinum leads were run from the back through the apparatus to each of the electrodes as shown in Figure 2. This eliminated any effect of the charged wire on the EPD process. The platinum wire was wrapped around behind the electrodes. A good electrical connection was made when the electrodes are secured in place with the plastic screws. Slight adjustments were made to make this device more user-friendly. The sample and platinum electrode were then held in place by four screws. The top piece was removed and replaced with a spacer. This allows for quick sample changes with consistent separation distance.

(a) **(b)**

Figure 2. (a) EPD fixture for depositing coatings and (b) a close-up image showing the sample prior to deposition. Plastic screws secure the sample and force it to contact the platinum electrode wrapped behind the sample.

Smaller samples were needed for diffusion couple experiments as the diffusion couple fixturing device is limited to 7 mm diameter samples. For this, coatings were deposited on 7mm diameter steel substrates, and a slightly modified device was developed as shown in Figure 3. The same opposing electrode was utilized for the deposition on the diffusion couple samples.

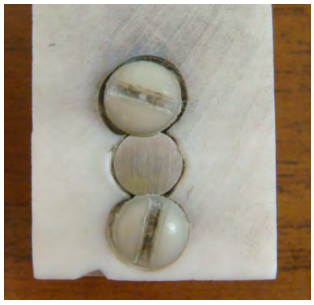

Figure 3. EPD fixture used for deposition on 7mm diameter diffusion couple samples.

III.B. Coaxial Configuration for Depositions on the Inner Surface of Cladding Sections

One of the highlights of this research was the use of EPD process for the deposition of coatings on the inner surface of claddings (i.e., non line-of-sight coatings). The initial plan was to submerge the cladding in a suspension, and the nano-particles would migrate into the cladding through holes in covers placed on either end of the cladding. This idea was abandoned because the migration rate would not be high enough to produce uniform coatings. The highly charged nano-particles would be consumed during deposition and the concentration would decrease significantly. To overcome this problem, we decided to flow the nanofluid through the cladding at a low flow rate, while using a co-axial electrode. The concept of this experimental design for co-axial configuration for the deposition of coatings on the inside surface of claddings is shown in Figure 4. A 2 mm diameter titanium electrode was used as the co-axial electrode.

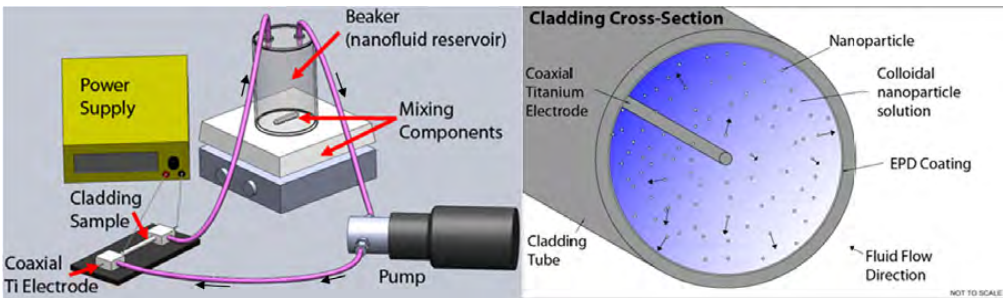

Figure 4. Design of coaxial electrode system for depositing coatings on the inner surface of claddings. The nanofluid pumped through the cladding.

Figure 5 and 6 show the two experimental designs used to deposit coatings using the co-axial electrode configuration. Figure 5 shows the initially experimented co-axial coating method. Here, the coating is applied while the cladding is horizontal, and the sample dried horizontally. These coatings were found to be non-uniform, with most of the deposit concentrated at the bottom of the cladding section. The thicker coating observed at the bottom was a result of sedimentation of nanoparticles by gravity. Therefore, it was decided to perform the experiment while positioning the cladding vertically (Figure 6. To reduce the effect of bubbles, the suspension flows from bottom to top. This provided significantly more uniform coatings.

The experiments in this study used commercial stainless steel tube as a substitute for the cladding with inner and outer diameter of 4mm and 6mm, respectively (very similar to the ABR cladding dimensions). Since EPD coating is an overlay coating, it is assumed the differences between this stainless steel material and the actual ferritic-martensitic steel will be a non-issue. Using a commercially available steel tube with dimensions similar to the cladding allowed us to perform a large number of experiments economically while establishing the proof-of-principle of the coating process on the inner surface of claddings. A titanium rod (2 mm diameter) was used as the co-axial cathodic electrode. Titanium is much less expensive than platinum and because a rigid cathode is necessary for this application, platinum would not be the optimal choice.

In order to investigate the longitudinal uniformity of coatings more easily, the steel tubes were bisected length-wise by EDM process prior to deposition. The two halves were sealed together using Teflon and electrical tape for the deposition and once the deposition was complete, the

two halves were separated for examination of the uniformity of the coating along the cladding length. This approach allowed for quick investigation to examine the quality and uniformity of the coating along the length of the cladding section. A photograph of a 12 inch section of EDM cut steel is shown in Figure 7.

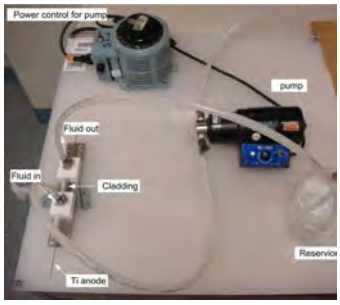

Figure 5. Coaxial system in the horizontal configuration. Coatings deposited and dried in this manner resulted in non-uniform deposits.

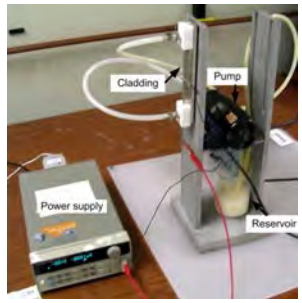

Figure 6. Coaxial system in the vertical configuration. Coatings formed in this manner resulted more uniformed deposits.

Figure 7. EDM cut uncoated simulated cladding section about 12” in length. Cladding was bisected prior to coating deposition so that it could be quickly and easily separated to examine coating uniformity along its length.

IV. Sample Preparation And Preparation of Nanofluids

The samples used for this study were commercial grade T91 (American Alloy and Steel) or HT9 (Idaho National Lab). The flat substrates were EDM cut (Xact Wire EDM Corp.) to dimensions 1/2”x1/2”x1mm. The front and back were then polished to 320 grit with the edges being polished to 1200 grit. The edges were polished to allow SEM investigation to measure the thickness and qualify uniformity of thickness. 316 stainless steel tubing (Grainger) with inner diameter of 4mm and outer diameter of 6mm was used as mimic SFR cladding for coaxial depositions.

The powders used in this study were procured from various vendors including NanoAmor (U.S.), MK Nano (Canada), and EV Nano Technologies (China). Details of each type of powder investigated are listed in Table 1. Solvents and additives to prepare nanofluids were procured through companies, VWR or Fischer Scientific (details in Table 2).

Table 1. Nanoparticle materials and sizes investigated in the present research.

Powder	Particle Size (Claimed)	Purity	Supplier
Titanium	30-50nm APS	99%	NanoAmor
Titanium	60-80nm APS	99%	SS Nano
TiN	20nm	97%	NanoAmor
TiO_2 Anatase	15nm	99%	NanoAmor
TiO_2 Rutile	50nm	99%	MK Nano
TiO_2 Anatase	50nm	99%	MK Nano
TiO_2 Rutile	250nm	99.97%	MK Nano
Zirconium	80nm APS	99.9%	EV Nano Technology
YSZ (8mol% Y_2O_3)	20-30nm	99.9%	NanoAmor
YSZ (8mol% Y_2O_3)	200-300nm	99.9%	NanoAmor
Vanadium	100nm APS	99.9%	EV Nano Technology
V_2O_3	20-40nm APS	99.5%	NanoAmor
Fe_3O_4	15-20nm APS	99.5%/98%	NanoAmor

Table 2. Solvents and additives used to prepare nanofluids investigated in the present research.

Solvent/Additive	Company	Vendor
Acetylacetone (ACAC)	TCI America	VWR
Acetone (AC)	Fisher Scientific	Fisher Scientific
Ethanol	Fisher Scientific	Fisher Scientific
Triethanolamine (TEA)	Fisher Scientific	Fisher Scientific
Acetic Acid (HAc)	Acros Organics	Fisher Scientific
Iodine (I_2)	Acros Organics	Fisher Scientific

Standard nanofluids were produced by mixing 40 ml of the desired liquid and additive with 0.2 grams of the nanopowder, resulting in a powder concentration of 0.5wt% (weight powder/volume solvent). This solid concentration was modified slightly during some experiments. An analytical balance (Ohaus Adventurer Pro Analytical Balance AV64) with accuracy of 0.1mg was used to measure the mass of the powders and solid additives (iodine). Initially, the mixing procedure utilized a bath sonicator or magnetic stirrer. As the project progressed, a probe sonicator was purchased (Misonix 4000). Mixtures were sonicated for 15 minutes at in a cooling pool prior to experiments. The suspensions were allowed to cool to room temperature before depositions commenced. The pH of selected mixtures was measured prior to depositions (Mettler Toledo SevenGo pH). The pH was not measured for several organic solvents because the hydrogen concentration (pH) loses its validity as a general measure for the acidity or alkalinity of an organic medium.

Though EPD has been performed with solid loading as high as 25g/l, a more dilute solution was desired for this application to allow easy flow through the pump and cladding sections. For

this reason, a 5g/l (0.2g powder/40ml solvent) suspension was used for most experiments. In the study of TiO_2, deposition parameters it was also found that the quality of coatings is not significantly affected by the concentration of nanoparticles. The suspensions that produced the optimum coatings on flat samples were used for the co-axial configuration cladding depositions. The applied voltage was more limited in these depositions due to the increased deposition area and current constraints of the power supply. Voltage of 20-40V was applied for 2-6 minutes. The suspensions for co-axial depositions were produced in the same manner, except with 300 ml of liquid rather than 40 ml.

V. General Deposition Procedures

After a few initial experiments an appropriate power supply (Agilent model 6614C DC power supply, Figure 8) was purchased along with the required data acquisition system and computer interface. This Agilent power supply has the ability to operate in either constant current or constant voltage mode and has a range from 0-100 V and 0-0.5 A with accuracy of approximately 50 mV and 4 μA. The power supply was interfaced with a computer and displays the current or voltage as a function of time using a LabView program. The applied voltage and deposition time parameters were adjusted using the computer interface.

Figure 8. Agilent power supply used to apply voltage and current during the EPD process.

Once the deposition was complete, the sample was carefully removed and allowed to dry in the atmosphere for several minutes. When the sample was visibly dried, it was heated to 100ºC for one hour to remove the organic compounds, and then sintered at higher temperatures if desired.

VI. Diffusion Couple Studies

Kovar diffusion couple fixturing device was obtained from Idaho National Lab (Figure 9). For each experiment, a thin (250 μm) cerium piece was sandwiched between two 7mm diameter, 1 mm thick T91 steel samples. Cerium was used as surrogate for uranium. One of these samples was coated and the other was left uncoated so that diffusion characteristics could be compared directly by measurements of relative diffusion lengths. Cerium was polished with 320 grit paper to remove the oxide layer immediately before assembly. Silicon carbide spacers were used to prevent inter-diffusion between samples and the Kovar fixture. A pressure of 8in-lbs was applied with the use of a torque wrench (Proto 577-6106 Torque Screwdriver, procured for this study). This torque translates to approximately 188kg/cm^2 force on the sample. Figure (9b) shows the

diffusion couple and sample configuration. The parameters are similar to those used at INL for their diffusion couple experiments.

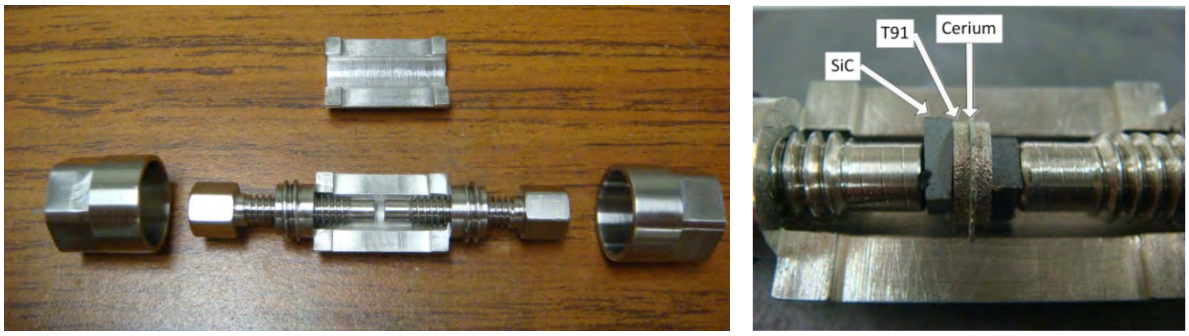

(a) **(b)**

Figure 9. (a) Photograph of the diffusion couple device used in this study. The screws tighten to apply pressure on the sample using a torque wrench and (b) close-up photograph showing how the cerium is sandwiched between two steel samples.

Once the diffusion couple was assembled, it was encapsulated in a Pyrex tube and sealed under vacuum. To reduce oxidation effects, zirconium sponge was placed in the encapsulation to absorb any remaining oxygen. Figure 10 shows the final assembly which was placed in a high vacuum (10^{-5} Torr) furnace. Diffusion couple experiments with coated samples were conducted at either 550ºC for 100 hours or 585ºC for 40 hours.

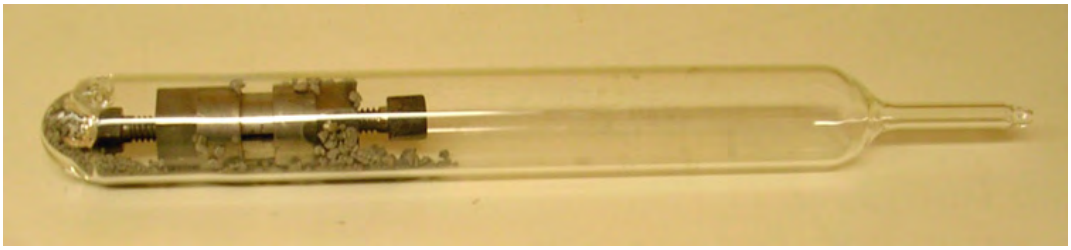

Figure 10. Diffusion couple encased under vacuum in a Pyrex tube. Zirconium sponge is used to absorb any extra oxygen.

Because cerium was used as a surrogate for uranium in the current study, it was important to determine its behavior compared to uranium or plutonium used in the reactor system. The phase diagrams for Fe-U and Fe-Ce are shown in Figure 11a and 11b, respectively. Other researchers have performed diffusion couple experiments with uranium at 800ºC for 25 hours. According to Figure 11a, this is about 80ºC above the lowest temperature eutectic composition. Operating above the eutectic composition was not acceptable in this study as an uncoated sample was used in each experiment as a reference and liquation would render the experiments invalid. For this reason, it was decided to stay below the iron-cerium eutectic temperature. In the iron-cerium system, the lowest eutectic compound forms at 592ºC. Experiments performed at 560ºC for 100 hours and 585ºC for 40 hours provided a diffusion length on the order of tens of microns. This is large enough to quantify the diffusion barrier characteristics, but small enough that the entire thickness of cerium (250 µm) would not be traversed and effect the diffusion on

the opposite sample. For each experiment, cerium was sandwiched between a coated and uncoated sample. The coating thickness was maintained at about 10 µm for these diffusion couple studies.

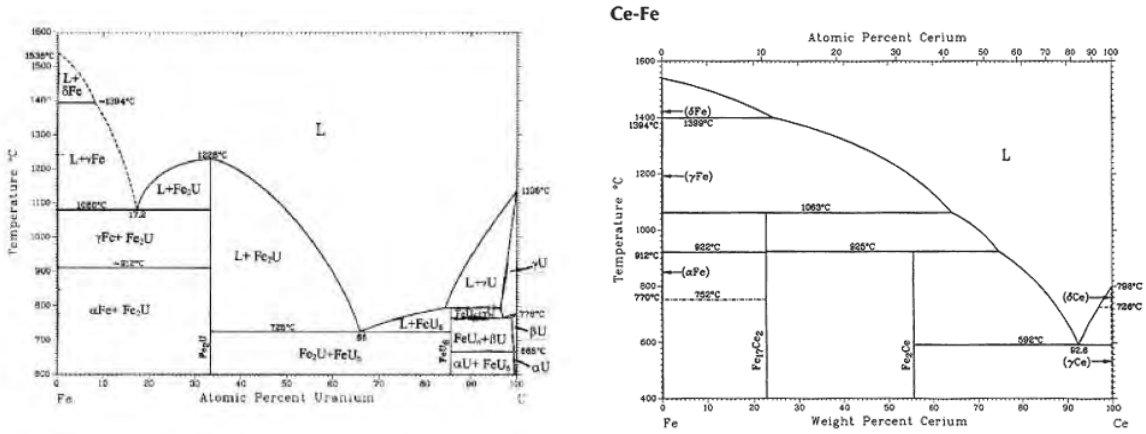

(a) (b)

Figure 11. Phase diagrams of (a) Fe-U system and (b) Fe-Ce system. The Fe-U systems has a eutectic temperature of 725ºC whereas the Fe-Ce has a lower eutectic temperature of 592ºC.

VII. Results and Discussion

VII. A. Temperature Constraints on T91 Steel

T91 steel was used as the primary substrate for deposition. Since a sintering step was investigated to further densify the coating and aid in coating adhesion it was of interest to see how the microstructure of the T91 steel could be restored after this high temperature sintering treatment.

For T91 steel, a normalizing heat treatment at 1050ºC is recommended by Sasaki et al. [48]. Since a martensitic microstructure forms following cooling from 1050ºC, a tempering heat treatment at 800ºC is necessary to avoid excessive hardening of the steel. Ideally, this recommended heat treatment step can be performed after deposition of the coatings so both heat treatment of the steel and sintering of the coatings can occur simultaneously. Heat treating at higher temperature will lead to more densification of the coating but can cause undesirable excessive grain growth in the steel. To investigate this effect, T91 samples (American Alloy and Steel) were heat treated, polished to a mirror finish then etched using Fry's Reagent (30ml H_2O, 40ml HCl, 25ml ethanol, and 5g $CuCl_2$) for 10-60 seconds. This etches the grain boundaries so that the size and shape of the grains can be investigated by SEM or optical microscopy.

The hardness of the T91 steel substrate was measured for various heat-treatment conditions (Figure 12). The sample heat treated at 1050ºC for 4 hours and tempered for 2 hours at 800ºC showed slightly lower hardness than the as-received sample (218Hv vs. 234Hv) which is within an acceptable range. Optical microscopy of the heat treated steel showed some grain growth (Figure 13 and Figure 14), which explains the loss of hardness shown in Figure 12. A

heat treatment step of up to 1350ºC is recommended in literature when sintering EPD deposits. For this reason, 1050ºC is considered a suitable balance between microstructural changes in the steel and the quality of the sintered coatings.

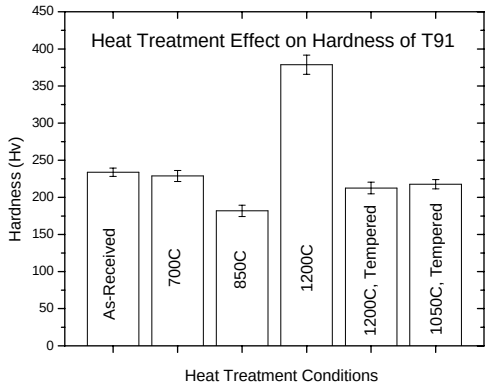

Figure 12. Effect of heat treatment on hardness of T91 ferritic steel. Heat treating and tempering at 1050ºC and 800ºC, respectively produced a hardness similar to the as-received sample.

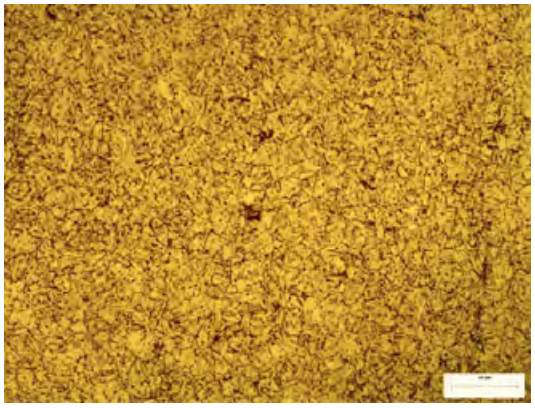

Figure 13. Microstructure of as-received T91 steel.

Figure 14. Microstructure of T91steel after heat treatment at 1050ºC for 4 hours followed by tempering at 800ºC for 2 hours.

VII. Electrophoretic Deposition

Titanium Dioxide Coatings

The most important variable in EPD process is the nanofluid composition, however the voltage and current also has a profound effect on the deposition procedure. Both these variables were optimized in this study. Experiments were performed in both constant current and constant voltage modes. The effects of additives iodine, triethanolamine (TEA), acetic acid (HAc), in acetylacetone were also investigated. The effects of particle size and phase-content of

TiO_2 on coating density and uniformity were investigated for both the green and sintered deposits.

This study concluded that the optimum mixture was acetylacetone with a small amount of triethanolamine (TEA). Constant voltage mode resulted in more reproducible coatings. Rutile phase TiO_2 suspensions exhibited less particle agglomeration than anatase phase and therefore produced denser coatings. Upon sintering, 250nm TiO_2 particles cracked and flaked off the substrate whereas 50nm particles exhibited good cohesion.

For each of these tests, it was important to keep the thickness constant since the density as well as microstructure, was utilized to quantify the quality of the coatings. For this reason, time of deposition was varied to produce coating with the same thickness (10µm for most experiments).

Both constant current and constant voltage experiments were conducted with TiO_2 nanofluids. This study was conducted with 15nm APS anatase TiO_2. It was concluded that constant voltage experiments produced more consistent deposits. For constant current experiments, 0.9 mA was applied for 120 seconds. Fluctuations in voltage were observed during depositions. As a coating gets deposited, the resistance between the electrodes increases due to buildup of the oxide coating and charged particles near the electrode. This can be seen in Figure 15 where the voltage for 0.1wt% TiO_2 varies from 17 to 26V. Figure 15(a) also shows the effect of particle concentration. Lower concentration suspensions exhibit higher voltage during these tests. This can be attributed to the particles acting as a charge carriers in this system. Higher concentrations of particles yields higher charge carrying capability, so less voltage is required to attain the needed current. Figure 15(b) shows the effect of particle concentration on coating thickness. The lower concentration suspensions deposited more mass.

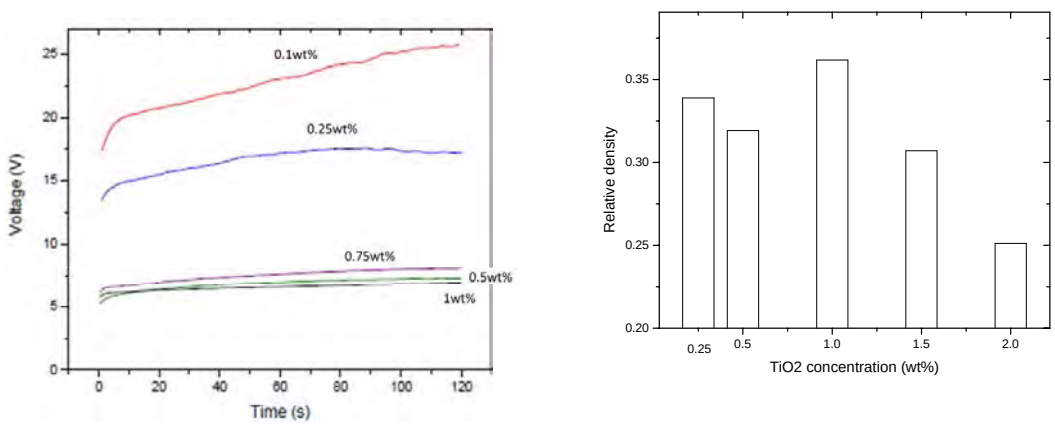

(a) **(b)**

Figure 15. (a) Constant current plots for deposition of TiO_2 suspension in ACAC with TEA. Lower particle concentration result in higher voltage and lower conductivity and (b) effect of particle concentration on thickness in constant current. mode at 0.9mA applied.

It was also shown experimentally that additions such as iodine, salts, acids, or bases significantly increase the conductivity of the mixture. The increase in conductivity corresponds with a decrease in applied voltage. Herein lies the problem with constant current mode. Recalling the Hamaker Equation, the mass deposited is proportional to the applied electric field. Furthermore, the applied voltage is proportional to the electric field, considering no changes in sample configuration. This means the mass of coating deposited is proportional to the applied voltage. This explains why more mass was deposited from lower concentration nanofluids under similar conditions, as can be observed in Figure 15(b).

Experiments performed under constant voltage mode with varying voltages confirm the correlation between applied voltage and deposition rate. Figure 16(a) shows that higher applied voltage results in higher current and Figure 16(b) shows that increasing voltage results in linearly increasing coating thickness.

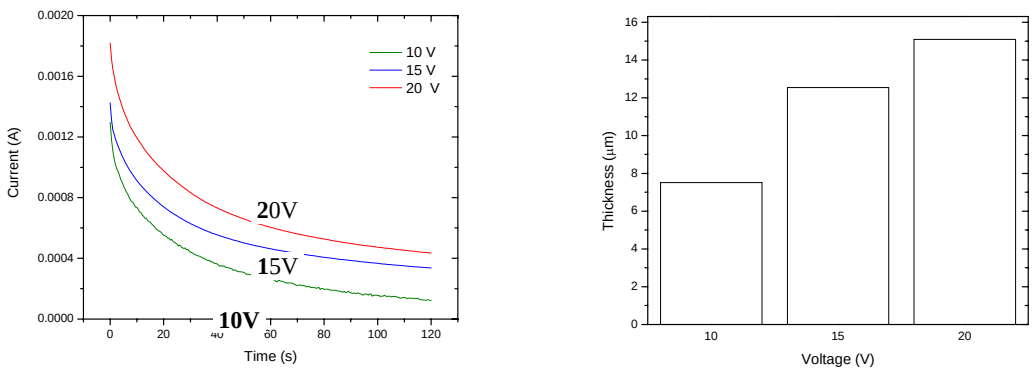

(a) **(b)**

Figure 16. Effect of applied voltage on (a) current and (b) thickness of coatings. Higher voltage results in higher current and thicker coatings. Experiments were performed with a nanofluid consisting of 0.5wt% TiO_2 in ACAC.

Figure 17(a-c) show the effect of particle concentration on (a) current, (b) thickness (c) as-deposited density of the coatings made with TiO_2 in ACAC with iodine. For this study, a constant voltage of 20V was applied for 2 minutes.

Figure 17(b-c) shows that particle concentration does not have a significant effect of the thickness or density of the coatings when concentration is below 1.5 wt%. The coating formed with higher, 2 wt%, concentration produced a thicker, lower density coating. This finding agrees with a theory hypothesized by Dor et al. [28] that density decreases as coating thickness increases, specifically for coatings thicker than 10µm.

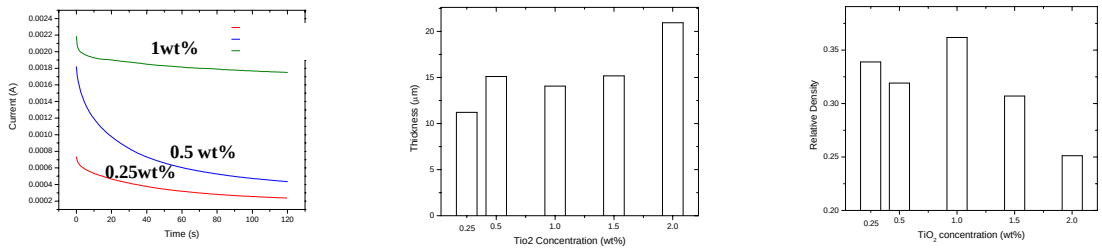

(a) **(b)** **(c)**

Figure 17. The effect of nanoparticle concentration on (a) current, (b) thickness of coatings, and (c) relative density. The nanoparticle concentration was found to have little effect on coating thickness or density below 1 wt%. Experiments were performed with a nanofluid consisting of 0.5wt% TiO_2 in ACAC.

Once it was established that constant voltage experiments were more reproducible than constant current experiments, all further experiments (with TiO_2 and all other coating materials) were conducted using the constant voltage method. Also, since the particle concentration does not significantly affect the deposition rate or coating density, all further experiments were performed with 0.5 wt% nanofluids.

The effect of several charging additives on TiO_2 depositions was investigated. Specifically, the effects of additives triethanolamine (TEA), acetic acid (HAc), and iodine on coating density and microstructure were investigated. The standard 0.5 wt% particle concentration was used in an acetylacetone solvent (0.2 g TiO_2/40ml ACAC). It was concluded that the additive TEA produces the densest coatings for the various additives studied.

Recalling the literature review, each of these additives produces positively charged ions, which are then adsorbed onto the particle's surface. TEA produces $HN^+(\text{-R-OH})_3$, whereas the other reactions produce protons (H^+). The positively charged ions are adsorbed on the nanoparticle's surface, giving them positive charge. They are then driven towards the cathode and form a deposit.

The amount of each additive to be used was taken from literature. TEA was added in 0.15 vol% relative to the solvent (~60 µL/40 ml). However, adding more TEA did not have a significant effect on deposit density or microstructure. Iodine was also in an amount equal to 8 wt% of the powder concentration, equaling 0.016 g iodine for 0.2 g TiO_2. In addition, acetic acid was added in 1.25 vol% (0.5ml/40ml).

The zeta potential of selected nanofluids was measured using electroacoustic principles and the results are shown in Figure 18. The measurements were conducted by Matec Applied Science, Inc, MA (www.matec.com). Recall that zeta potential is a measure of the charge on each particle. This can be correlated to nanofluid stability and amount of mass deposited through EPD. As may be seen in Figure 18, the additive triethanolamine (TEA) produces nanofluids with the highest zeta potential of ~37mV. Nanofluids comprised of only TiO_2 and ACAC exhibited the second highest zeta potential (~30mV). Additions of iodine and iodine and TEA together reduced the zeta potential. This data shows that the particles in a nanofluid

containing TEA have higher charge than the others. This higher charge may reduce the size agglomerates, and produce denser coatings.

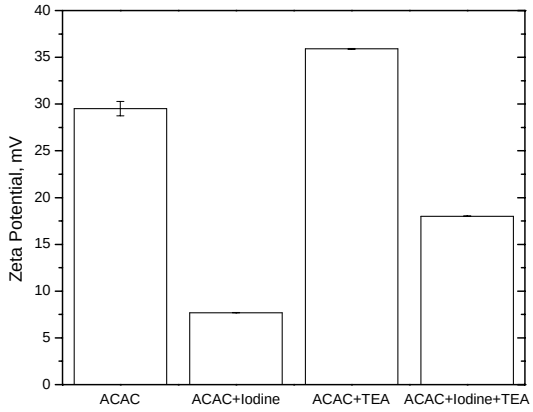

Figure 18. Zeta potential measurements of 0.5wt% TiO_2 in ACAC with selected additives. Acetylacetone with the additive TEA produces the highest zeta potential.

The coating density was measured by dividing the mass change by the volume of the deposited coating. The density is measured relative to the theoretical density of anatase phase TiO_2 (3.9g/cm^3). Experiments conducted with nanofluids containing TEA produced significantly denser coatings. These coatings were nearly 50% of theoretical density, whereas the others were 42% or less. Results of these measurements are shown in Figure 19.

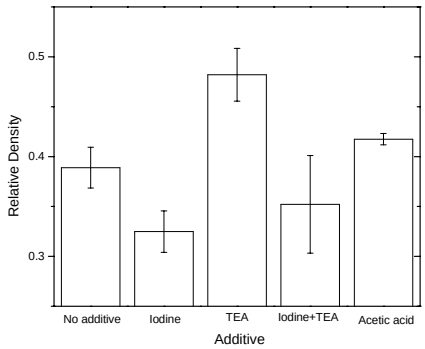

Figure 19. Effect additive on coating density for TiO_2 depositions. TEA resulted in the densest coatings. All experiments performed with 0.5wt% TiO_2 in ACAC.

The microstructure of these coatings was also investigated using scanning electron microscopy. Images of the microstructure of coatings qualitatively show that TEA has the least porosity (Figure 20), thus confirming the density calculations. Microstructural investigationS also showed that lower density coatings have larger agglomerates.

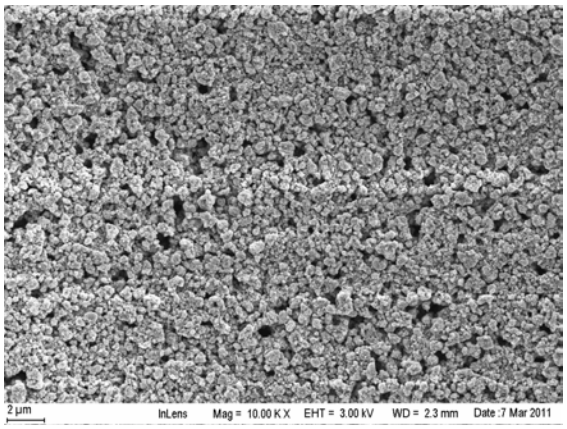

(a) No Additive

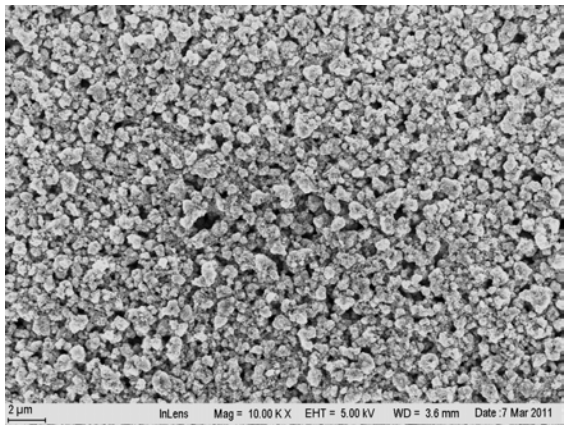

(b) 8wt% Iodine

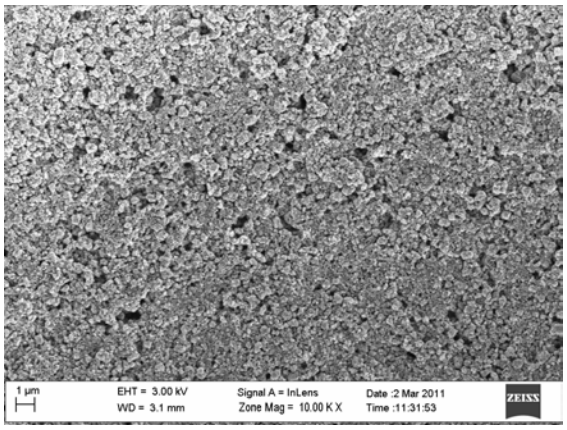

(c) Acidic Acid

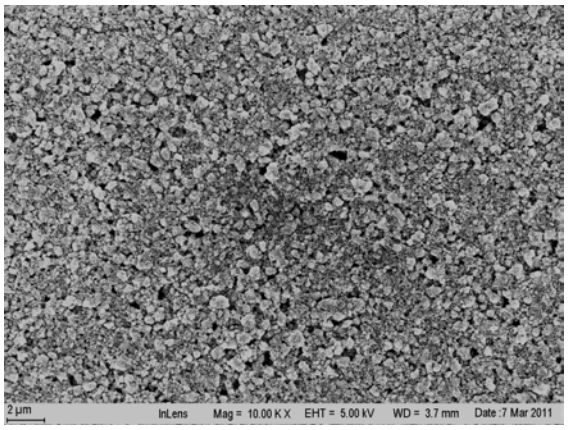

(d) TEA

Figure 20. Surface microstructure of TiO_2 coatings produced by various additives. Coatings formed with the additive TEA qualitatively show the lowest porosity and smallest particle size. This agrees with the density data shown in Figure 19.

We theorize that TEA additions produce more highly charged particles than the other additives. This is due to the charge carrying ion, $HN^+(\text{-R-OH})_3$ and protons rather than only protons as is the case with the other additives. Since the TiO_2 particles are more highly charged, less agglomeration occurs and denser coatings result.

There are two common phases of TiO_2: anatase and rutile. Most reported EPD studies of TiO_2 have used anatase powders, although rutile is the more stable phase and has higher density. To compare coatings using these two phase powders, TEA was used as an additive and constant voltage was applied. It was determined that the 250 nm rutile-phase particles produce the densest coatings, but often tended to flake off the steel substrate upon sintering. It was found that anatase particles undergo a phase transformation and convert to rutile upon sintering at 1050ºC. The anatase coatings also tend to crack upon sintering which can be attributed to a large decrease in volume due to phase transformation and sintering effects. As a sintering step is needed to increase adhesion, the optimum coating was found to be 50nm rutile phase TiO_2.

There are several sizes available of both rutile and anatase TiO_2. This study is focused on the 15 nm and 50 nm anatase particles, and the 50 nm and 250 nm rutile. The density of each phase must be taken into account when determining the theoretical density as the density of anatase is 3.9g/cm^3 and that of rutile it is 4.2g/cm^3.

The rutile coatings showed higher as-deposited density (Figure21). This can be attributed to significantly less agglomeration of rutile particles compared to anatase. SEM images showed that anatase forms large agglomerates that are nearly 1µm in diameter. Rutile did not exhibit this agglomeration and by all evidence it was concluded that the particles remain separate and deposit as individual particles. SEM images of each of the as-deposited coatings are depicted in Figure 22.

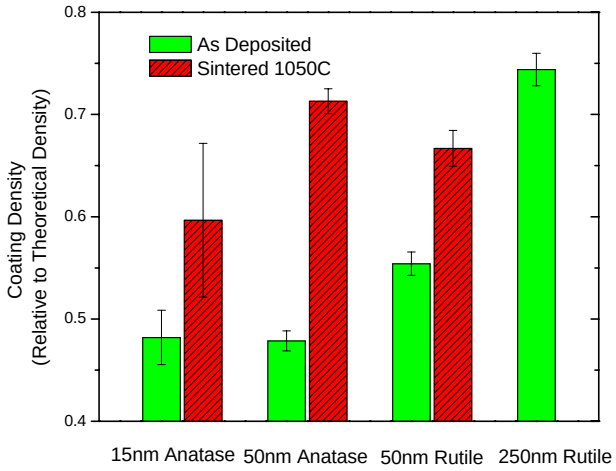

Figure 21. Density of coatings for rutile vs. anatase phase and particle size. Coatings comprised of rutile phase particles exhibit higher green density.

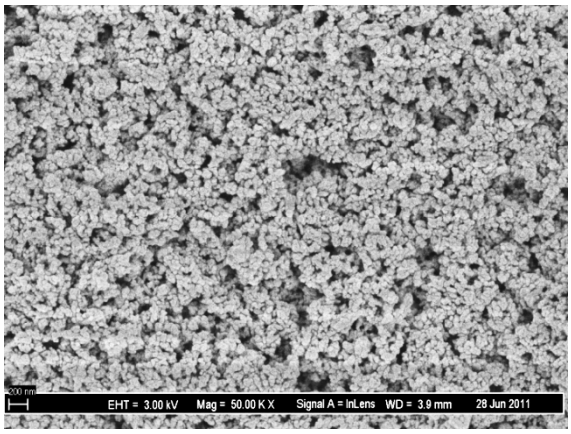

(a) 50nm Rutile

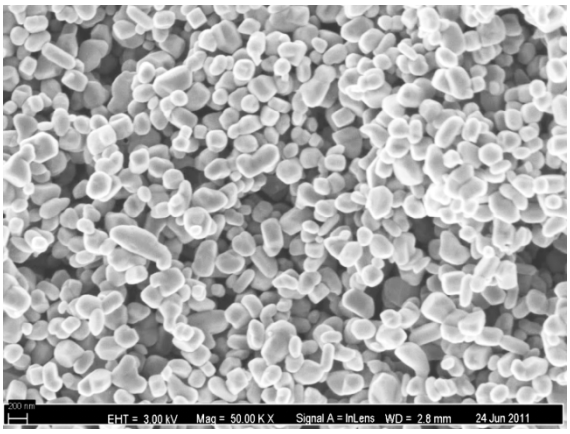

(b) 250nm Rutile

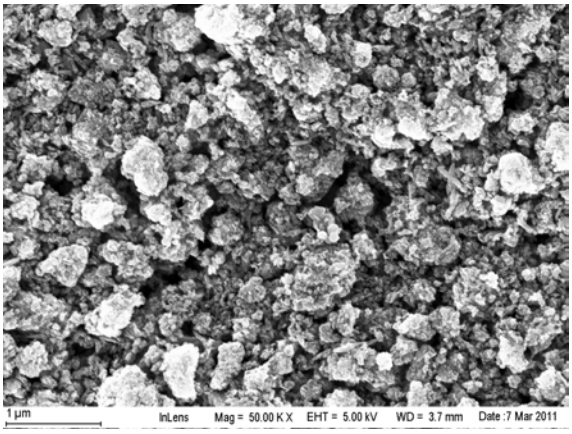

(c) 15nm Anatase

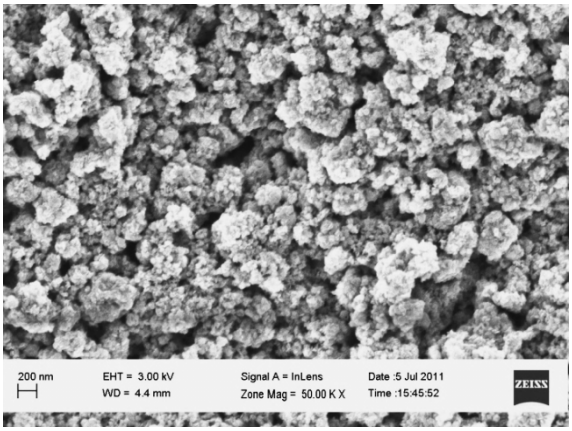

(d) 50nm Anatase

Figure 22. Surface microstructural images of TiO_2 coatings high magnifications. Rutile coatings (a-b) do not show agglomeration, whereas the anatase particles form clusters (c-d). The clusters are the cause of lower density green coatings and crack formation upon sintering.

In addition to exhibiting higher density, rutile is a better coating candidate than anatase because it does not undergo a phase transformation during sintering, and more importantly it does not form agglomerates. Small anatase particles form aggregates while suspended in acetylacetone and deposit as such. These agglomerates sinter together and pull the coating apart, causing the formation of cracks as seen in Figure 23. X-ray diffraction spectroscopy was utilized to confirm the phase transformation in the coatings comprised of anatase particles (Figure 24).

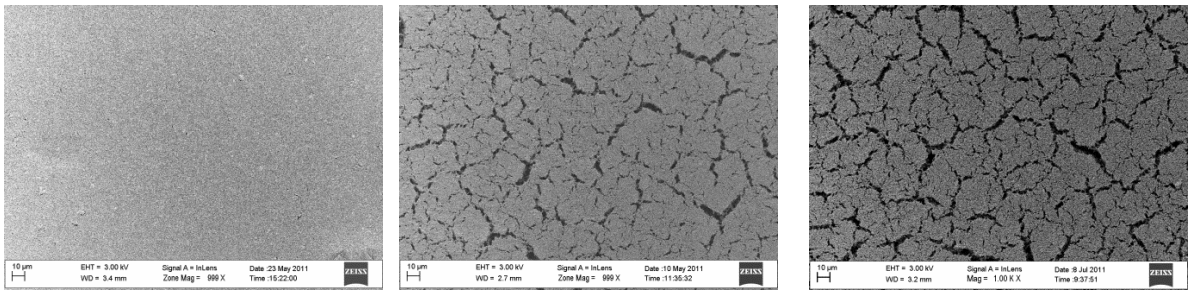

(a) 50nm Rutile **(b) 15nm Anatase** **(c) 50nm Anatase**

Figure 23. SEM micrographs of TiO_2 coatings at 1000X. The anatase coatings (b-c) show severe cracking, whereas this is not seen in the 50nm rutile based coating. All coatings were formed from nanofluids containing ACAC and TEA.

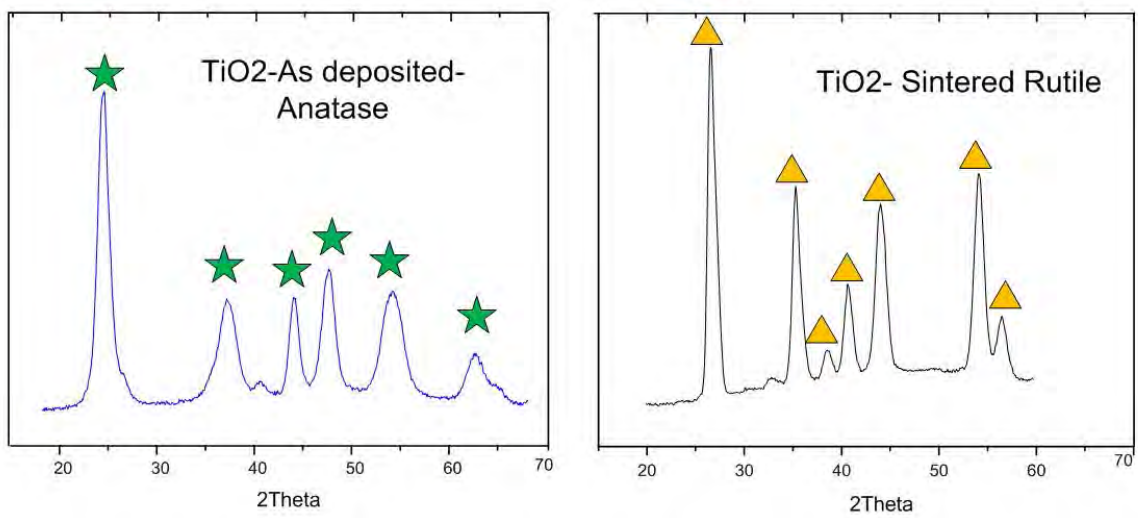

(a) **(b)**

Figure 24. X-ray diffraction spectra of (a) the as-deposited coating comprised of anatase particles and (b) the same coating, now comprised of rutile TiO_2, after sintering at 1050ºC for 4 hours. The conversion of anatase to rutile phase TiO_2 is accompanied by a volume decrease which may contribute to the cracking.

The optimum coatings were produced using 50 nm rutile nanoparticles. Figure 25 shows several appealing aspects of these coatings. Figure 25(a) shows how the particles deposit individually and (b) shows how the particles adhere well to each other upon sintering. Figure 25(c-d) shows that cracking is not evident in the as-deposited or sintered coatings.

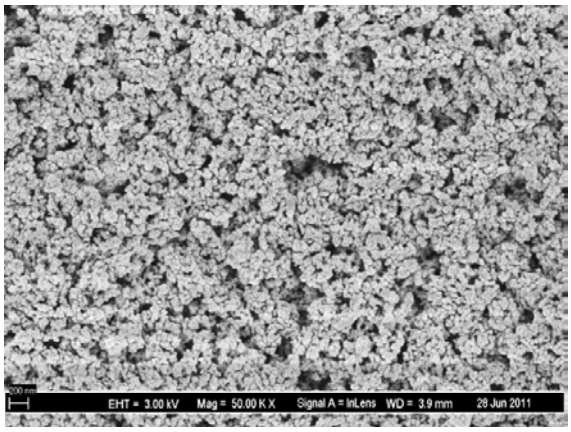

(a) 50nm rutile prior to sintering,

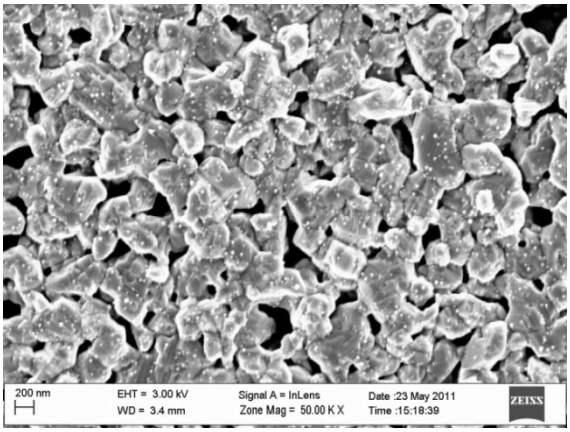

(b) 50nm rutile sintered at 1050ºC for 4 hours.

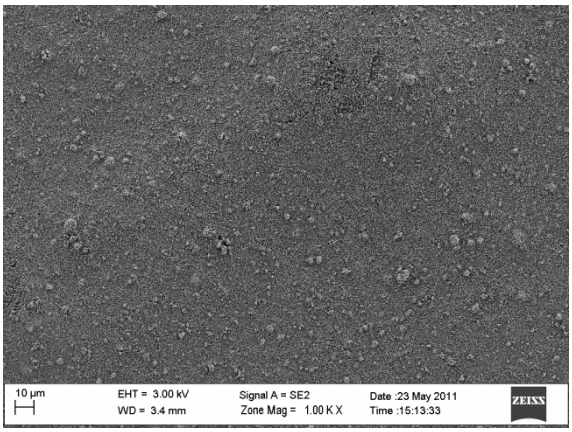

(c) 50nm rutile prior to sintering

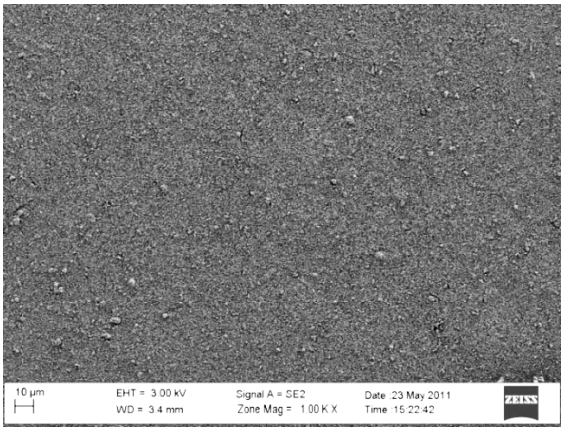

(d) 50nm rutile sintered at 1050ºC for 4 hours.

Figure 25. SEM images of TiO_2 coatings before and after sintering at 1050ºC (high magnification images) (a-b) illustrate the sintering effects at high magnification (c-d) lower magnification showing that cracking is not evident even after sintering. All coatings were produced using nanofluids containing acetylacetone and TEA.

Of critical importance is also the steel-coating interface. Focused ion beam (FIB) was used to investigate the interface between the steel and as-deposited and sintered TiO_2 coatings (Figure 26a-b). Both coatings were prepared using the optimum coating conditions. These micrographs show the benefits of the sintering step. A gap can be observed between the as-deposited coating and the steel surface, whereas this is not noticeable in the sintered sample. Also, the surface of the sintered coating is much more intact than the as-deposited surface.

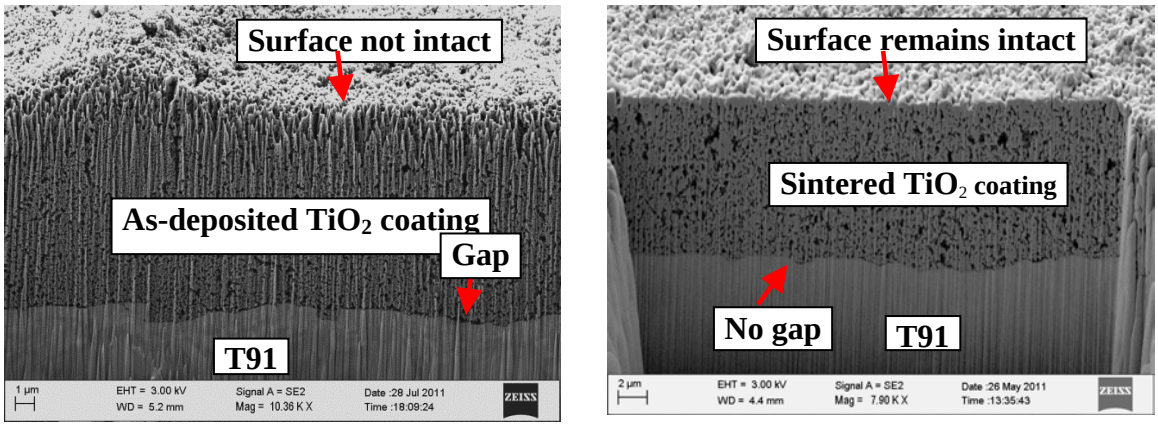

(a) (b)

Figure 26. Focused Ion Beam (FIB) micrograph of (a) as-deposited TiO_2 coating and (b) TiO_2 coating sintered at 1050ºC for 4 hours. Coatings were formed from nanofluids containing acetylacetone with the additive TEA.

In next set of experiments rutile nanoparticles were used. Coatings were deposited using 50nm, 250nm and a mixture of 50+250nm (1:1) nanoparticles. Figure 27 shows the density of the coatings before and after sintering at 900ºC and 1050ºC for 6 hours. Some coatings undergo excessive densification upon sintering at 1050ºC and flaked off from the steel substrate. Figure 28 and 29 show the SEM Inlesn plan view micrographs of the coatings before and after sintering, respectively.

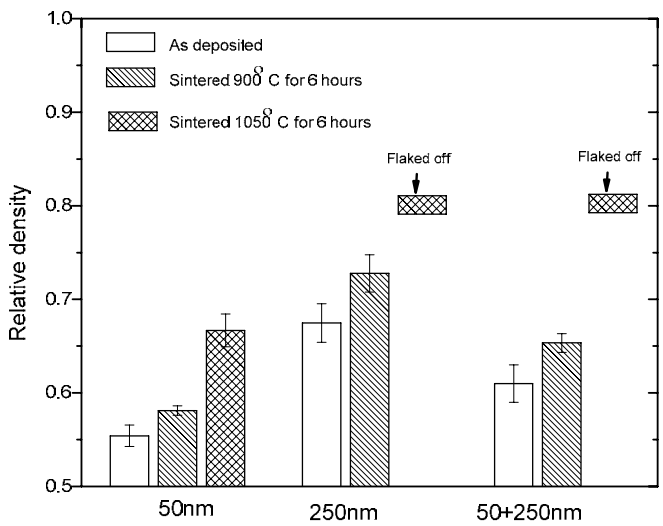

Figure 27.Effect of rutile particle size on the coating density before and after sintering at 900ºC for 6 hours and 1050ºC for 6 hours.

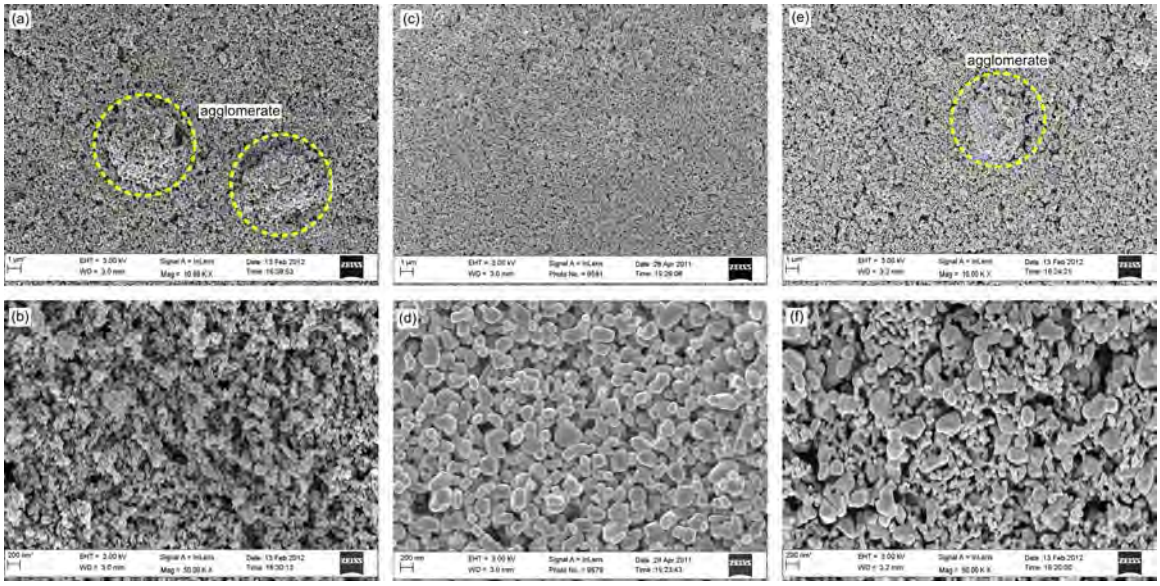

Figure 28. SEM Inlens plan view micrograph of the as deposited coatings produced with rutile nanoparticles (a & b) 50nm (c & d) 250nm (e & f) 50+250nm.

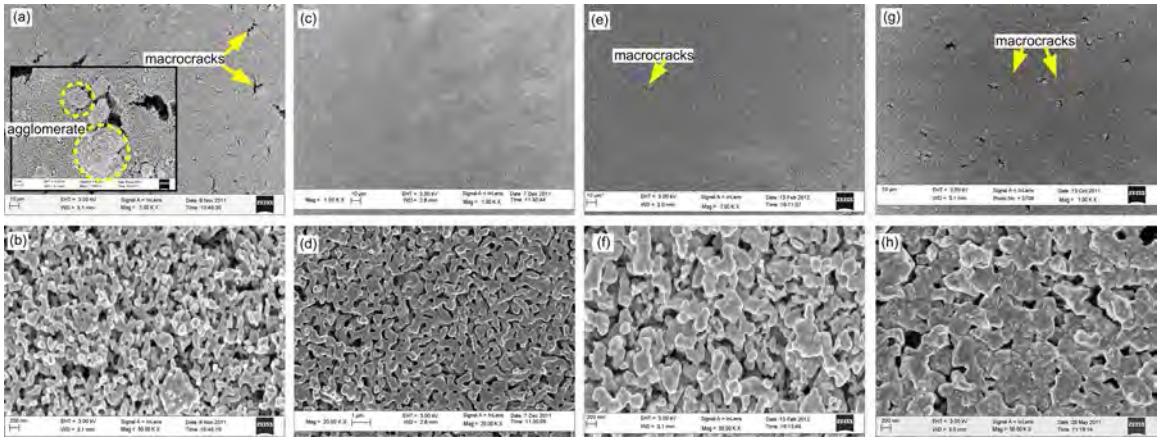

Figure 29. SEM Inlens plane view micrograph of the sintered coating at 900ºC for 6 hours produced with rutile nanoparticles (a & b) 50nm (c & d) 250nm (e & f) 50+250nm and (g & h) with 50nm and sintered at 1050ºC for 6 hours.

All coatings were completely crack free in the as deposited condition. Unlike coatings prepared with anatase nanoparticles; coatings made with rutile nanoparticle are formed with deposition of mostly individual nanoparticles and not as deposition of agglomerates. However, in the coatings made with 50nm rutile nanoparticles, big agglomerates with the size of almost 1µm are still seen. In the coatings made with 250nm rutile nanoparticles there is almost no evidence of particle agglomeration. This promotes very high packing of the nanoparticles resulting in high green density of the coatings (66%). In the coatings made with the mixture of 50 and 250nm nanoparticles some regions with agglomeration of 50nm nanoparticles are still seen. However, it seems that both types of particles incorporate equally in the coating.

Once the rutile coatings are sintered it is noticeable that significantly less cracking happened compared to anatase coatings. Lack of severe agglomeration and phase transformation are the

two major reasons for better sintering performance. However, in the coatings made with 50nm rutile nanoparticles still some cracking happened around the agglomeration regions. During sintering, in the agglomerated regions, the cluster shrinks independently from the body of the coating which induces tensile stresses between agglomerate and coating body. Since the particles form a weak bond during sintering, cracking initiates from the interface of agglomeration/coating and propagates throughout the coating. Furthermore, in the coatings made with smaller nanoparticles of 50nm more densification and shrinkage is required to achieve the high densities due to their low green density compared to coatings made with 250nm. On the other hand by sintering at higher temperature of 1050ºC excessive densification and spallation happened in the 250nm and 250+50nm coatings while in the 50nm coating densification up to 68% happened. According to density measurement results and microstructural investigations, it is concluded 250nm nanoparticles are the best choice for EPD coatings due to the agglomeration free and high packing deposition and good densification at lower sintering temperatures. In the next section, the sintering cycle for the coating is optimize to achieve the highest density and coating/substrate bonding.

Optimizing the Sintering Cycle

In this section, optimization efforts of the sintering cycle of the EPD coatings have been will be discussed. Several cycles has been tested. In some experiments, the coating flaked off from the substrate due to excessive densification. Table 3 summarizes the sintering cycles investigated and the visual inspection results on the samples. One can notice that by sintering at temperatures higher than 1000ºC for more than 1 hour, the coatings sinters extensively and flake off from the T91 substrate due to lack of adequate bonding. Figure 30 summarizes the density measurement results of the samples. Figure 31 shows the plane view SEM Inlens images of coatings sintered at different cycles.

All coating were free of cracking. As it can be seen in both density measurements and SEM results by increasing the sintering temperature the densification increases. For better densification of the coatings extended sintering was performed at 850°C for 24 hours after sintering at 1000°C for 1 hour and 900°C for 6 hours. The extended sintering helps to enhance the level of densification even up to about 90% of the theoretical density in the sample sintered at 1000°C for 1 hour. Sintering of the coating is constrained by the substrate, hence the degree of densification is lower in constrained sintering compared to free standing sintering. The substrate limits the densification by its greater thermal expansion that applies tensile tension on the coating during sintering and its rigidity in the isothermal sintering step that leaves only one direction for free sintering [31]. In the study of Lu et al [32] it is suggested that in the extended sintering after sintering at higher temperature (here 850°C for 24 hours after 900°C or 1000°C) a compressive mismatch stress induces between coating and substrate. This stress can be large as sintering stress induced by surface energy and therefore a semi pressure assisted sintering occurs. It was also determined that in the coatings sintered at 850°C for 24 hours after sintering at 900°C, significantly less grain growth was seen compared to the one sintered at 1000°C for 1 hour. According to Mazaheri et al [33, 34] by two step sintering at lower temperatures, triple junctions mobility plays the role of controlling mechanism due to having higher enthalpy of

activation. Grain boundary mobility is inhibited by lack of motion in triple junctions and the process leads to densification with smaller grain size.

Figure 32 shows the FIB cross section of the samples in the coatings before and after sintering. No bonding between the coating and substrate is seen in the as deposited coating (Figure 13a). Some bonding starts to form by sintering at constant temperature at 900°C (Figure 13b). However, a significant dense bonding layer forms right at the interface of T91/ TiO_2 by extended sintering at 850°C for 24 hours. EDS analysis shows that significantly the diffusion region is significantly bigger in the coating sintered for an extended period (Figure 32 d and e). The bonding region is reach in chromium. It is well known that diffusion in the BCC crystal structure of ferrite occurs much more rapidly than in the FCC crystal structure of austenite. The Ferrite to austenite phase transformation happens at roughly 900°C for T91 steel. The higher diffusion rate therefore created a better bonding between the coating and steel substrate.

Table 3. Examined sintering cycles and the visual inspection results.

#	Sintering cycle	Visual inspection
1	850°C -2hr	OK
2	850°C -6hr	OK
3	900°C -6hr	OK
4	950°C -6hr	OK
5	1000°C -6hr	Flaked off
6	1050°C -2hr	Flaked off
7	1000°C -1hr	OK
8	950°C -6hr-850°C -24hr	Flaked off
9	900°C -6hr-850°C -24hr	OK
10	1000°C -1hr-850°C -24hr	OK

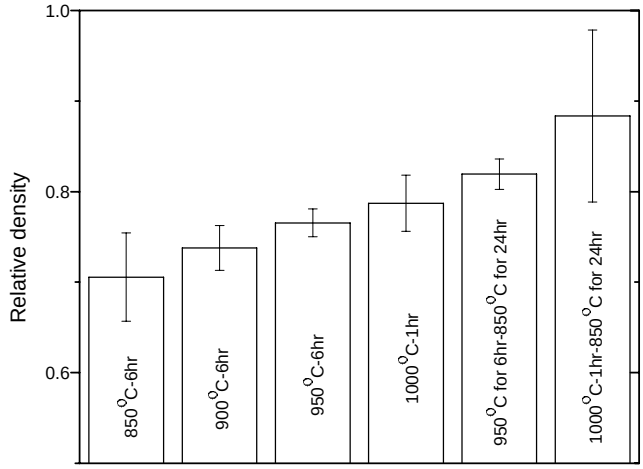

Figure 30. Effect of sintering temperature and time on the density of the coatings prepared with 250nm rutile nanoparticles.

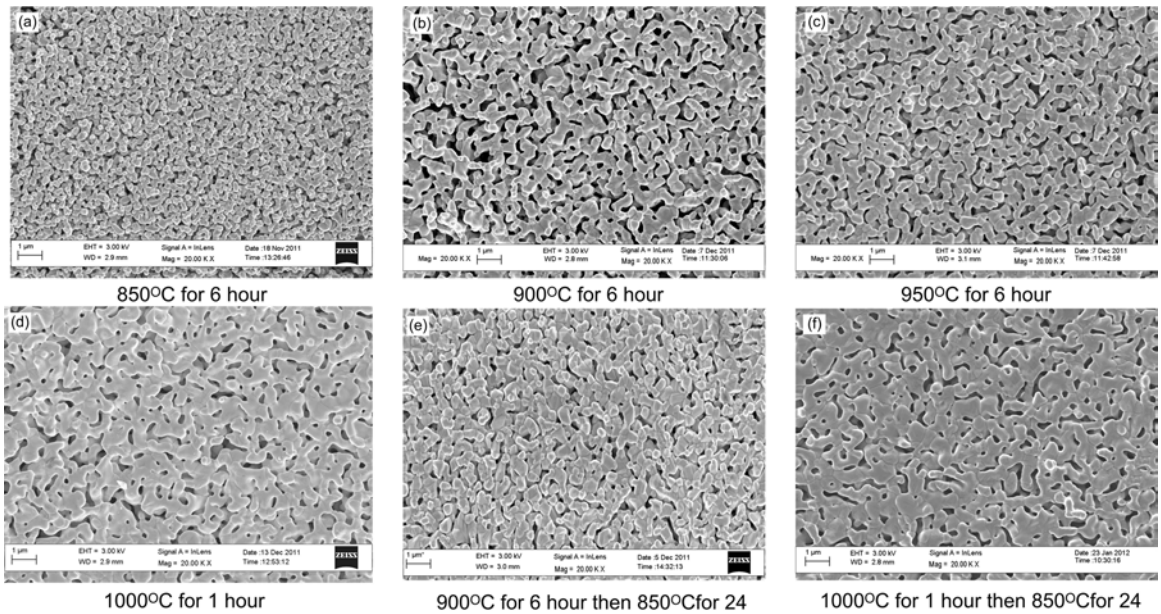

Figure 31. SEM Inlens plan view images of the coating made with 250nm Rutile nanoparticles at different sintering cycles.

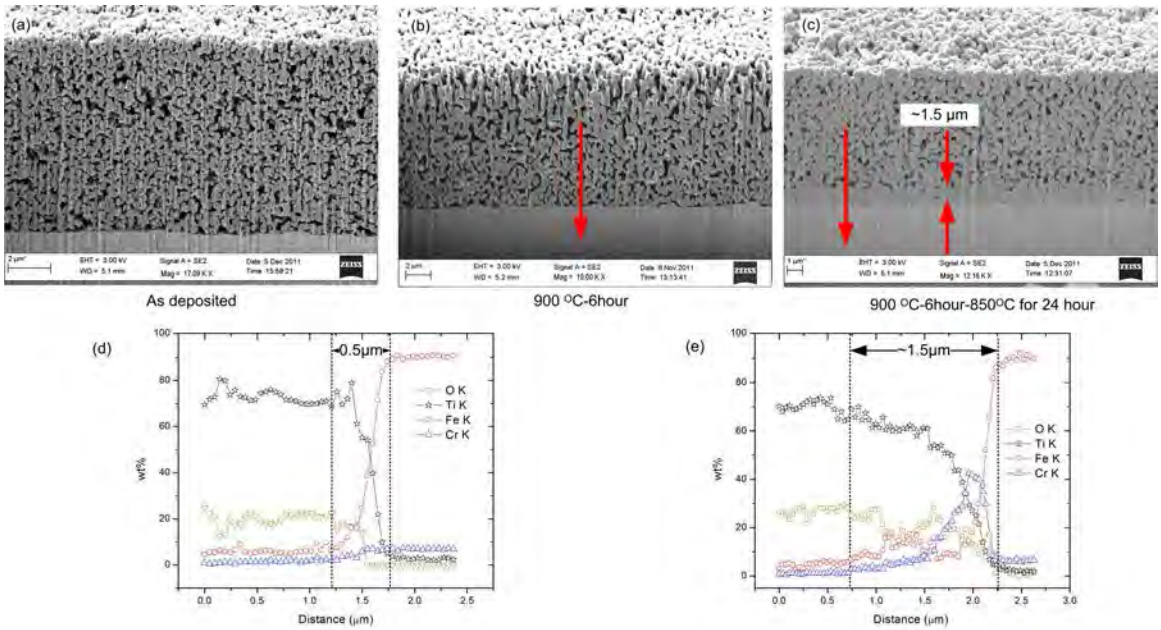

Figure 32. FIB cross section and EDS analysis across the coating-substrate interface of the coatings made with 250nm nanoparticles (a) as deposited (b) sintered at 900°C for 6 hour, (c) sintered at 900°C for 6 hours+ at 850°C for 24 hours. (d) and (e) EDS analysis along the interface at (b) and (c), respectively.

Yttria-Stabilized Zirconia Coatings

Systematic studies were performed to determine the optimal suspension parameters and particle size for YSZ coatings. The YSZ particles used to produce these coatings contained 8 mol% yttria, with the remainder being ZrO_2. Suspension additives of iodine, TEA, and acetic

acid were used in combination with isopropanol, acetone, ethanol, and acetylacetone solvents. Particle size studies compared coatings comprised of 20-30 nm and 200-300 nm nanoparticle size ranges. The optimum coatings were then sintered at 1050ºC and densities were again measured after sintering. A suspension containing 0.15 vol% TEA in acetylacetone was determined to produce the most reproducible, uniform, dense coatings. Particle size had little effect on the as-deposited coatings, but the smaller particles (20-30nm) resulted in more cracking upon sintering, but cracks did not occur with the larger (200-300nm) particles.

The first step in this study was to optimize the nanofluid. As with TiO_2, the powder concentration was kept relatively low at 0.5 wt% particle concentration (0.2g/40ml solvent) and particle sizes of 20-30 nm. In order to make accurate density measurements, the coating thicknesses were kept constant at 15µm. Table 4 shows the nanofluids investigated in this study. Selected nanofluid mixtures were inspired by literature and others (ACAC/I_2 and ACAC/I_2, TEA) were derived from mixtures used in our study for TiO_2 coatings.

Table 4. Solutions investigated for deposition of YSZ coatings by the EPD process.

Label	Author	Solvent	Additive
ACAC	X.J. Lu	Acetylacetone	-
ACAC/TEA	Hui, Xu	Acetylacetone	0.625% TEA
ACAC:Eth	Xu/Talibi	Acetylacetone and Ethanol (1:1)	-
ISO	Jia	Isopropanol	Iodine
AC:Eth/I2	Aruna	Acetone and Ethanol (3:1)	Iodine
ACAC/I2	-	Acetylacetone	Iodine
ACAC/I2,TEA	-	Acetylacetone	Iodine and TEA

Coating density and microstructural characteristics were primarily used as metrics to optimize YSZ coatings. The mass change was recorded and thickness measured using a magnetic thickness gauge. Figure 33 shows the density of the green coatings. Coatings could not be consistently produced from several of the suspensions, which is the reason not all of the mixtures from Table in this figure.

As shown in Figure 33, ACAC with TEA, ACAC with TEA and iodine, and 1ACAC:1Ethanol produced dense coatings. In order to further isolate the optimum suspension, the microstructure of these dense coatings was examined (Figure 34).

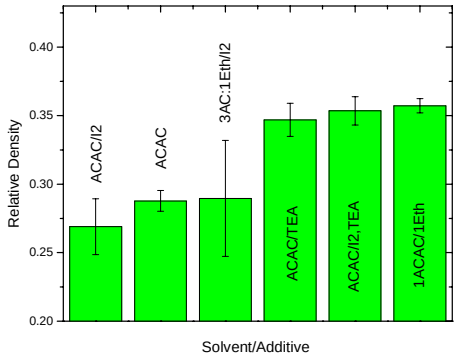

Figure 33. Three suspensions formed significantly denser YSZ coatings than the others. The microstructure of these coatings was examined to determine the optimum nanofluid, which was found to be acetylacetone with 0.15 vol% TEA.

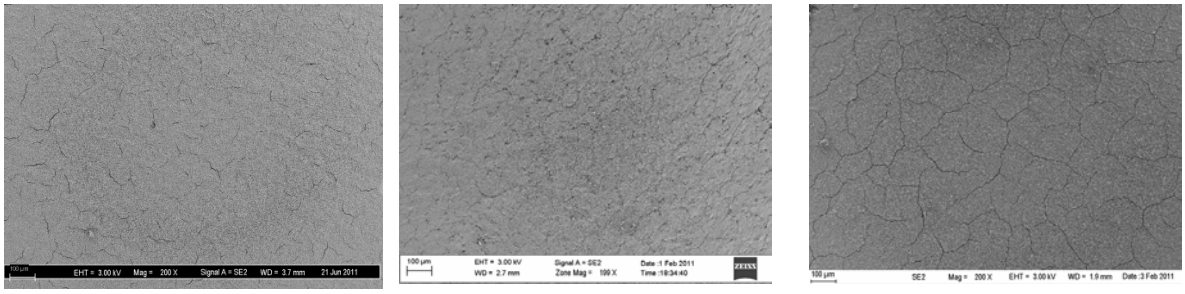

(a) ACAC/TEA **(b) ACAC/TEA,I2** **(c) ACAC:Ethanol**

Figure 34. SEM micrographs comparing the surface microstructure of dense YSZ coatings. The coating formed from ACAC:Ethanol (c) exhibited significantly more cracks than the others.

Based on these microstructural examinations, further studies were discontinued for ACAC/Ethanol suspension. In the interest of simplicity, the ACAC/TEA suspension was selected for this study as the chemical reactions of a system comprised of TEA and I_2 are not well understood and may have produced more inconsistent coatings.

The next step was to choose which particle size produces the densest coatings without sacrificing microstructural uniformity: 20-30 nm or 200-300 nm. For these studies, 0.5wt% YSZ was suspended in acetylacetone with 60µL of TEA (0.15 vol%) and coating thickness remained constant at 10µm. These samples were then sintered at 1050ºC for 4 hours to densify the coating and aid in adhesion. Density data for the as-deposited and sintered YSZ coatings is depicted in Figure 35.

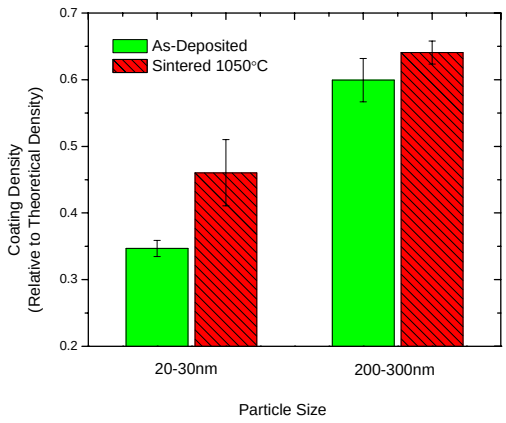

Figure 35. Effect of particle size and sintering on YSZ coating density. The larger particles produce denser coatings, both before and after sintering because larger particles do not form agglomerates in the nanofluid. All depositions were performed using nanofluids of acetylacetone and 0.15 vol% TEA.

Significantly higher density was observed for the coatings formed with the 200-300nm particles compared to those with the smaller 20-30 nm particles. This can be attributed to agglomeration of the smaller particles. As seen in Figure 36, the larger particles deposit as individual particles whereas the smaller particles (20-30nm) deposit as clusters.

In addition to higher density, the larger particles exhibited less cracking both before and after sintering. Sintering caused the coatings comprised of the smaller particles to exhibit cracking, but this was not seen with the larger particles (200-300nm). SEM micrographs of the as-deposited and sintered 20-30 nm and 200-300 nm coatings are presented in Figure 37 b and c, smaller particles tend to form coatings that crack easily because the clusters sinter into one large particle, and these larger particles in turn do not sinter and causing cracking (Figure 37 c and e). The larger particles showed little signs of cracking even after sintering (Figure 37f).

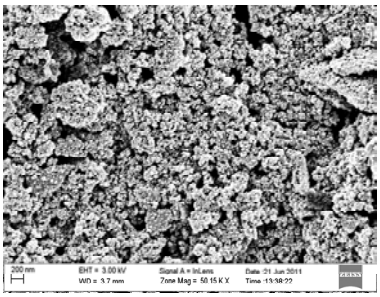

(a)

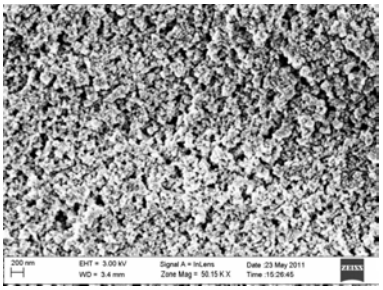

(b)

Figure 36. SEM micrographs of as-deposited YSZ coatings high magnifications. Coating comprised of (a) 20-30 nm particles and (b) 200-300 nm particles. It is clear that the larger particles do not agglomerate as much as the smaller ones. All coatings were formed with nanofluids containing ACAC and TEA.

As with titanium dioxide, the steel-coating interface is significantly important. The interface of the 200-300 nm sintered YSZ coating and the steel was investigated by focused ion beam (FIB) analysis (Figure 38). As seen in the TiO_2 coating, there is no gap between the steel and the coating, indicative of a well-adhered coating.

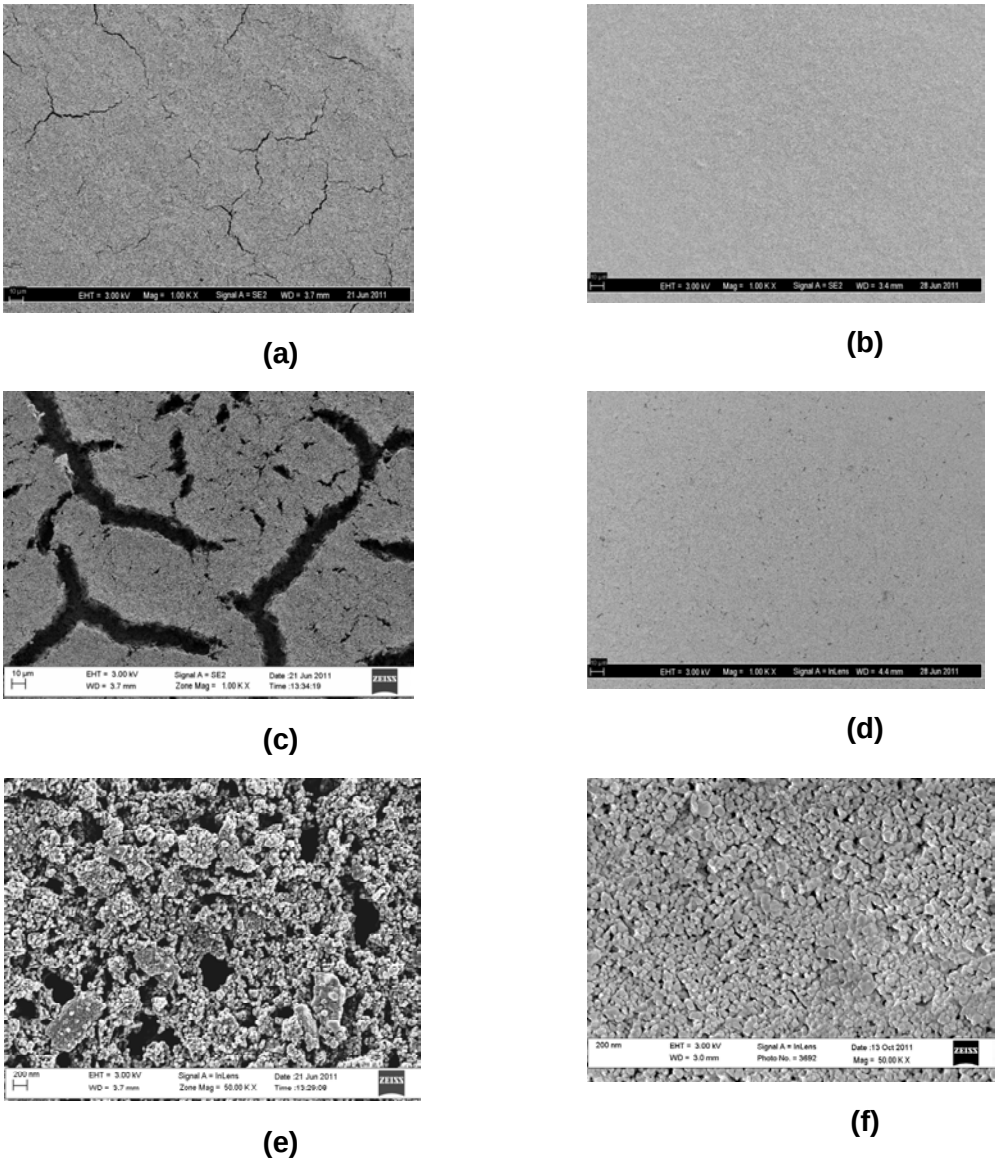

Figure 37. YSZ coatings at 1000X. All coatings were formed from a 0.5wt% nanofluid with 0.15vol% TEA. (a) As-deposited 20-30nm YSZ. (b) As-deposited 200-300nm YSZ (c and e) 20-30nm YSZ coating sintered at 1050ºC for 4 hours (d and f) 200-300nm YSZ coating sintered at 1050ºC for 4 hours. Coatings comprised of the larger particles do not form cracks before or during sintering, whereas the smaller particles cause cracking in the green coatings which becomes severe during sintering. Coatings were formed from nanofluids containing acetylacetone with a TEA additive.

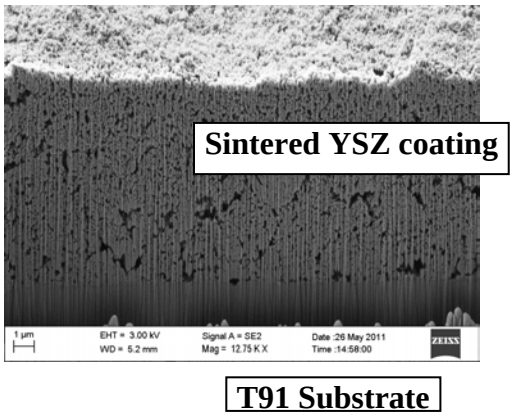

Figure 38. FIB micrograph of a sintered YSZ coating. Lack of large gaps between the substrate and coating indicate good adhesive properties. Coating was formed through EPD using an acetylacetone/TEA nanofluid.

To further evaluate the profound effect of particle size on the density of the coatings before and after sintering coatings were also prepared using 100-200nm nanoparticles with similar deposition parameters for 20-30nm nanoparticles. Additionally, experiments were performed using two sintering steps, at 850ºC and 1050ºC with the goal of reducing the residence time at 1050ºC. Figure 39 compares the as deposited and sintered at 1050ºC for 4 hours with and without extended sintering at 850ºC for 24 hours. Figure 40 shows the plan view SEM images of the as deposited coatings. More agglomeration is again observed in the smaller particles, even though both coatings with thicknesses of roughly 9µm and free from macro cracks. In the coating made with 20-30nm nanoparticles, some micro-cracks can be seen among the agglomerates. More particle agglomeration in the smaller particles reduced the proper particle assembly and high packing density and results in less density compared to the coatings made with larger particles. Again, the higher agglomeration level of smaller particles is due to their higher surface area.

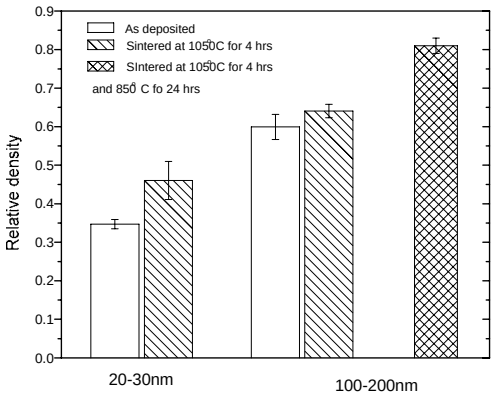

Figure 39. Effect of particle size and sintering on YSZ coating density. The larger particles produce denser coatings, both before and after sintering at 1050ºC because level of agglomeration is less in larger particles in the nanofluid. Extended sintering at 850ºC resulted in higher density. All coatings were made by ACAC+Ti+0.15vol% TEA nanofluid.

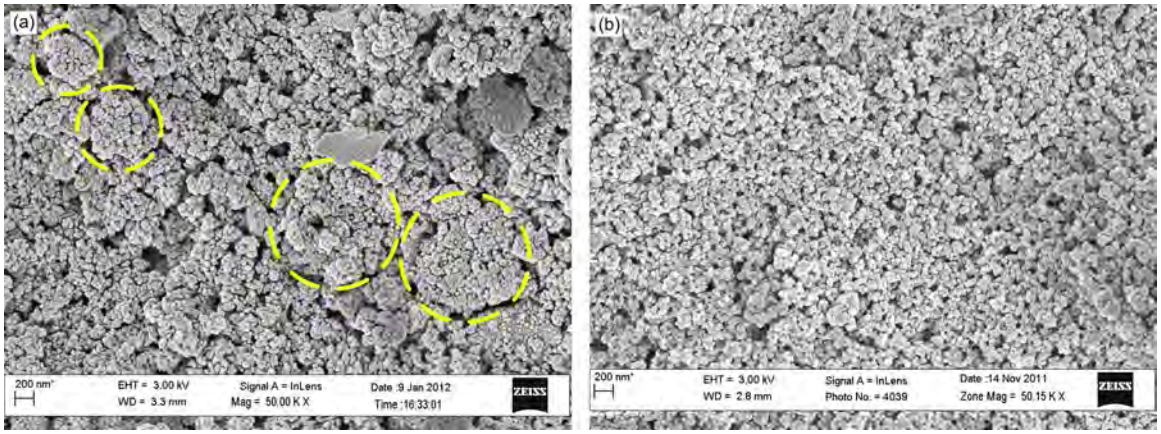

Figure 40. SEM surface microstructure of as-deposited YSZ coatings made with (a) 20-30nm and (b) 100-200 nm nanoparticles. It is clear that the larger particles do not agglomerate as much as the smaller ones. All coatings were formed with nanofluids containing ACAC+0.15vol% TEA.

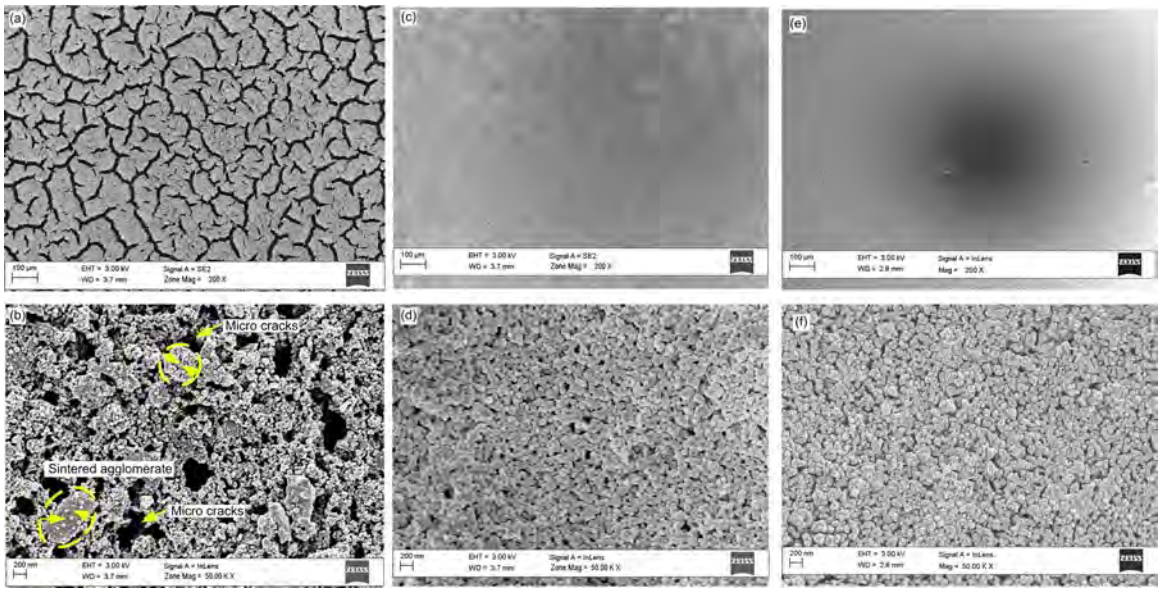

Figure 41. SEM plan view images of the coating made with (a & b) 20-30nm and (c-e) 100-200nm nanoparticles. (a-d) were sintered at 1050ºC for 4 hours. (e&f) sintered at 1050ºC for 4 hours then at 850ºC for 24 hours. All coatings were made by ACAC+Ti+0.15vol% TEA nanofluid.

Figure 41 shows the SEM surface microstructure of coatings sintered at 1050ºC. As may be seen, coatings prepared with larger particles (Figure 41 c-f) are free of cracking and the higher magnification micrograph shows some densification and sintering of the nanoparticles. In the coating made with smaller particles thought severe cracking developed after sintering. Figure 41b reveals that the main reason for such cracking is the presence of nanoparticle agglomeration. During sintering on the agglomeration site, the cluster shrinks independently from the body of the coating which induces tensile stresses between agglomerate and coating body. Since the particles form a weak bond during sintering, cracking initiates from the interface of agglomeration/coating and propagates throughout the coating. For better densification of the

coatings extended sintering was performed at 850°C for 24 hours after sintering at 1050°C for 4 hours and as it is shown in Figure 39, the coating density increased up to about 83%. Some more microcracks can be seen in the coating but no severe cracking in macro scale is visible. Sintering of the coating is constrained by the substrate, hence the degree of densification is lower in constrained sintering compared to free standing sintering. The substrate constraint the densification by its greater thermal expansion that applies tensile tension on the coating during sintering and its rigidity in the isothermal sintering step that leaves only one direction for free sintering.

Figure 42 shows the FIB cross section views and EDS line scan analysis of the YSZ coating made with 100-200nm nanoparticles and sintered at the two aforementioned sintering cycles. In the as deposited coating (Figure 42a) more porosity is visible and no clear bonding between the coating and substrate is visible. By sintering for 4 hours at 1050ºC, it is seen that at some points direct bonding between the coating and the substrate start to form (Figure 42b and 42d). However, after the extended sintering step at 850ºC for 24 hours a dense bonding interface appears between the coating and the substrate as a result of the more diffusion between the two during longer exposure to higher temperatures (Figure 42c and 42e). The porosity level is also lower after the extended sintering step which is consistent with density measurement results. No severe cracking or separation from the T91 substrate is visible. Using EDS analysis across the coating-substrate interface it is observed that the diffusion zone is about 850nm in the coating sintered for extended time while it's about 580nm in the coating sintered at 1050ºC for 4hours.

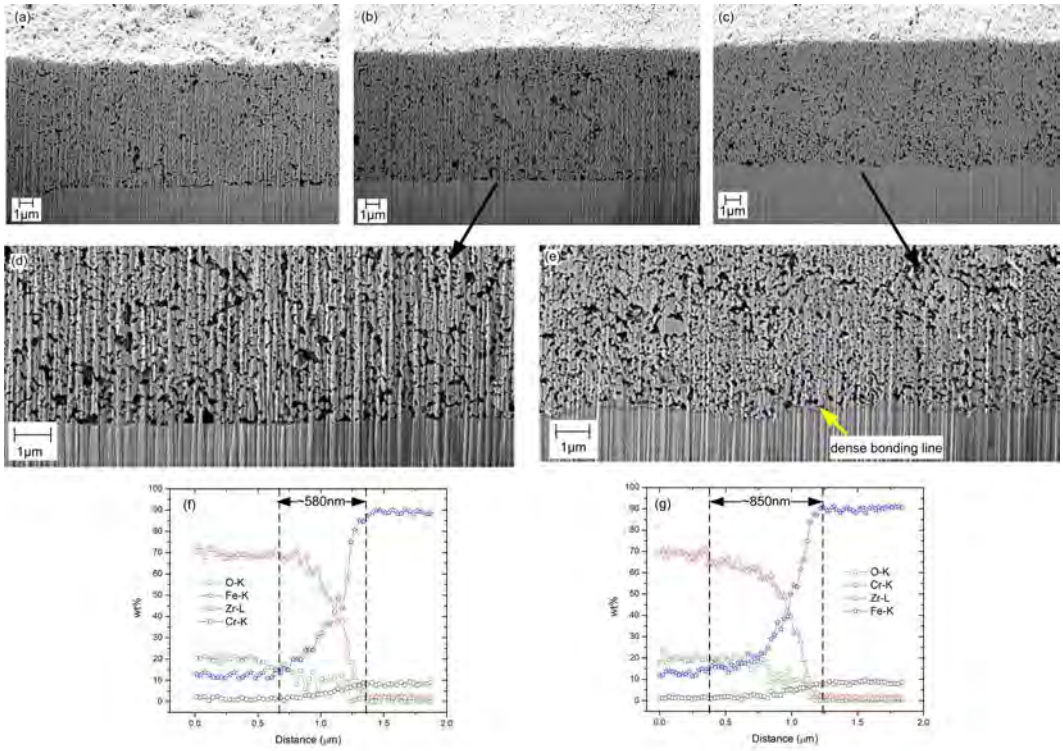

Figure 42. FIB cross section micrograph of a YSZ coating prepared with 100-200nm nanoparticles. (a) as deposited (b & d) sintered at 1050ºC for 4 hours (c & e) sintered at 1050ºC for 4 hours then 850ºC for 24 hours. (f) and (g) EDS analysis across the coating/steel interface shown in (d) and (e), respectively.

To evaluate the mechanical integrity of the coatings a scratch testing was performed on the coatings according to the procedure explained in the experimental procedure section. Figure 43 shows the SEM plan view micrographs of the scratch marks on the coatings. It can be seen that the indenter does not penetrate all the way through the coatings even in the as deposited coating (Figure 43a). The width of the scratch decreases for the sintered samples. The width of the scratch decreases from ~146µm in the as deposited to ~ 74µm in the coating sintered at 1050°C for 4 hours. The scratch mark is even smaller (60 µm) when the coating is sintered for extended time of 24 hours at 850°C.

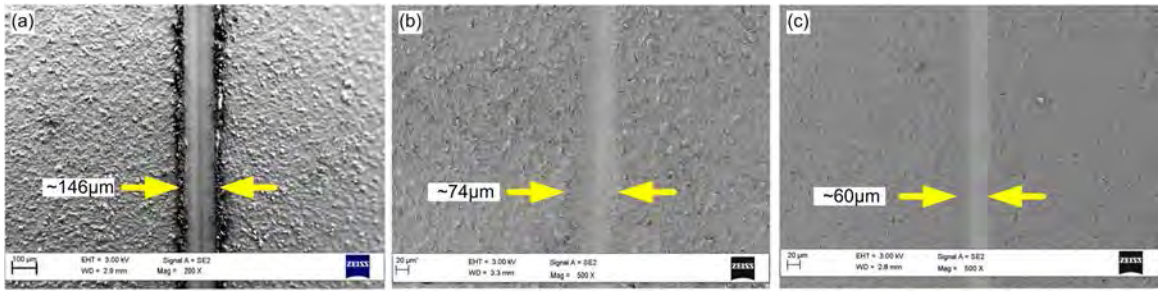

Figure 43. SEM SE plane view images of the scratch areas on the coatings made with 100-200nm YSZ in (a) as deposited and sintered (a) for 4 hours at 1050ºC and for (c) 4 hours at 1050ºC then at 850ºC for 24 hours. All coatings were prepared with ACAC+Ti+0.15vol% TEA nanofluid.

Vanadium Oxide Coatings

Since there is little literature reported on the deposition of vanadium oxide by EPD, the common parameters and recipes developed for TiO_2 and YSZ were used for vanadium-oxide (V_2O_3) deposition. It was found that V_2O_3 is more difficult to deposit than the other oxides experimented in this study, with the depositions requiring higher voltages and deposition times. Additionally, nanopowders were not readily available and particles used were in the single micron range. The difficulties encountered in depositing V_2O_3 coatings were due to a combination of the large particle size (~5µm) as well as the varying charge states of vanadium. However, after considerable experimentation it was determined that coatings could be deposited consistently from a nanofluid containing 0.25wt% V_2O_3, 0.25wt% V, 0.15 vol% TEA and 8 wt% iodine in acetylacetone (Figure 44). Vanadium-oxide was also found to sinter well at 1050ºC with evident agglomeration of particles. However, there was little increase in bonding between the steel and the coating.

Several additives were attempted in acetone and acetylacetone including iodine, TEA, sodium hydroxide, and combinations of these. It was found that the most effective deposition could be achieved when iodine (8 wt%) and TEA (0.15 vol%) were used in combination with an ACAC solvent. SEM images (Figure 45a and 45b) show a crack-free, uniform V_2O_3 coating. A higher magnification image (Figure 45b) indicates the particle size is on the order of a few microns. Although the supplier claimed the particles are 20-40 nm APS, it is evident that several of the particles were in the micron size range.

Figure 45(c-d) shows the sintering characteristics of V_2O_3 coatings. Some small cracks were evident, but the coating remains intact. Figure 45(d) indicates the particles appear to be adhering to one another.

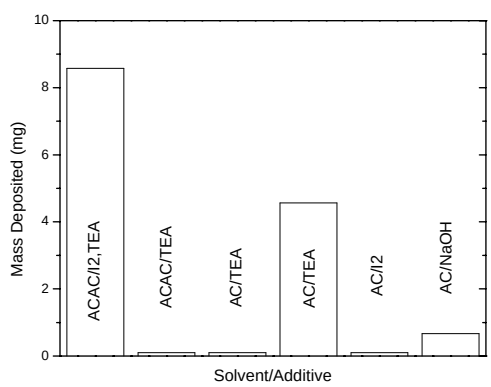

Figure 44. Effect of solvent on mass deposited. All experiments were performed with 80V applied for 5 minutes. A nanofluid containing ACAC with additives TEA and iodine produced the most massive, consistent deposits.

Although it was possible to deposit coatings, depositions were not reproducible. Approximately 50% of the nanofluids investigated did not produce deposits. In order to obtain more reproducible colloids several approaches were attempted. The suspension was allowed to

rest for 90 minutes after mixing to allow time for the TEA and iodine to react with the acetylacetone and produce charge, but this did not produce the desired results. Crushing the particles using a mortar and pestle was attempted to reduce the particle size further, but the inconsistencies continued. To overcome any issues of water absorption on particle surface, the particles were heat treated at 500ºC for 48 hours to remove this layer. Magnetically stirring of the nanofluid overnight was also attempted, but none of these methods improved the reproducibility of coatings.

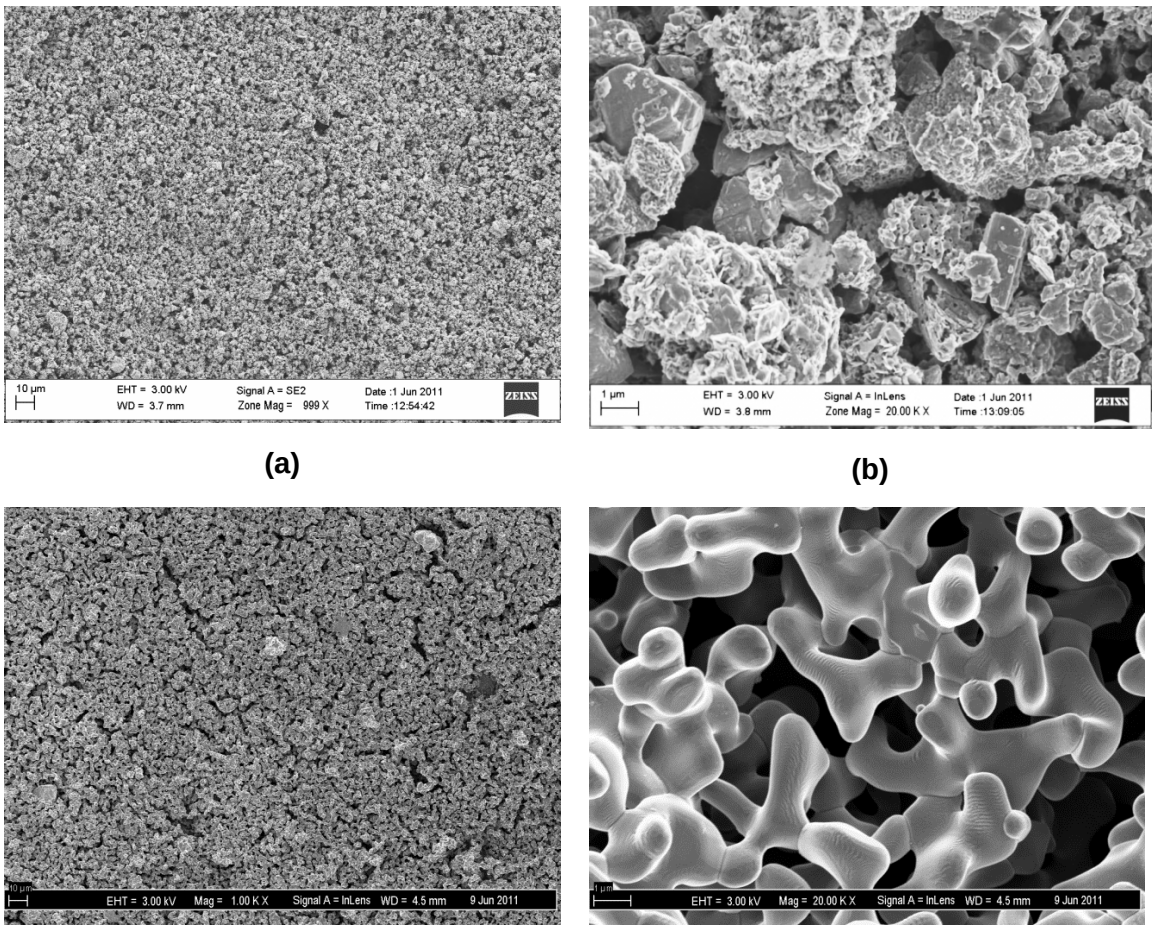

Figure 45. V_2O_3 coatings formed from an ACAC/TEA, iodine nanofluid. (a) low magnification image of as-deposited vanadium oxide coating. (b) high magnification image of as-deposited vanadium oxide coating. (c) low magnification image of sintered coating. (d) high magnification image of sintered coating. Sintering at 1050ºC or 4 hours significantly densifies the coating.

A reactive sintering step was attempted where vanadium powder mixed with Fe_3O_4 was used to create the nanofluid. The expectation was that during sintering vanadium would react with oxygen in Fe_3O_4 to form vanadium oxide. The iron would bind to the steel and provide good adhesion. This was also found to be unfeasible as iron oxide deposited much more readily than vanadium under the same conditions. Since vanadium particles are much larger (≥1 µm) than iron oxide particles (~20 nm), they deposit as large ‘lumps’ as shown in Figure 46.

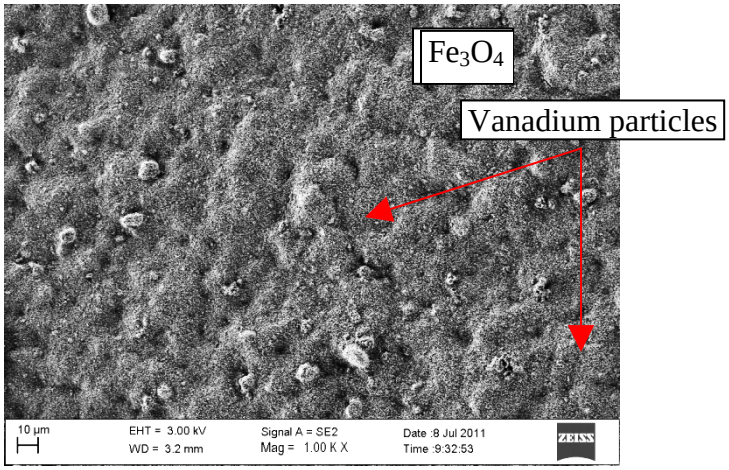

Figure 46. As-deposited V+Fe_3O_4 coating. Large vanadium particles indicate that the coating is not uniform, and would not form a uniform iron and vanadium oxide coating upon reactive sintering.

After all aforementioned unsuccessful attempts, a more reproducible method of depositing V_2O_3 was finally achieved. Upon mixing pure vanadium metal nanopowders with vanadium oxide (1:1), the reproducibility success rate increased from 50% to almost 100%. It is speculated that the vanadium acts as a catalyst to charge the vanadium oxide, while also being deposited in small quantities. Vanadium has four oxidation states: +2, +3, +4, +5. The vanadium in V_2O_3 is V^{+3}. A common method of charging particles is through adsorption of protons, but an additional step occurs due to the unique chemistry of vanadium. The vanadium oxide expels electrons, neutralizing the protons and forming H_2. The positively charged vanadium oxide can then be more easily oxidized by oxygen or water impurities in the system or atmosphere. Equation (8) shows this two part reaction.

$$V^{+3}{}_2O_3 + 4H^+ \rightarrow (V^{+3}{}_2O_3)^{+4} + 2H_2$$

$$(V^{+3}{}_2O_3)^{+4} + 2O^{-2} \rightarrow V^{+3}{}_2O_3$$

Equation (8)

When vanadium is present, it is preferentially oxidized. This allows the vanadium oxide compound to remain charged and therefore be driven to the electrode. Some of the smaller vanadium particles may also be deposited, but this is not undesirable for this application.

The V+V_2O_3 coatings appeared to be similar to the V_2O_3 coatings. It is not possible by conventional EDS analysis to determine the free vanadium present, but SEM indicates the majority of the coating is vanadium oxide. Figure 47 shows the as-deposited and sintered SEM images of V+V_2O_3 deposits.

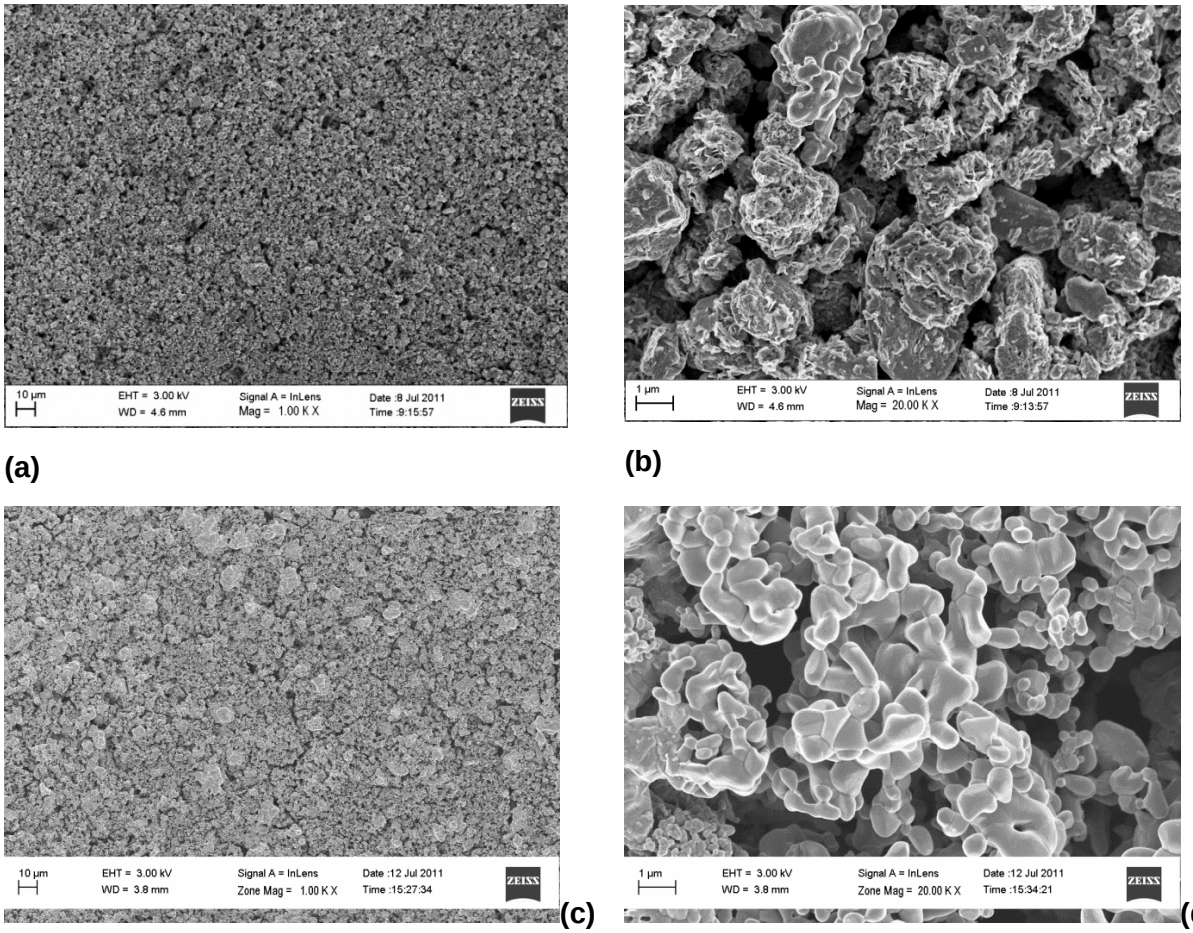

Figure 47. V+V_2O_3 coatings. (a) low magnification image of as-deposited vanadium oxide coating. (b) high magnification image of as-deposited vanadium oxide coating (c) low magnification image of sintered coating. (d) high magnification image of sintered coating. These coatings were formed from nanofluids containing 0.25wt% vanadium oxide, 0.25wt% vanadium in ACAC with 0.15vol% TEA and 8wt% iodine. Sintering occur at 1050ºC for 4 hours.

In conclusion, the optimum results were achieved with 0.25wt% V_2O_3, 0.25wt% V with 0.15 vol% TEA and 8 wt% I_2 in ACAC. Vanadium was added to absorb oxygen so that the V_2O_3 particles could remain charged and successfully deposit. Sintering at 1050ºC for 4 hours resulted in minimal cracking and increased adhesion.

Titanium Coatings

An important achievement of this project was developing a method for the deposition of pure titanium metal coating by the EPD process. As with vanadium-oxide, there was little literature on deposition of titanium by EPD process. Therefore rigorous and systematic experimentation was conducted with solvents acetone and acetylacetone with various additives to deposit titanium coatings.

The effect of several charging additives of triethanolamine (TEA, 0.15vol%), acetic acid (HAc, 2.5 vol%), and iodine (0.04wt%) on coating density (and microstructure) were studied in detail (examples shown in Figure 48 and 49).

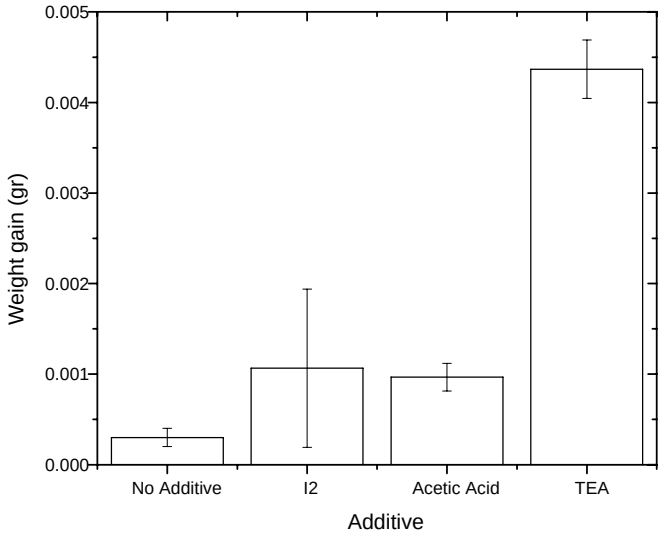

Figure 48. Effect additive on coating deposition mass. TEA made the highest deposition rate. All experiments are conducted with 0.5wt% of 30nm titanium in ACAC.

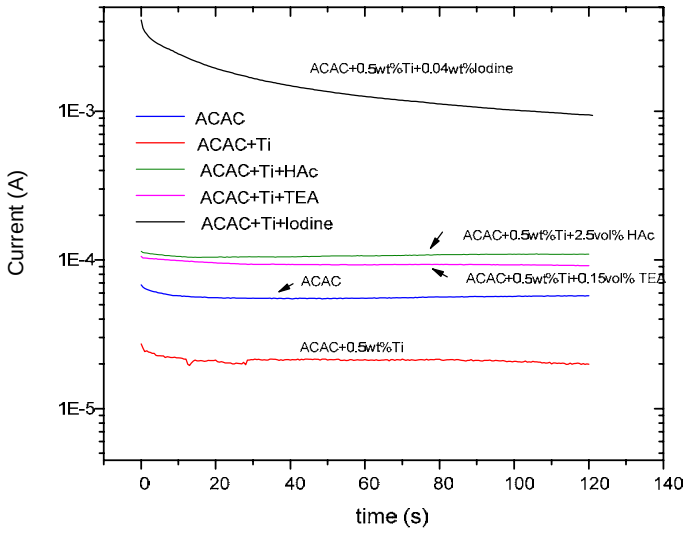

Figure 49. Current-vs-time graphs during deposition from different nanofluids. Applied voltage was 20V. Similar experiment was done on ACAC solvent as a reference.

The amount of additives was changed but we report here only those studies where highest reproducibility in coatings was achieved. The standard 0.5 wt% particle concentration was used in an ACAC solvent (0.2 gr Ti/40ml ACAC). It was concluded that the additive TEA produces the highest mass deposition and reproducible coatings for the various additives studied. TEA produces $HN^{+}(\text{-R-OH})_3$ which are absorbed on the titanium nanoparticle surface.

$$N(\text{-R-OH})_2 + ACAC \rightarrow HN^{+}(\text{-R-OH})_2 + ACAC^{-} \qquad \text{(Equation 9)}$$

Hence, the nanofluid including ACAC+0.5%Ti+0.15vol%TEA was selected to prepare coatings for all other experiments. In order to avoid the effect of the thickness on the density and properties of the coatings, the thicknesses of all coatings have been kept constant at 9-10 microns. Two particle sizes of 30-50nm and 60-80nm range were investigated. For coatings prepared with 30-50 nm particles, it was observed that thicker coatings generally resulted in more cracks. Cracks formed when the coating thickness exceeded approximately 8µm. It was found that varying voltage from 20-80V did not affect the cracking threshold. Figure 50 illustrates these effects.

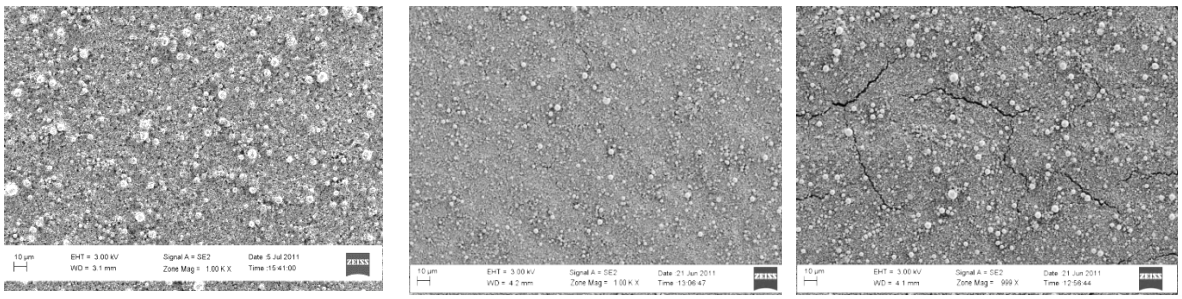

(a) (b) (c)

Figure 50. Titanium coatings of varying thickness (a) 1.9µm. (b) 5.4µm (c) 9.7µm. The 9.7µm coating forms cracks, indicating the cracking threshold is between 5 and 9.5µm. Coatings were deposited from a nanofluid containing ACAC and TEA.

There was some concern that we may be depositing TiO_2 since titanium nanoparticles may have oxidized in air or in the nanofluid. In fact, there was some oxidation, as a thin oxide layer provides a surface for the charged particles (i.e. protons) to adsorb on to. That said, significant oxidation of the nanoparticles did not occur as the coating was confirmed to be titanium by SEM EDS, with a very little amount of oxygen present (Figure 51a). The titanium coating showed 99.4% titanium and 0% oxygen. Similar TiO_2 coatings showed a pronounced oxygen signal (Figure 51b).

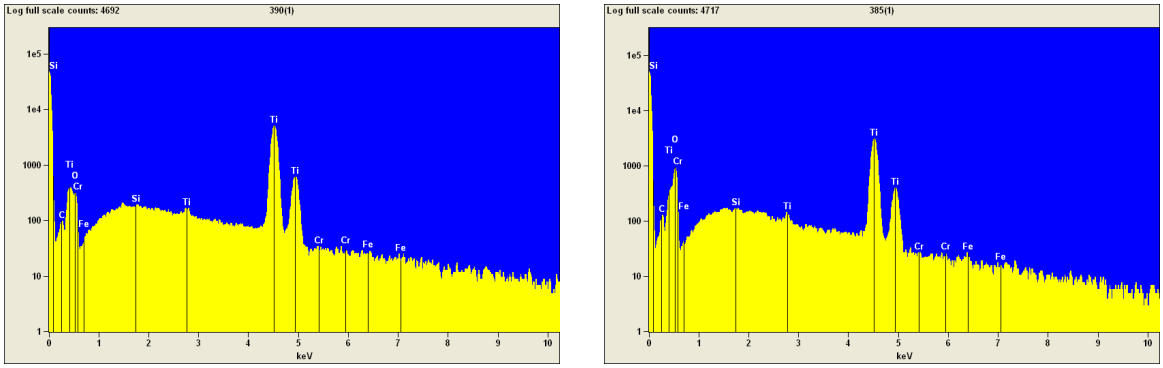

(a) (b)

Figure 51. EDS spectrum of (a) titanium coated sample. Titanium peaks are obvious between 4 and 5 keV (b) titanium oxide coating. Titanium peaks are obvious between 4 and 5 keV and oxygen peak is present near 0.5keV.

For deposition of titanium coatings, 60-80nm particles were also used. Figure 52 compares the as deposited and sintered (at 1050 ºC, in vacuum) densities of the coatings made with the two particle sizes.

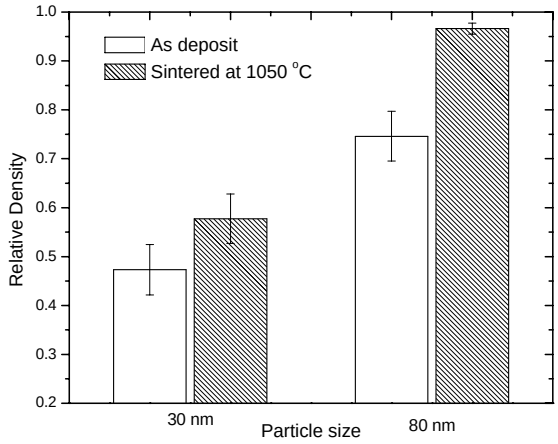

Figure 52. Effect of Particle size and sintering on titanium coating density. The larger particles produce denser coatings, both before and after sintering 1050 ºC because larger particles do not form agglomerates in the nanofluid. All depositions were formed from nanofluids containing ACAC and 0.15 vol% TEA.

Figure 53 shows the plan view SEM images of the as deposited coatings. It may be noted that more agglomeration in the smaller particles, even though both coatings with thicknesses about 9µm are crack free. More particle agglomeration in the smaller particles reduced the proper particle arrangement and high packing which resulted in the significant lower density of the coatings.

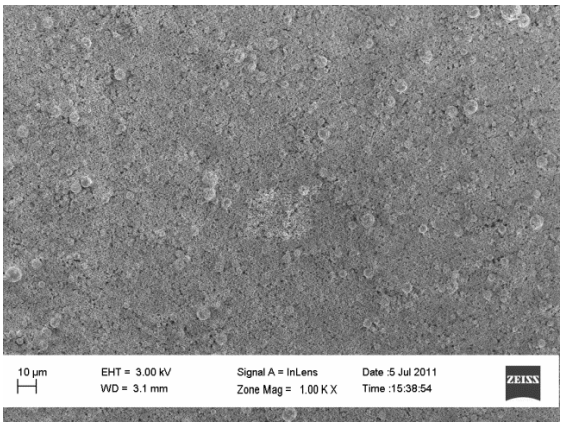

(a)

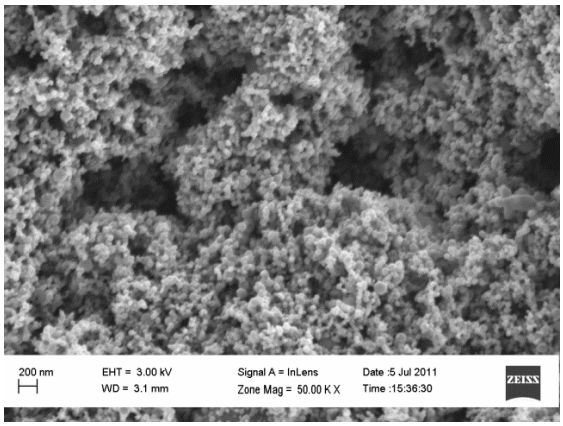

(b)

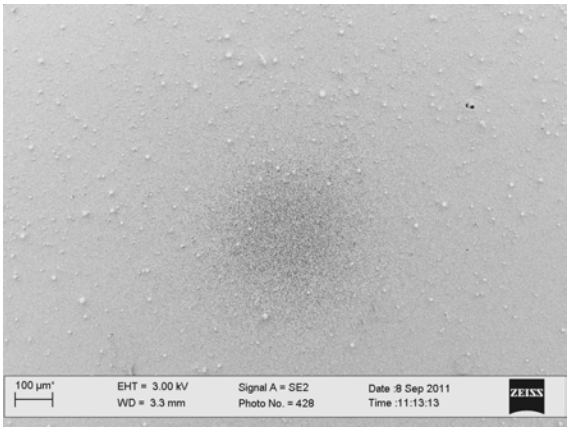

(c)

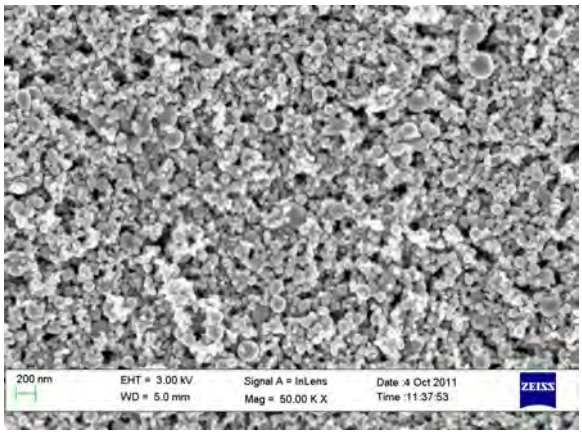

(d)

Figure 53. Titanium coatings. (a) 1000X image of as-deposited coating. (b) 1000X image of sintered coating. (c) 50,000X image of as-deposited coating. (d) 50,000X image of sintered coating. Coatings were deposited from a nanofluid containing ACAC and TEA.

Figure 54 shows the plane view images of coatings sintered at 1050ºC. In these coating unlike the other coating materials, a sintering step at 700ºC for two hours was conducted prior the final sintering for 4 hours at 1050ºC. The coating prepared with lager particles (Figure 54a & b) is free of cracks and the higher magnification image shows very good densification of the particles and formation of grain boundaries by sintering of the nanoparticles. In the coating made with smaller particles though, cracks developed after sintering. Higher magnification images of the crack free regions (Figure 54 d) shows that formation of bigger grains compared to the coating made with larger particles. This is attributed to the smaller particle size and more driving force for sintering due to curvature and surface energy. Figure 54e shows that the main reason of the cracking of the coating prepared with smaller particles is agglomeration. Once there is a agglomeration, during sintering the agglomerate cluster shrinks independent from the body of the coating which causes tensile stresses between cracking and since the particle joining during sintering is weak cracking initiate from the agglomeration sites and propagates through the coating.

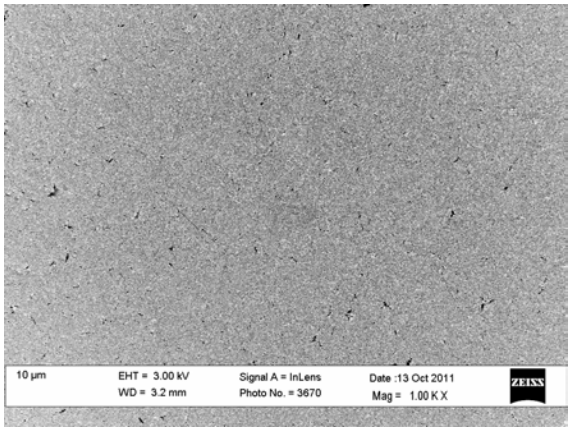

(a)

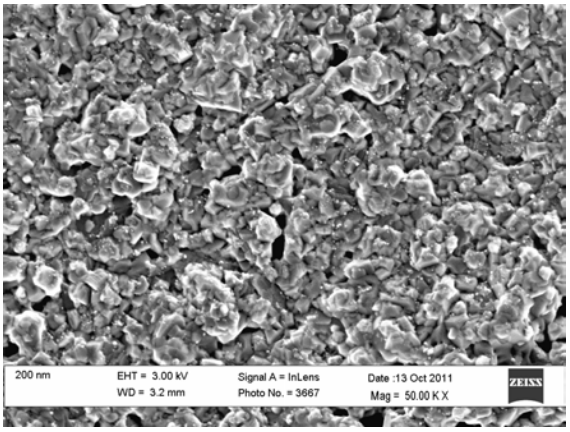

(b)

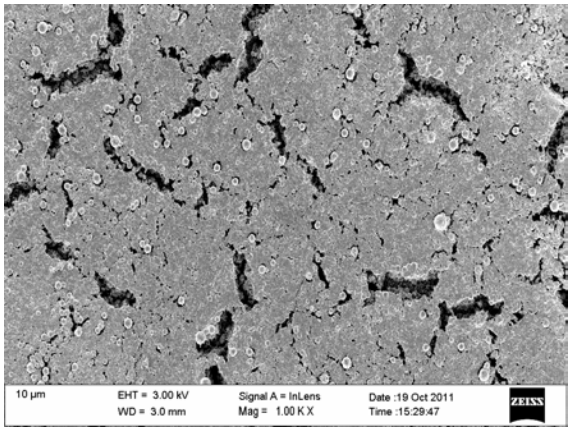

(c)

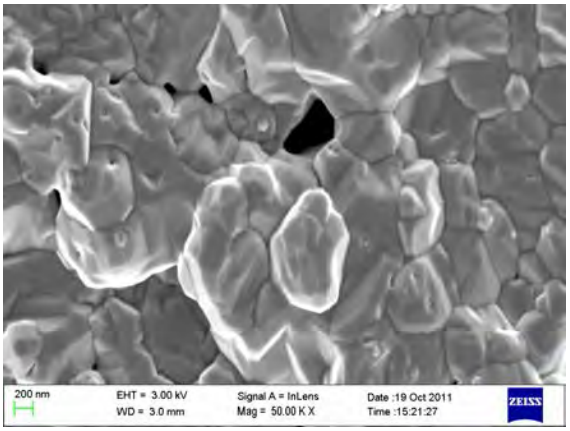

(d)

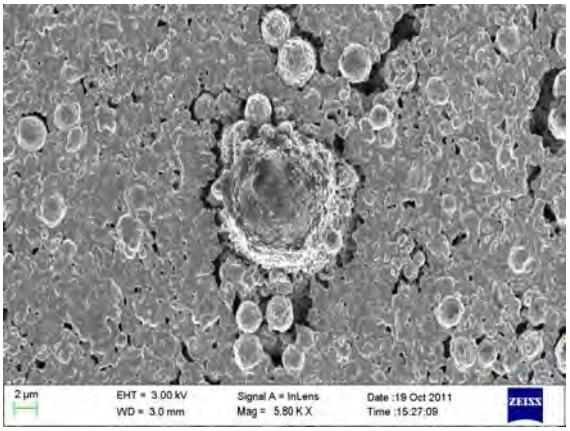

(e)

Figure 54. SEM plan view images of the coating made with (a & b) 80nm and (c-e) 30nm particles. coatings were sintered at 1050ºC.

To evaluate the possibility of sintering of the coatings at other temperatures, coatings were also sintered at 950ºC and 850ºC. Figure 55 compared the resulting densities of the coatings. It

was found that even with sintering at 850ºC, coating with about 84% theoretical density with good bonding to T91 steel can be produced. Sintering at lower temperature can significantly reduce the high temperature effects of the microstructures of T91 steel which is very favorable.

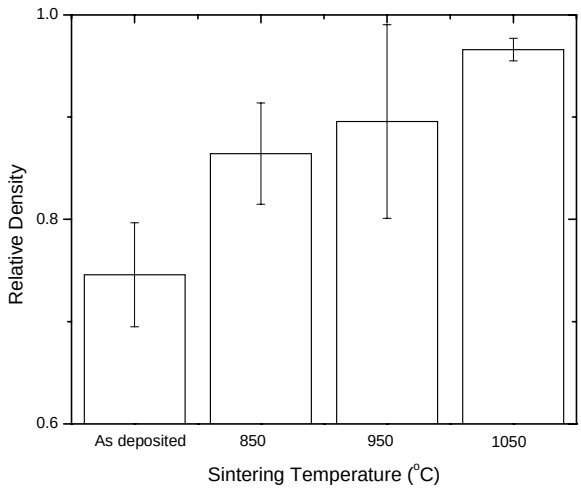

Figure 55. Effect of Sintering temperature of the density of the coatings made with 60-80nm titanium nanoparticles.

Figure 56 shows the FIB cross section view and EDS line scan analysis of the titanium coating made with 60-80nm nanoparticles and sintered at 1050ºC for 4 hours and 850ºC for 15 hours. One can notice well adhered and densified coatings. Porosity level is almost the same in both coatings which is consistent with density measurement results. No cracking or separation from the T91 substrate is visible. Using EDS analysis across the coating-substrate interface it is observed that the diffusion zone is about 900nm in the coating sintered at 850ºC for 15 hours while it's about 500nm in the coating sintered at 1050ºC for 4hours. However, the densification of both coatings are the same or even slightly more in the latter case. Higher diffusion in the former can be due to the fact that at 850ºC the T91 steel is still in the ferritic phase regime and has BCC crystal structure while at 1050ºC due to austenitic phase transformation the crystal structure changes to FCC.

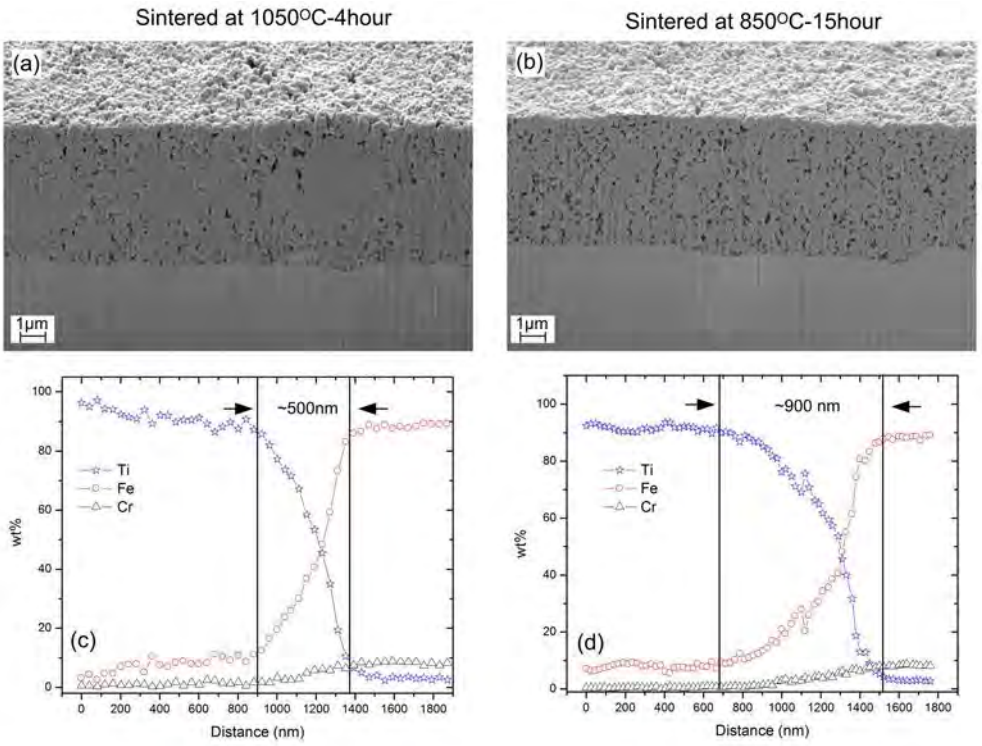

Figure 56. FIB cross section and EDS analysis across the coating-substrate interface of the coatings made with 60-80nm nanoparticles and sintered at (a & c) 1050ºC for 4 hours and (b & d) 850ºC for 15 hours.

To evaluate the mechanical integrity of the coatings scratch tests were performed on the coatings according to the procedure explained in the experimental section earlier. Figure 57 shows the SEM plan view micrographs of the scratches coatings that were tested under similar conditions. The indenter did not penetrate the coatings even in the as-deposited coating (Figure 57a). Furthermore, the width of the scratch decreases as the sintering temperature increases which is consistent with density measurement results. In the coating sintered at 850ºC for 15 hours thought, the width of the scratch is almost the same as the one sintered at 1050ºC for 4 hours even though the sintering temperature is significantly lower. On the other hand, some microcracks can be seen close to the scratch marks in the latter case even though the densities of the coatings are very close. This suggests that improved mechanical integrity may be achieved by sintering at lower temperature and longer times.

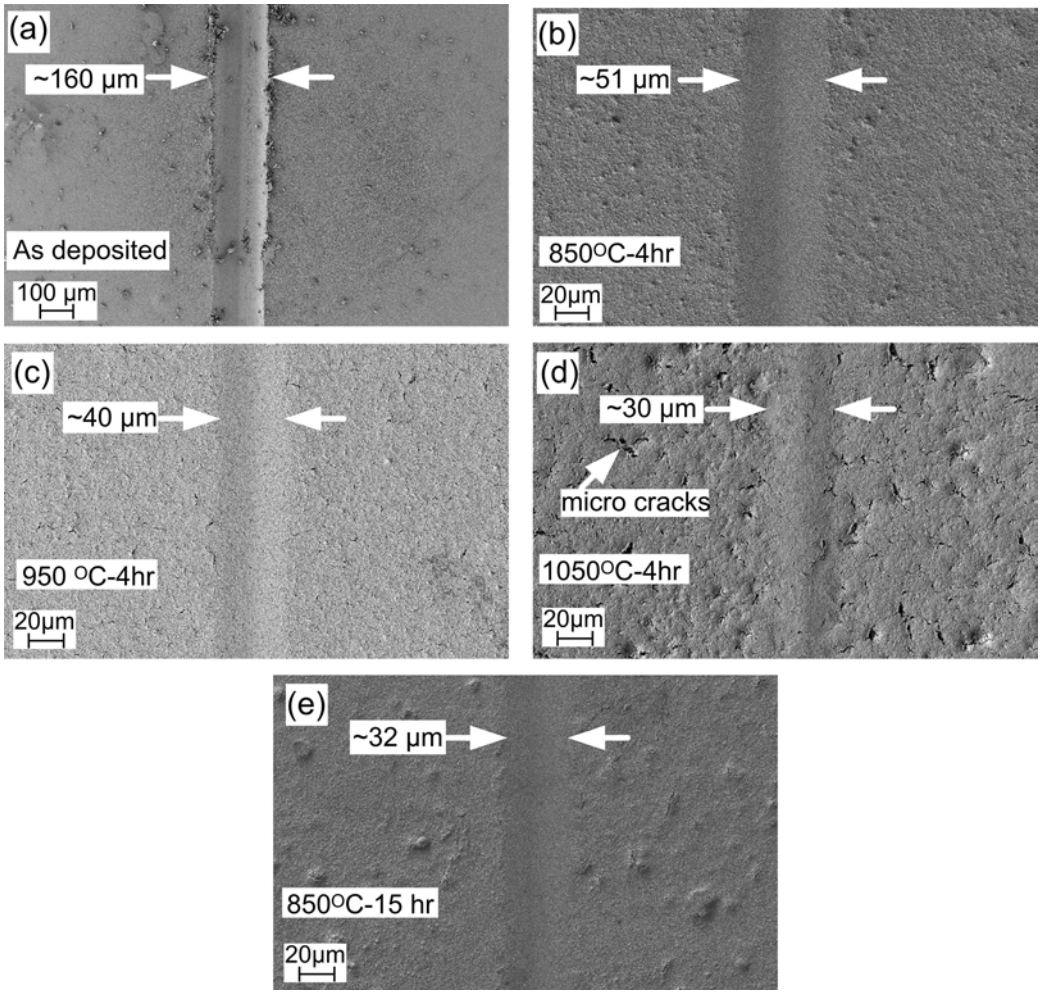

Figure 57. SEM images of scratches on the coatings made on titanium coatings (a) as deposited and (b) sintered for 4 hours at 850ºC (c) sintered for 4 hours at 950ºC (d) sintered for 4 hours at 1050ºC and for (e) sintered for 15 hours at 850ºC. Coatings were prepared by ACAC+Ti+0.15vol% TEA nanofluid and were about 9-10µm thick.

In conclusion titanium was successfully deposited by the EPD process using a mixture of TEA in ACAC. A thin oxide layer allows charge production and adsorption of charged species on the titanium nanoparticles. Coatings made with larger particles (60-80nm) had both higher green density and less agglomeration compared to ones made with smaller particles (30-50nm). Crack free coatings with excellent bonding to T91 steel were prepared by sintering the coatings made with 60-80nm particles at temperatures ranging from 850-1050 ºC.

Zirconium Coatings

As with titanium and vanadium oxide, rigorous experimentation was performed to identify the parameters for electrophoretic deposition of pure zirconium coatings. Solvents acetone and ACAC with additions of TEA, iodine, and water were investigated. Nanofluids with iodine, TEA, or both iodine and TEA produced deposits. However, iodine additions resulted in significant variations in deposition rates between experiments. Suspensions of 0.15 vol% TEA in ACAC produced consistent, uniform deposits. One of the set-backs here was the non-availability of

nanometer-sized particles of zirconium. The smallest zirconium particles available were several microns in size, so the coatings are not as uniform as they would have been with nano-sized zirconium powder.

SEM/EDS investigation clearly confirmed the coating formed was that of zirconium, with little evidence of oxygen. However, sintering in even high vacuum furnaces at 1050ºC or even 850ºC resulted in significant undesirable oxidation of zirconium coating.. Investigation using SEM/EDS (Figure 58) shows clearly that the particles are much larger (several microns in diameter) than the 80nm APS claimed by the powder supplier. Despite this, coatings were still successfully deposited. For future work, it is speculated that if smaller particles could be fabricated, then more uniform and dense coatings of zirconium could be deposited.

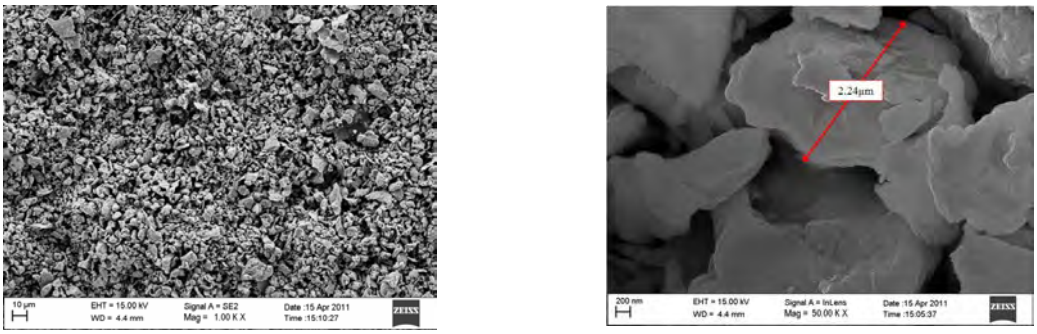

(a) **(b)**

Figure 58. SEM of a 15 µm thick zirconium coating at (a) low magification and (b) high magnification. In both micrographs it is obvious that the particles size is much larger than 80nm as claimed by the manufacturer. Coating was deposited from an ACAC/TEA nanofluid.

As with titanium, it is assumed that a very thin oxide layer forms on the zirconium particles to allow production and adsorption of charge. SEM/EDS analysis showed the coating was comprised of 99% zirconium with trace amounts of iron from the substrate (Figure 59). X-ray diffraction also confirmed that this is in fact pure zirconium, with a small iron peak, presumably from the steel substrate.

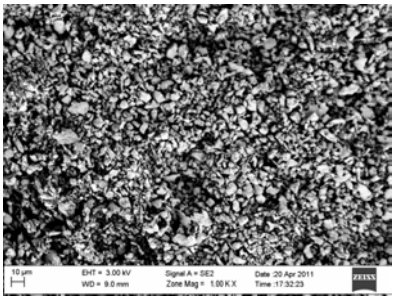

(a)

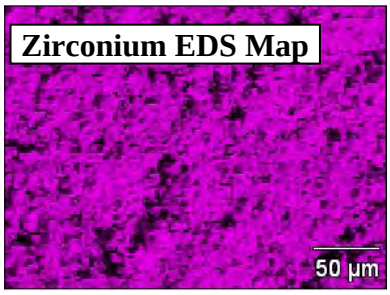

(b)

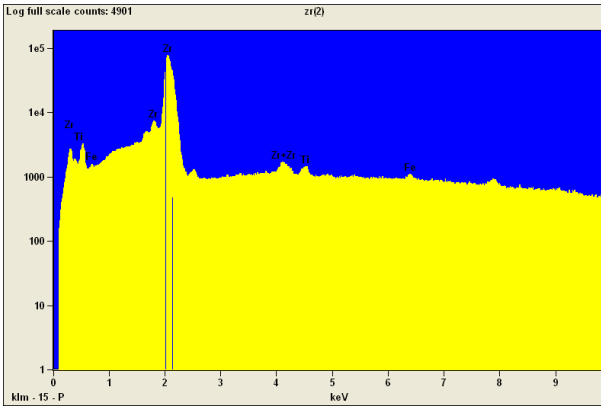

(c)

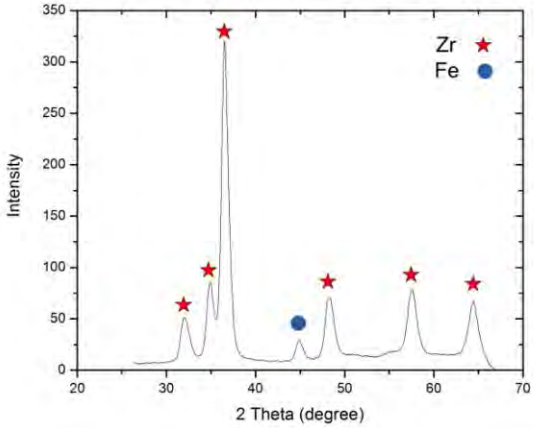

(d)

Figure 59. (a) SEM of zirconium coating with (b) corresponding zirconium elemental x-ray map. (c) EDS analysis of the zirconium coatings and (d) x-ray diffraction spectrum. Analysis confirms the coating is zirconium, with the only other significant signal originating from the iron in the steel substrate.

In conclusion, this set of experiments has shown that zirconium coatings (with only trace amounts of oxygen) can, in theory, be deposited through electrophoretic deposition from a mixture of 0.5 wt% zirconium and 0.15 vol% TEA in ACAC. If smaller particles could be obtained, denser, more uniform coatings could potentially be produced. Sintering may also be possible, but a very high vacuum ($<10^{-5}$ torr) or strongly reducing atmosphere would be necessary. Lower sintering temperatures may also be explored as part of future studies.

Vanadium Coatings

We performed extensive experiments to deposit vanadium coatings, in light of the fact that vanadium has been shown to an effective diffusion barrier material to mitigate FCCI in previous studies. However, vanadium exhibited the greatest inconsistency in deposition of all the materials investigated in this study. As with the other metals, no literature references were available for EPD of vanadium. After much experimentation, consistent coatings could be deposited from vanadium particles suspended in a mixture of ACAC, acetic acid, and iodine while the solution was magnetically stirred. The deposited coating sintered extremely well, showing excellent signs of agglomeration during sintering.

Determining a suitable nanofluid to deposit vanadium was challenging. Initially, the common mixtures of ACAC and iodine or TEA were experiments but were unsuccessful. After this, several additives including iodine, TEA, sodium hydroxide, water and acetic acid were added to acetone, ACAC, and ethanol. A deposit was formed from a combination of 8 wt% iodine (0.08%mass of powder) and 5 vol% acetic acid in ACAC. The average mass deposited with each suspension is shown in Figure 60.

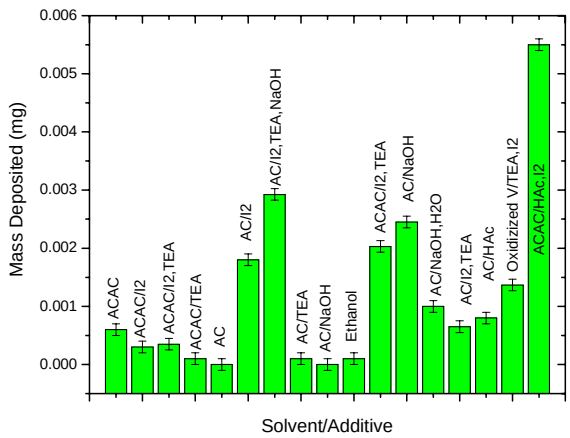

Figure 60. Various nanofluids investigated for vanadium coating deposition. The solvent ACAC with additives acetic acid and iodine produced the most uniform deposits.

As with vanadium oxide, an ‘incubation’ period of 90 minutes was attempted to allow time for the charge producing or adsorbing reactions to occur. The particles were also crushed with a mortar and pestle under the assumption that smaller particles have higher surface area so that more charge can be adsorbed per unit mass. Particles were also oxidized by mixing with water, and then allowing the water to dry in hopes that the slightly thicker oxide could produce or adsorb more charge, but this approach was not successful.

Finally, depositions were successfully produced while the suspension was being stirred continuously on a magnetic stirrer. Using this method, a reproducibility rate for coating deposition of 70% was achieved. Observation of the microstructure of these coatings (Figure 61) may explain why this method is effective. The larger particles are on the order of 5 µm, which is at least twice as large as the largest particles observed in other coatings. The deposited particles are most likely the smallest particles in the mixture, as the large particles would have too large of a mass to surface area ratio, and would be expected to sediment. As the large particles sediment, they may trap smaller particles that would normally be suspended and produce a coating. Stirring allows the smaller particles to escape and eventually form a deposit.

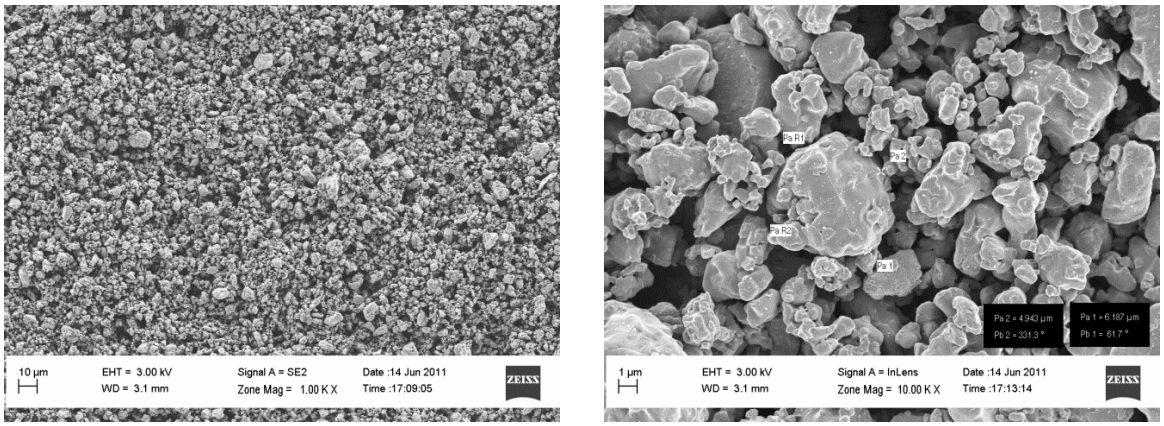

(a) **(b)**

Figure 61. SEM images of vanadium coating at (a) low magnification and (b) high magnification. It is clear the particle size is larger than 100nm, as claimed by the manufacturer. Coating was formed from a nanofluid containing ACAC with acetic acid and iodine.

In order to confirm the composition of the coating, SEM/EDS analysis was performed to obtain an elemental spectrum (Figure 62). This showed almost 75 at% of the coating to be vanadium with the rest being mostly oxygen.

In order to increase adhesion and density, vanadium coatings were sintered at 1050ºC for 4 hours. Sintering was very effective in promoting cohesion between particles. Figure 63 compares as-deposited and sintered vanadium coatings. Though a significant sintering effect is observed, the coating did not adhere to the steel substrate; the entire coating and flaked off but remained in one piece.

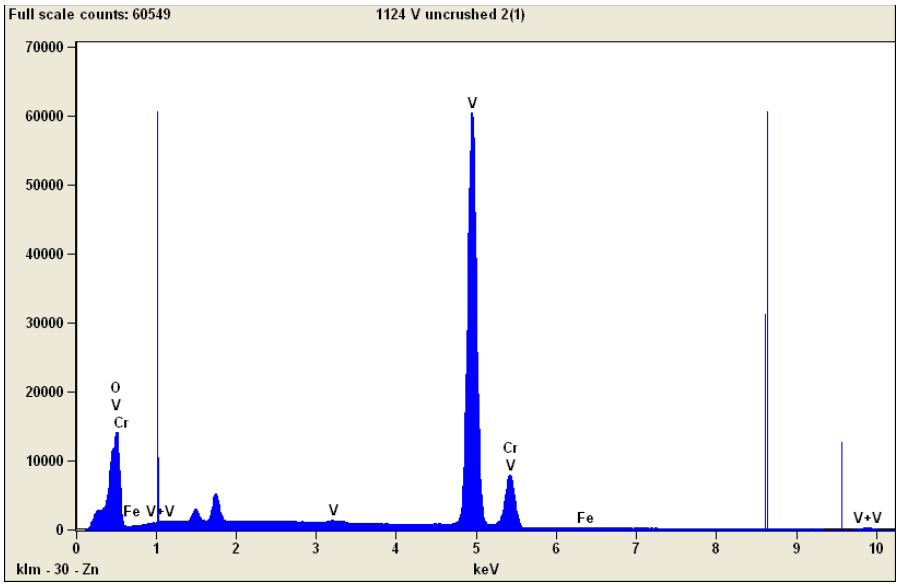

Element Line	Weight %	Weight % Error	Atom %	Atom % Error
O K	9.3	+/- 0.2	24.7	+/- 0.6
V K	90.1	+/- 0.3	74.8	+/- 0.3
Cr K	0.3	+/- 0.1	0.2	+/- 0.0
Fe K	0.3	+/- 0.0	0.2	+/- 0.0

Figure 62. EDS spectrum of vanadium coating showing that the majority of the coating is vanadium, with some portion being oxide, presumably from vanadium oxide. Coating was produced from a nanofluid containing ACAC with the additives acetic acid and iodine.

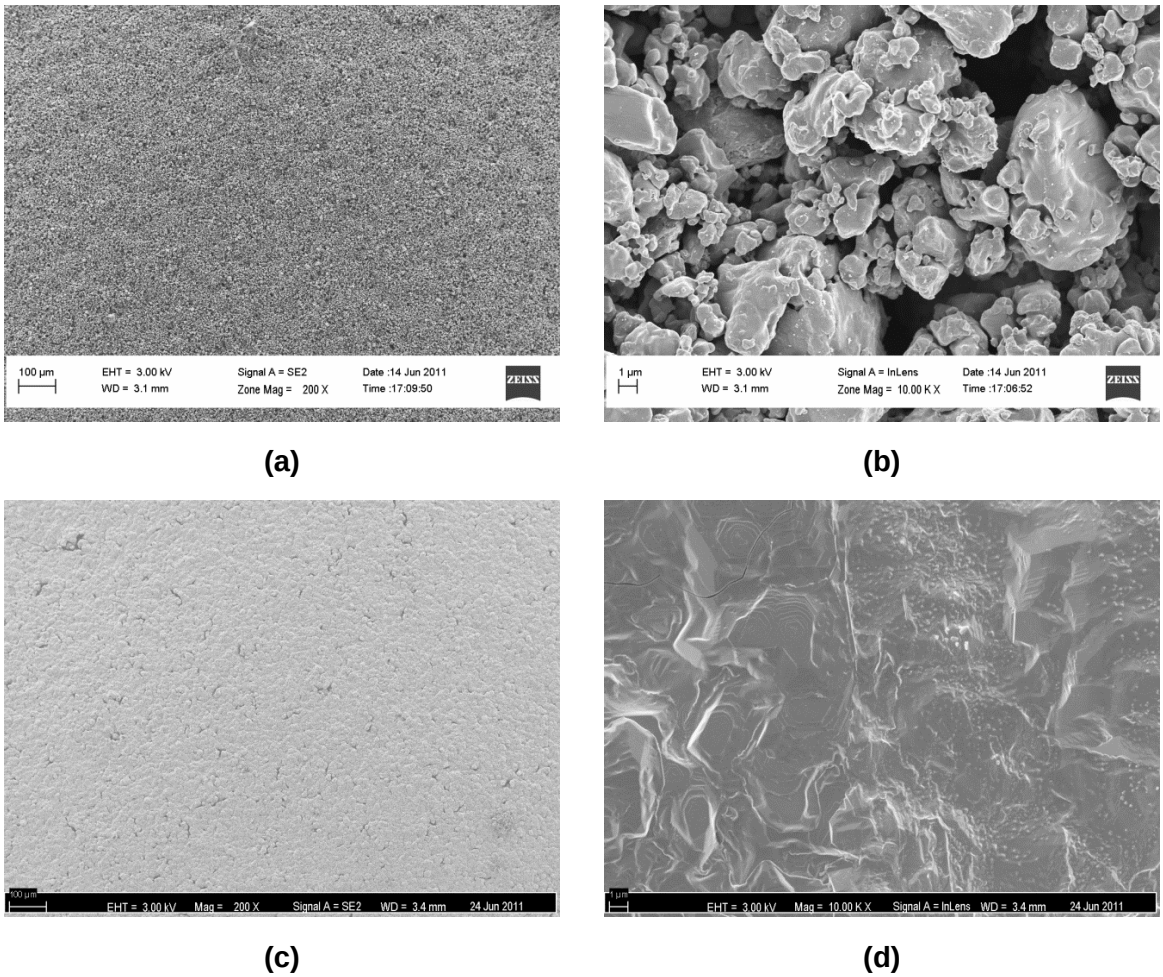

Figure 63. SEM micrograph of as-deposited vanadium coating at (a) 200X and (b) 10,000X and sintered coating at (c) low magnification and (d) high magnification. Good particle sintering is seen after heat treating at 1050ºC for 4 hours. Coating was produced from a nanofluid containing ACAC with the additives acetic acid and iodine.

In conclusion, a vanadium deposit could be formed the EPD process using a mixture of ACAC, acetic acid, and iodine that was magnetically stirred. If smaller particles could be procured, a more uniform, dense coating could be produced more consistently. Upon sintering at 1050ºC for 4 hours, the particles sintered well to each other, but not to the substrate. Methods for enhancing adhesion of the vanadium coating to the substrate warrant further investigation.

Titanium Nitride Coatings

Titanium nitride is also a promising barrier coating for FCCI and was investigated in this study by rigorous experimentation. Uniform coatings could be produced with 0.5 wt% TiN particles in ACAC with addition of 0.15 vol% TEA. Limited experiments showed that the threshold for cracking on these coatings is only a few microns and sintering generally promoted crack formation.

Figure 64 shows how the crack density increases as the thickness increases. This cracking threshold is thought to be between three and four microns. Sintering was attempted with a thin, one micron TiN coating. Figure 65 compares the microstructure of as-deposited and sintered TiN coatings. The small 20nm particles show good sintering ability as shown in the high magnification images in Figure 65 (b) and (d).

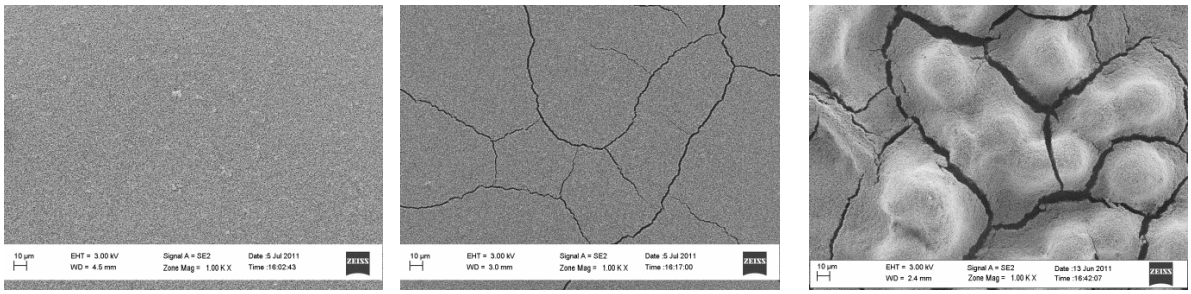

(a) **(b)** **(c)**

Figure 64. Titanium nitride coatings of varying thickness at 1000X. (a) 1.3µm. (b) 3.8µm (c) 7.2µm. Thicker coatings tend to form cracks due to increased stress. The cracking threshold for TiN coatings is between 1 and 4µm. Coatings were formed from a nanofluid containing acetylacetone and TEA.

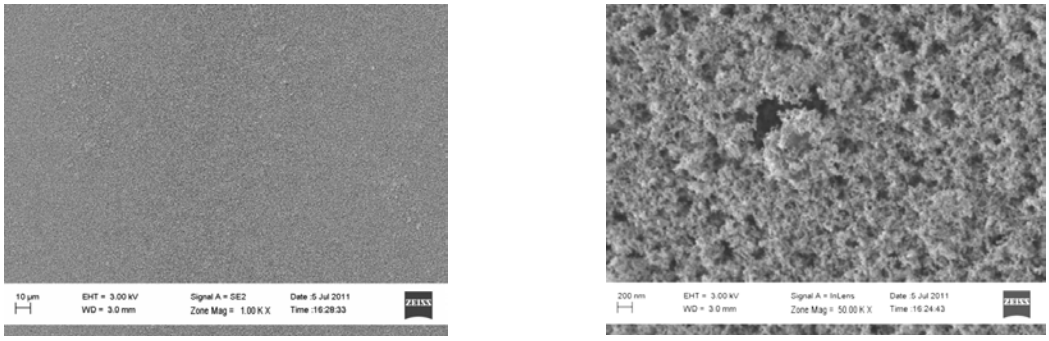

(a) **(b)**

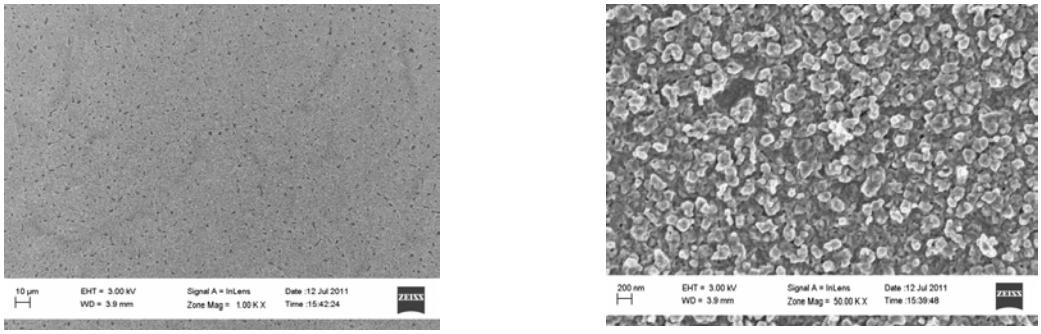

(c) **(d)**

Figure 65. SEM images of titanium nitride coating at (a) low magnification and (b) high magnification prior to sintering and after sintering at 1050ºC for 4 hours at (c) low magnification and (d) high magnification. The small (20nm) TiN particles sinter well. Deposits were formed from a nanofluid containing ACAC and TEA.

In conclusion, titanium nitride has the potential to be deposited by EPD using a mixture of TEA and ACAC with a concentration of 0.5wt% 20nm TiN particles. Coating thickness must be kept below 5µm as there is a tendency in thicker coatings to form cracks. Initial experiments show that sintering can densify the coating and promote adhesion to the steel substrate. Further experiments should be conducted to determine how the cracking threshold can be increased and to study the effects of sintering more comprehensively..

VII.C. Electrophoretic Deposition on the Inner Surface of Cladding Sections using the Coaxial Electrode Configuration

An important contribution of this project is the development of a technique to successfully coat the inner surfaces of fuel claddings. The coating methodology developed for deposition on sample test flats was modified for deposition on inner surfaces of steel used as a surrogate for cladding material (4mm in inner diameter and 12” in length). As discussed in the experimental section of this report, this was achieved using a co-axial titanium electrode (2mm diameter). It was found that coatings of TiO_2, YSZ, zirconium, and titanium could be deposited uniformly on the entire 12” length section of the inner surface of the cladding. It is speculated that with some refinement of deposition parameters, deposition of other coatings such as those of vanadium and V_2O_3 should also be possible. We believe that this is a significant accomplishment of this study. Based on the successful depositions on 12” length cladding sections, the scientific proof-of-principle has been established and it is a matter of incorporating technological modifications (fixtures, power supply, etc.) to successfully coat the inside surface of the entire length of cladding.

TiO_2 coatings were initially produced on the inner surface 2 and 6 inch long steel tubes. To facilitate the ready examination of coating uniformity, the tubes were cut longitudinally into two hemispherical halves by the EDM technique prior to deposition, then re-coupled together tightly with Teflon and electrical tape. After coating deposition, the two halves were readily separated and the uniformity of deposit on the inner surface of the tubes was examined. The depositions utilized the optimum mixture as determined by flat coating experiments. The voltage was kept at 20 V or 40 V depending on the conductivity of the mixture. The larger surface area of the 12 inch cladding (1.89 in^2 vs 0.25 in^2) limits the ability of the power supply to monitor and supply the current.

Coatings of titanium, TiO_2, zirconium, and YSZ were successfully produced on the inner surface of claddings. Photographs of the inner surface of 12” sections with coatings of various materials are shown in Figure 66. The coating is uniform along the entire 12 inch length of the simulated cladding section.

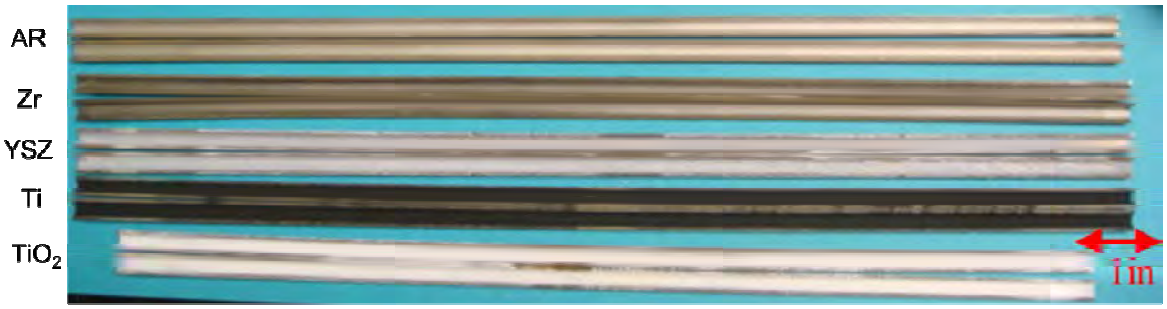

Figure 66. Photograph of the coated inner surface of the 12" cladding sections showing uniform coating along the entire length of the cladding section (AR: as-received, no coating).

A higher magnification photograph (Figure 67) shows that the coating is uniform and crack free in each case. These experiments indicate that with additional experiments the EPD process can be used to deposit coatings on the inner surface of SFR fuel claddings.

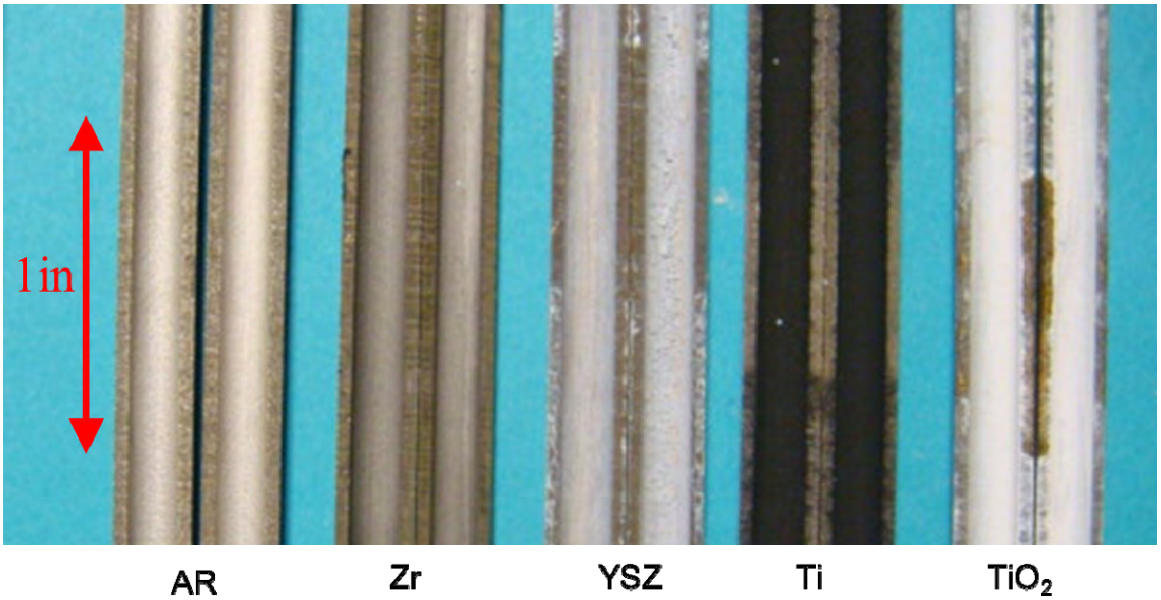

Figure 67. Higher magnification photograph of coated cladding substitute. Deposit shows minimal cracking and uniform coverage on the inner surface of the claddings.

VII.D. Diffusion Couple Experiments

Initial Experiments

The diffusion barrier characteristics of the coatings formed by EPD are crucially important for the FCCI application. For the diffusion couple studies, cerium was used as surrogate for metallic uranium fuel because of their similar physical properties. Among the property requirements of the diffusion barrier material is that it have low mutual solubility with the fuel material on one side and steel on the other. In order to determine the time and temperature for the diffusion couple experiments, several initial experiments with cerium sandwiched between two uncoated samples of T91 steel were performed. As the cerium-iron phase diagram (Figure 68) shows, a

eutectic reaction occurs at 592ºC. Due to alloying elements in the steel, this eutectic reaction would likely occur even below this temperature, so a temperature of either 560ºC or 585ºC was selected for our diffusion couple experiments. A diffusion time of 100 hours at 560ºC or 40 hours at 585ºC produced adequate and measureable diffusion lengths.

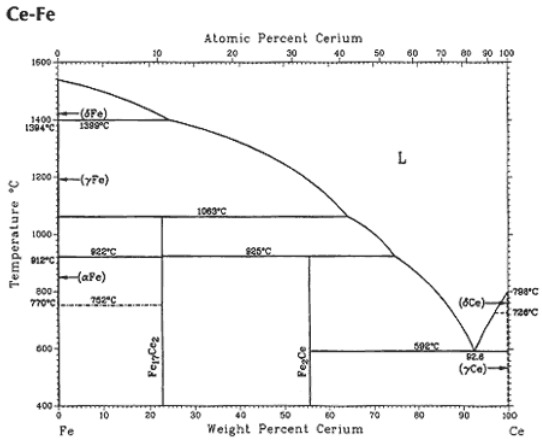

Figure 68. Iron-cerium phase diagram. Eutectic point is at 592ºC. In order to avoid eutectic melting, experiments were performed at or below 585ºC.

First, experiments were performed above the eutectic region to identify characteristics of eutectic melting in this system, at 700ºC for 48 hours. Figure 69 shows severe grain growth near the iron-cerium interface as well as the large amounts of inter-diffusion between iron and cerium. These gross changes in interfacial microstructure result from liquation at the interface, as is predicted by the phase diagram shown in Figure 68. Cerium was found to diffuse across the entire sample with 1wt% cerium detected 1 mm from the original interface.

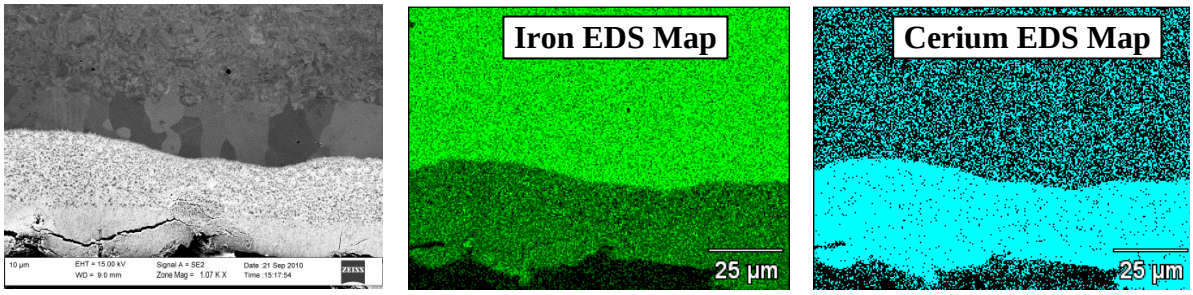

(a) **(b)** **(c)**

Figure 69. Diffusion couple studies between cerium and uncoated T91 steel performed at 700ºC for 48 hours (a) SEM micrograph showing grain growth and melting and corresponding (b) iron and (c) cerium EDS map.

The next experiments were aimed at determining an adequate time and temperature such that the diffusion length of an uncoated sample would be on the order of tens of microns, but not traverse the entire thickness of the cerium sample and influence diffusion characteristics at the other interface. These tests were performed at a temperature of 560ºC for 100 hours.

Due to time constraints on the furnace use, the possibility of operating at a higher temperature for less time was also investigated. One experiment performed at 590ºC for 50 hours produced significant diffusion without formation of a eutectic compound (Figure 70).

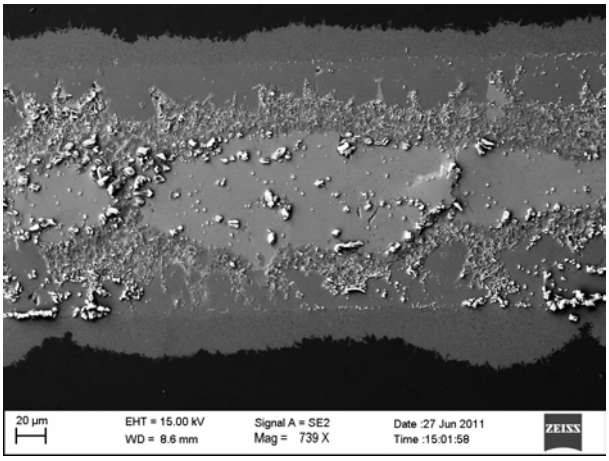

Figure 70. Micrograph of the interfaces after test diffusion couple performed with two pieces of bare T91. This experiment was performed at 590ºC for 50 hours.

ImageJ was utilized to evaluate the average diffusion length in each diffusion couple. The threshold and outline functions were utilized to distinguish the diffusion area. Figure 71 clearly illustrates how this method differentiates the area of diffusion from the remaining sample. The average diffusion length was then calculated by dividing the diffusion area by the length of sample investigated. The average diffusion length for the top interface of this uncoated sample is 44µm.

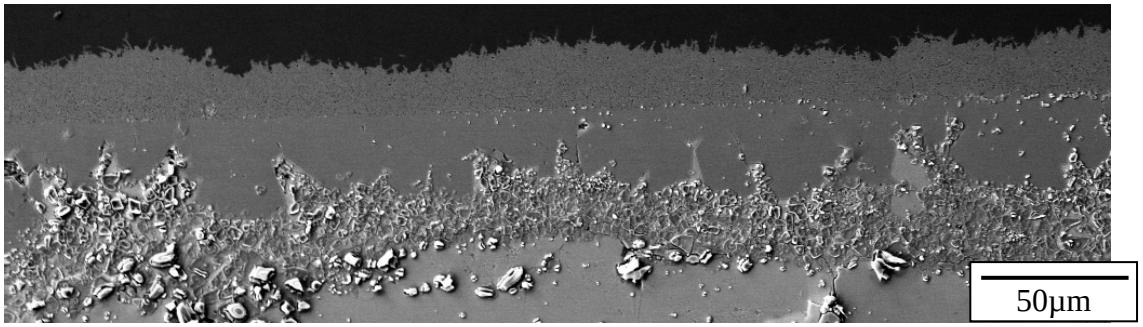

(a)

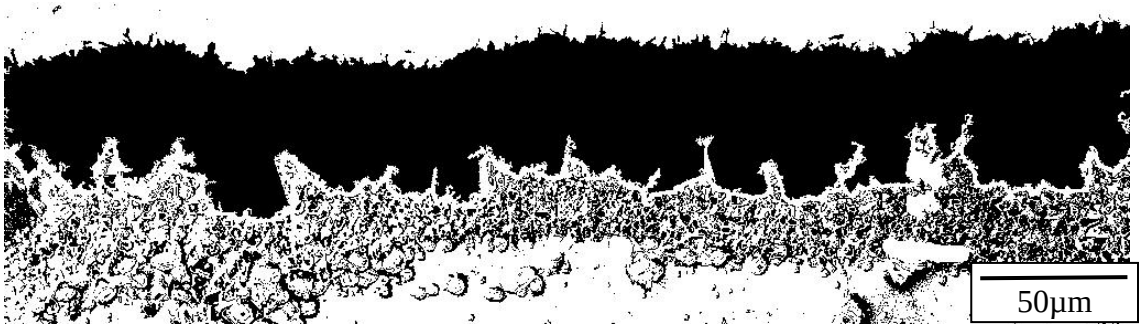

(b)

Figure 71. (a) SEM micrograph and (b) corresponding Image J threshold image selecting only the diffusion area (black). The average thickness of the diffusion zone was measured by dividing the selected area by the length of sample investigated. The lighter, irregular area below the diffusion zone is cerium oxide formed after polishing, and is not part of the diffusion.

Titanium Dioxide Coatings

The first TiO_2 diffusion couple test was performed at 560ºC for 100 hours with a 15µm thick as-deposited (unsintered) coating prepared using 15 nm anatase TiO_2. The coated side showed a slight decrease in diffusion length, reducing the average diffusion length from 79.8 µm to 29.3µm, which represents a factor of improvement of 2.7 (63.3% reduction). The diffusion was also more uniform on the coated side, which is desirable for this application. An SEM backscatter micrograph of the cross-section of the diffusion couple after the tests is shown in Figure 72.

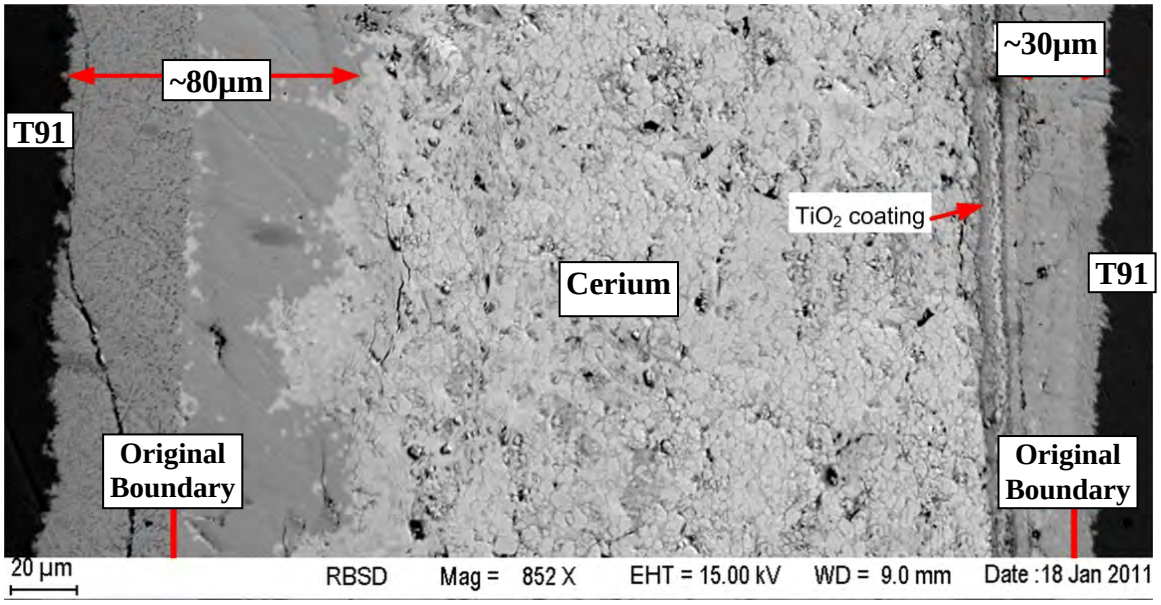

Figure 72. Backscatter micrograph of as-deposited TiO_2 diffusion couple. Uncoated side (left) shows approximately 80µm of diffusion whereas on the coated side (right) diffusion length was approximately 30µm.

Higher magnification images (Figure 73) show how the structure of the coating remained intact and diffusion was limited to cerium diffusion through the coating into the iron. Iron did not diffuse through the coating into cerium. Fe_2Ce was identified as the main intermetallic compound.

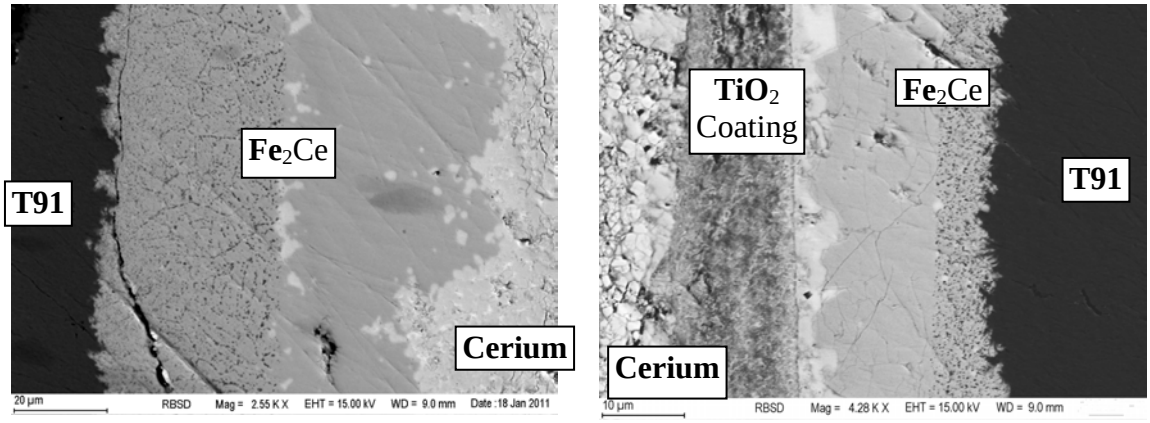

(a) (b)

Figure 73. High magnification backscatter micrographs of (a) uncoated and (b) as-deposited TiO_2 coated samples. The TiO_2 coating remained largely intact.

An EDS line scan analysis (Figure 74) of this sample highlights the effectiveness of titanium oxide as a diffusion barrier. The TiO_2 coating completely inhibited the diffusion of iron into cerium and significantly reduced the amount of cerium diffusion into steel. Figure 75 shows the diffusion couple cross section produced with sintered TiO_2 coating. As can be seen no diffusion occurred on the coated side while there is severe diffusion is observed on the of the uncoated side.

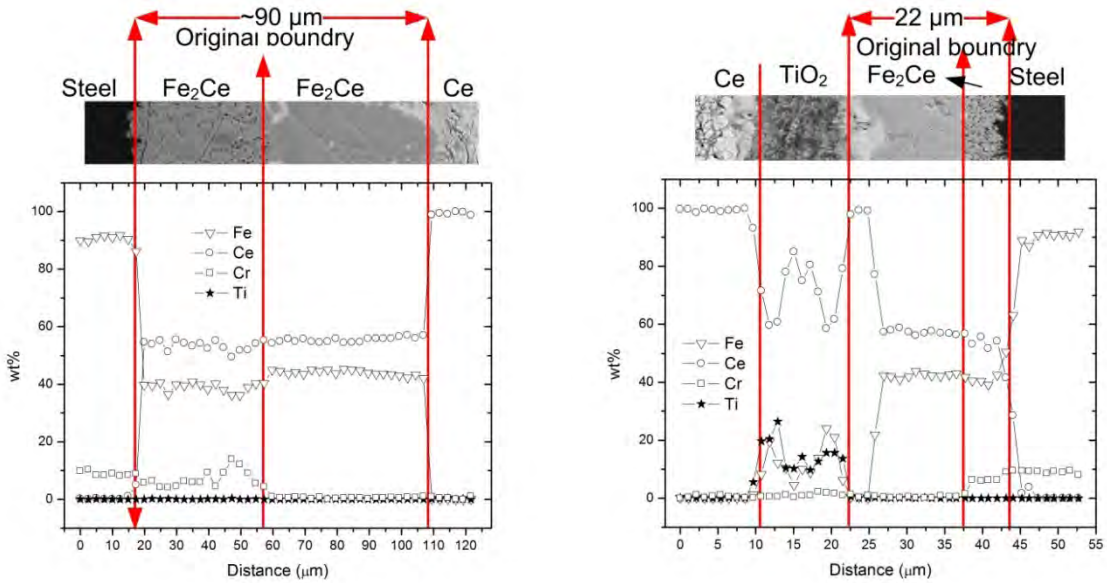

(a) **(b)**

Figure 74. EDS line scans across diffusion couples (a) uncoated and (b) as-deposited TiO_2 coated samples. The diffusion zone was reduced significantly by the TiO_2 coating.

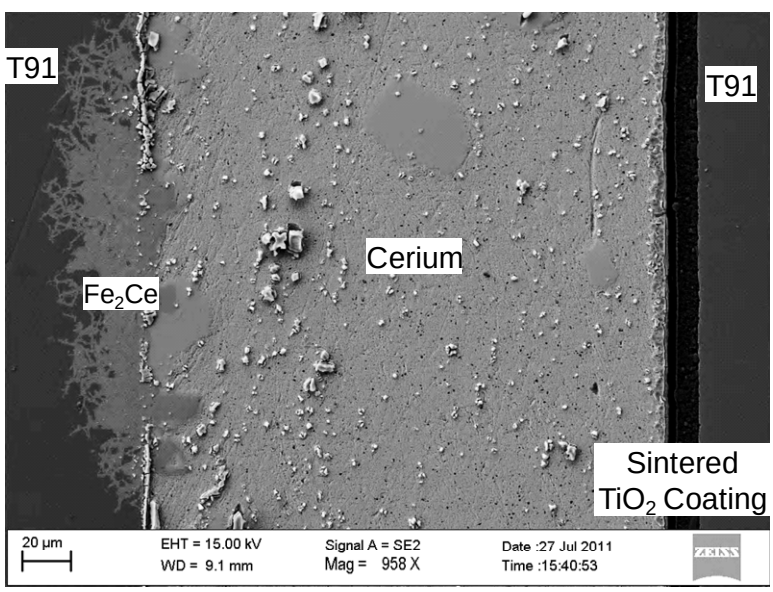

Figure 75. Backscatter micrograph of TiO_2 coated and sintered T91 (right) and uncoated T91 (left). No diffusion is observed on the coated side.

Figure 76 shows the cross-sectional analysis on the T91/cerium/ sintered TiO_2 coated T91 diffusion couple. As may be observed in the SEM BSE micrograph, severe interaction between

iron and cerium occurred on the bare side (left) where the Fe_2Ce intermetallic compound formed. The maximum width of the interaction zone is up to 60µm. The original boundary is distinguishable by a sudden drop of the chromium content (Figure 76e) in the line scan analysis. This suggests that diffusion and chemical interactions occur between iron and cerium. In contrast, significantly less interaction occurs with cerium on the coated side (right), which indicates the excellent diffusion barrier characteristic of the sintered TiO_2 coating. It was also worth pointing out that increasing the thickness of the TiO_2 coating from 4µm to 7.5µm and then to 10µm decreased the width interaction zone. For the 10µm coating reduced the FCCI by up to 80%.

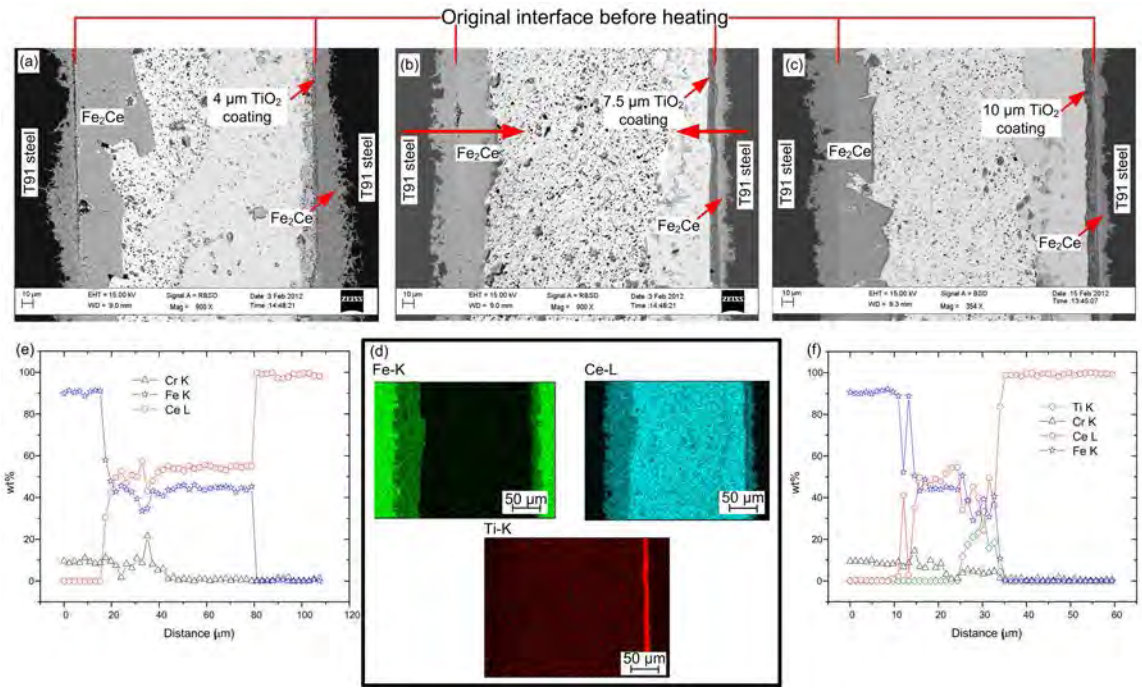

Figure 76. T91 steel/Cerium/sintered TiO_2 coated T91 steel diffusion couple cross sectional analysis, coating thickness is (a) 4µm (b) 7.5µm (d) 10µm SEM BSE micrograph: on the bare side (left) shows severe interaction between cerium and iron occurred while on the coated side (right) no interaction zone is seen. (d) EDS map and (e) and (f) EDS line scan analysis of the regions marked in (b). The diffusion couple experiment was conducted at 575ºC for 100 hours.

Yttria-Stabilized Zirconia Coatings

Diffusion couple experiments were performed with a 10µm YSZ coated sample at 585ºC for 40 hours. The coatings were deposited using nanofluid (0.5wt% 200-300nm YSZ in acetylacetone with 0.15 vol% TEA) followed by sintering at 1050ºC for 4 hours. The YSZ coating acted as an excellent diffusion barrier as shown in a backscatter micrograph (Figure 77), almost completely eliminating diffusion.

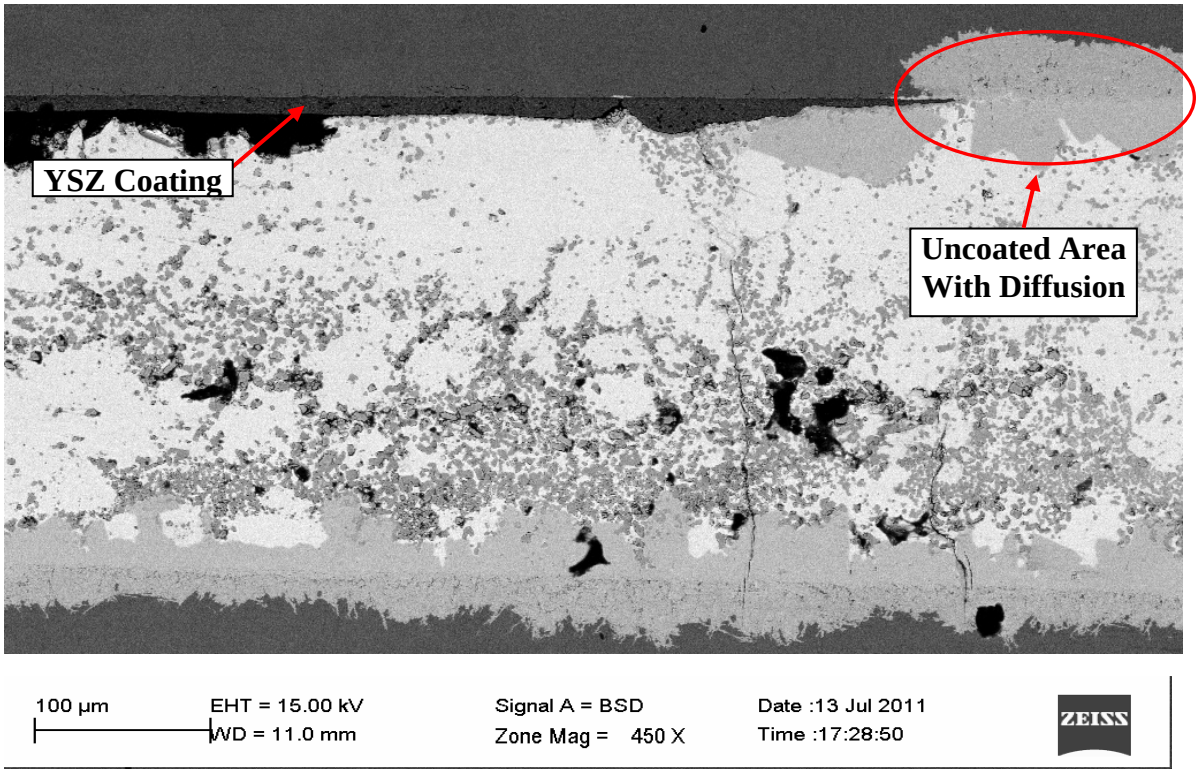

Figure 77. Backscatter SEM micrograph of YSZ coated T91 (top) also showing a small uncoated T91 region (bottom and right edge). No diffusion was observed where YSZ coating was present but significant diffusion (~60µm) was observed in regions where the coating was absent.

This image in Figure 77 demonstrates the excellent diffusion barrier characteristics of the YSZ coating. The diffusion length on the bare side averaged ~57 µm and there is no measurable diffusion in the YSZ coated side. This is also explicitly observed in the top right of Figure (circled) where the coating is missing and significant diffusion has occurred into the bare steel. To relate the diffusion characteristics of this coating to the others, a 1µm diffusion length was assumed on the coated side, providing a factor of improvement of 57 (98% reduction).

Energy dispersive x-ray analysis confirms the absence of diffusion in either direction on the YSZ coated side (Figure 78). The figure clearly indicates that iron did not diffuse through the coating into the cerium (Figure 78b), the retention of the coating structure (Figure 78c), and the absence of cerium diffusion into steel (Figure 78d).

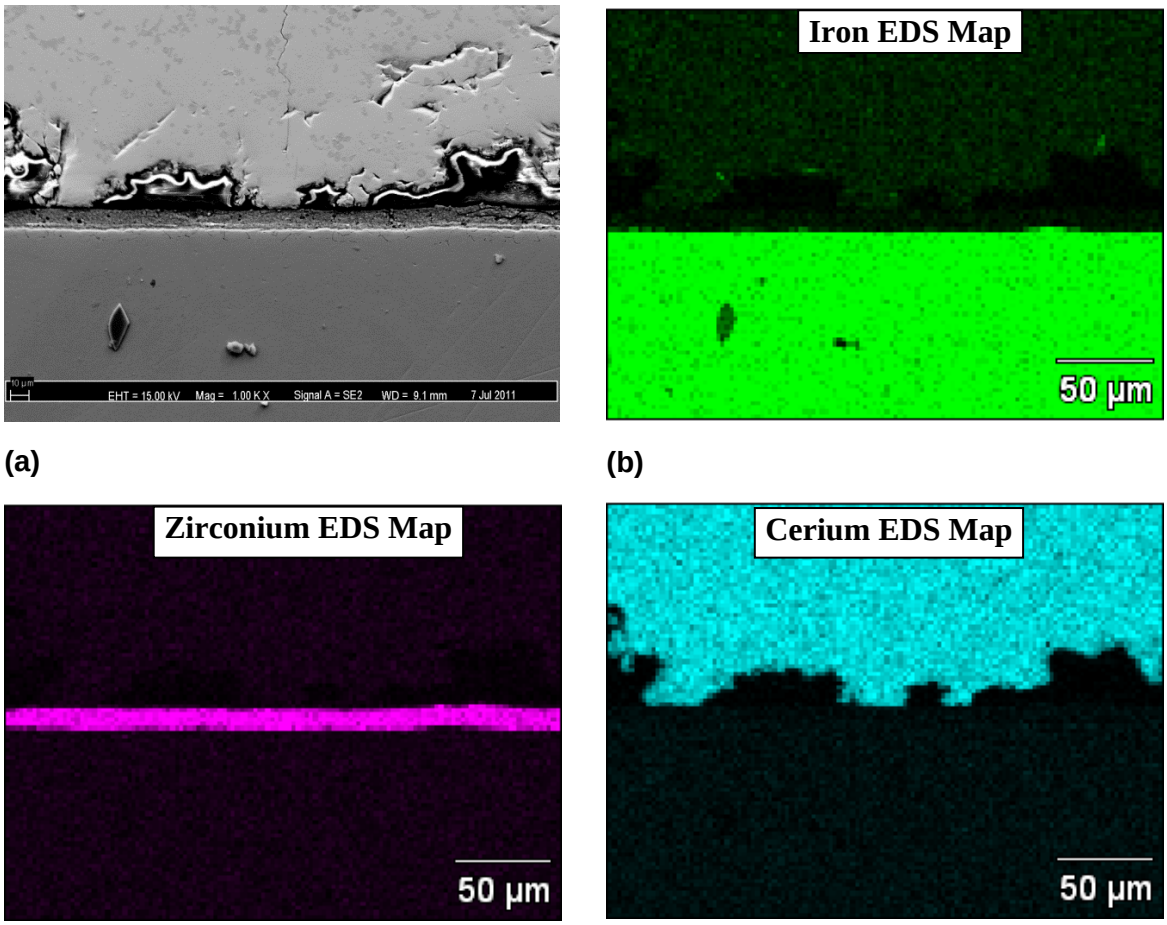

(a) **(b)**

(c) **(d)**

Figure 78. (a) SEM micrograph of YSZ coated side of diffusion couple and elemental EDS maps of (b) iron, (c) zirconium, and (d) cerium. The robust YSZ coating remained intact while preventing diffusion of iron into cerium and cerium into iron.

Figure 79 shows the cross sectional analysis on the T91/cerium/ sintered YSZ coated T91 diffusion couple performed at 575ºC for 100 hours. As may be seen in SEM BSE micrograph of Figure 79a, on the bare side (left) severe interaction between iron and cerium occurs and Fe_2Ce intermetallic compound is formed. The width of the interaction zone is up to 63µm. The original boundary is distinguishable by a sudden drop of the chromium content (Figure 79e) in the line scan analysis. This indicates that the main diffusion and interaction occurs between iron and cerium. On the coated side (right) significantly less interaction between cerium and iron is observed, which indicates the excellent diffusion barrier characteristics of the sintered YSZ coating. By increasing the thickness of the YSZ coating from 3.5µm to 6.5µm the interaction zone becomes smaller (Figure 79b) while it vanishes completely in the coating with 8µm thickness (Figure 79c).

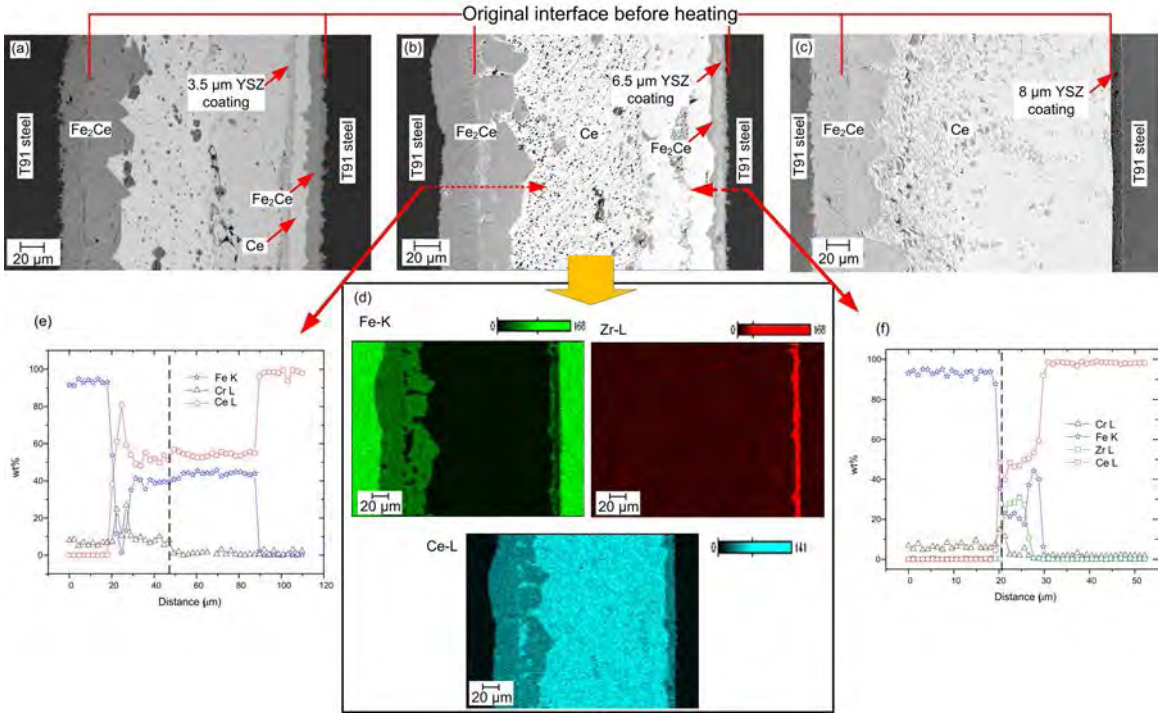

Figure 79. T91 steel/Cerium/sintered YSZ coated T91 steel diffusion couple cross sectional analysis for coating thicknesses (a) 3.5µm (b) 6.5µm (d) 9µm SEM BSE micrograph: on the bare side (left) severe interaction between cerium and iron occurred while on the coated side (right) no interaction zone is seen. (d) EDS map and (e) and (f) EDS line scan analysis of the regions marked in (b). The diffusion couple test was conducted at 575ºC for 100 hours.

Vanadium Oxide Coatings

Diffusion couple tests with vanadium oxide coatings were performed at 585ºC for 40 hours. The sample with 10 µm thick coating was sintered at 1050ºC for 4 hours to promote densification and substrate adhesion. The V_2O_3 coated sample reduced the diffusion path from 104 µm to 11 µm, a factor of improvement of 9.5 (89% reduction). A backscatter micrograph displays the diffusion characteristics well (Figure 80).

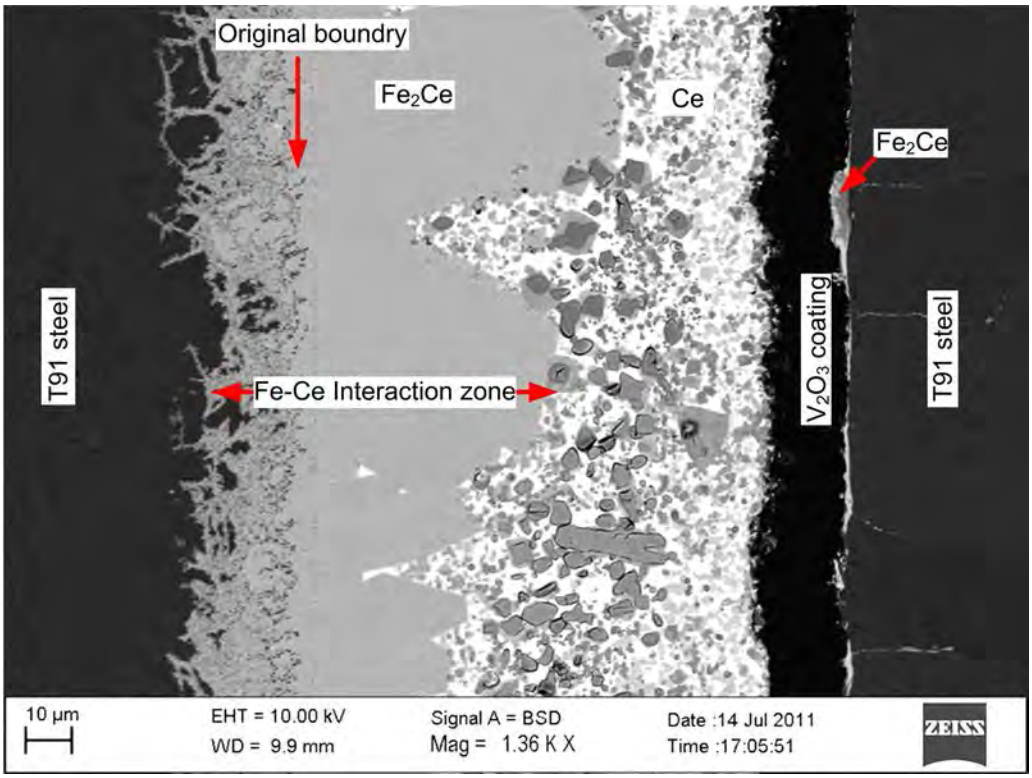

Figure 80. Backscatter micrograph of V_2O_3 diffusion couple. The vanadium oxide coating (right) reduced the diffusion path almost 100µm on the uncoated side (left) to less than 10µm.

Energy dispersive spectroscopy was utilized to confirm the location of the coating, cerium, and iron. Figure 81 shows a backscatter image (a) with corresponding elemental maps of (b) vanadium, (c) iron, and (d) cerium. The V_2O_3 coating inhibited the diffusion of iron into cerium and greatly reduced the diffusion of cerium into steel.

Though there were signs of increased densification upon sintering, adhesion remained poor in V_2O_3 coatings. Vanadium oxide is a very good diffusion barrier, greatly reduces the inter-diffusion between iron and cerium. The total diffusion length was reduced by nearly a factor of 9.5 (89% reduction).

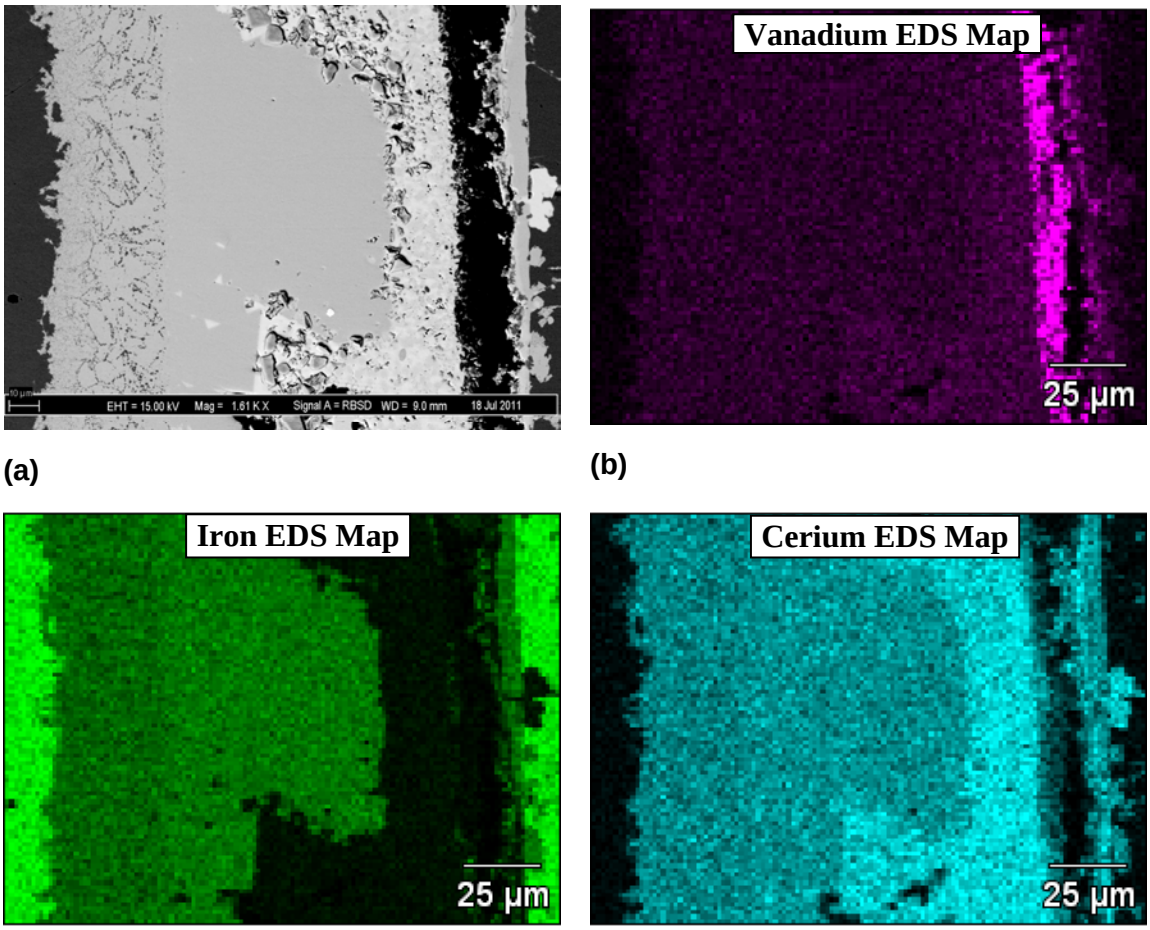

(a) **(b)**

(c) **(d)**

Figure 81. (a) SEM micrograph of V_2O_3 diffusion couple along with elemental EDS maps of (b) vanadium, (c) iron, and (d) cerium. The diffusion on the uncoated (left) is much greater than that on the vanadium oxide coated side (right).

Titanium Coatings

Figure 82 shows the cross sectional analysis on the T91/cerium/ sintered titanium coated T91 diffusion couple. As can be seen in the SEM BSE micrograph on the bare side (left) severe interaction between iron and cerium occurs and Fe_2Ce is formed. The width of the interaction zone is up to 63µm. The original boundary is distinguishable by a sudden drop of the chromium content (Figure 83 c) in the line scan analysis. This indicates that the main diffusion and interaction occurs between iron and cerium. Although on the coated side (right) no evidence of interaction between cerium and iron is seen, which indicates the excellent diffusion barrier characteristic of the sintered titanium coating. The chemical composition profile transition is very sharp across the cerium/coating/steel boundary. Coating region is composed of >90wt% titanium indicating the negligible dissolution of cerium into the coating.

To evaluate the effect of sintering on the diffusion barrier characteristic of the coating, the same experiment was conducted but this time using the deposited coating. Figure 83 shows the SEM BSE micrograph of the cross section of the diffusion couple. As can be observed, the

interaction zone formed on both sides and it is slightly smaller on the coated side (56 µm vs 66 µm). Cerium was able to diffuse through the porous titanium coating where it encountered the T91 steel surface and reacted with it. After reaction Fe_2Ce intermetallic formed and the titanium coating was pushed away from the original interface of steel/coating.

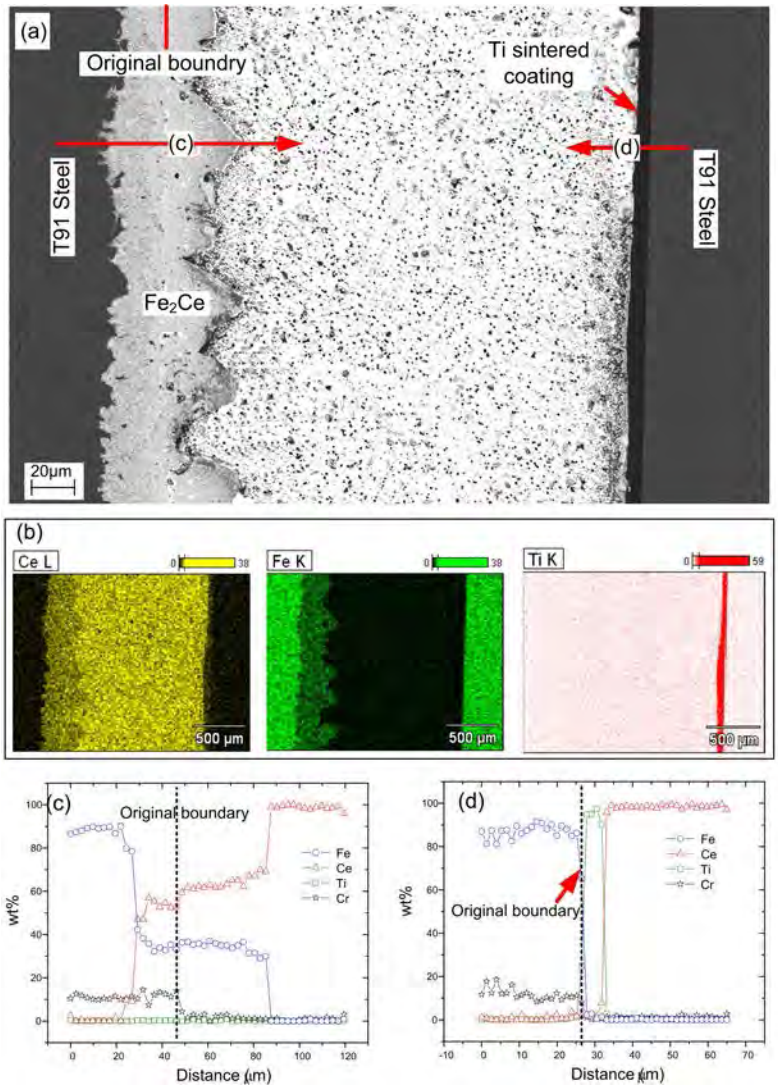

Figure 82. T91 steel/Cerium/Sintered titanium coated T91 steel diffusion couple cross sectional analysis, (a) SEM BSE micrograph: on the bare side (left) severe interaction between cerium and iron occured while on the coated side (right) no interaction zone is seen (b) EDS map of the micrograph shown in (a); (c) and (d) EDS lines scan of the marked lines in (a).

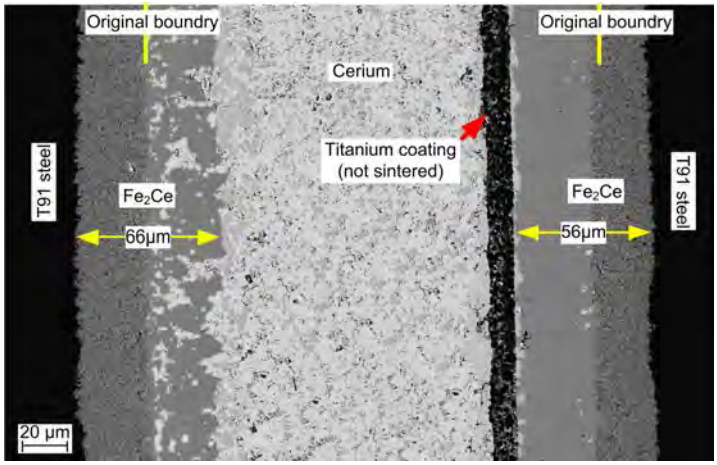

Figure 83. SEM BSE micrograph of cross section of T91 steel/cerium/as deposited Titanium coated T91 steel diffusion couple. The interaction zone is slightly larger on the bare side (left) compared to the coated side (right).

One titanium diffusion couple test was performed with an as-deposited 15µm thick coating at 560ºC for 100 hours. The diffusion path was reduced from 76µm to 65µm as seen in Figure 84. This corresponds to only a 5% reduction in diffusion length. A backscatter diffraction micrograph of the as-deposited TiO_2 coated sample is shown in Figure 84. The titanium coating on the right side only slightly inhibited diffusion. ImageJ analysis shows a decrease in average diffusion length from 76µm to 65µm.

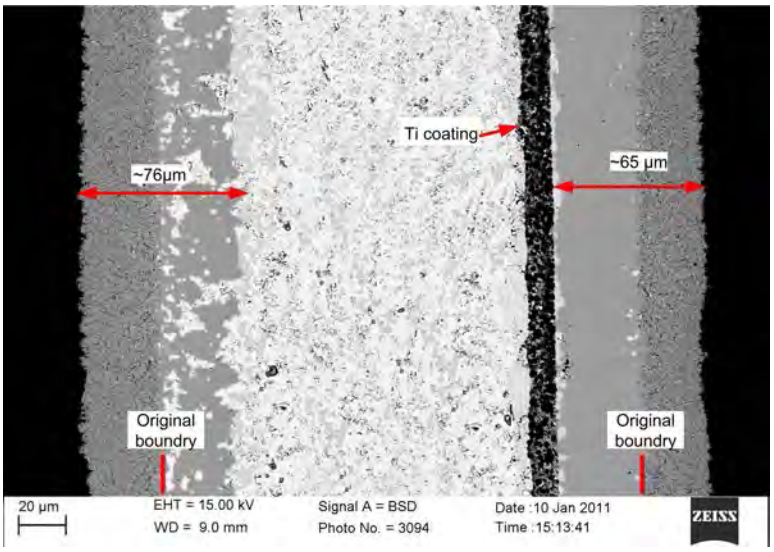

Figure 84. Backscatter image of as-deposited titanium diffusion couple. The as-deposited titanium coated side (right) only slightly reduced diffusion.

Zirconium Coatings

One zirconium diffusion couple experiment was conducted at 585ºC for 40 hours. Due to the ease of oxidation of zirconium, a sintering step was unfeasible for these coatings. The coating was 15µm thick and exhibited poor adhesion. The diffusion characteristics of zirconium were

poor; the coating detached from the substrate and pieces of it drifted into the cerium medium. There was no measurable decrease in diffusion length with the zirconium coating.

Figure 85 shows a backscatter micrograph of the zirconium diffusion couple. The coating was originally attached to the top T91 steel, but detached during the diffusion couple tests. This can be attributed to the large, loosely adherent particles comprising the coating. The hot, ductile cerium (207MPa, Vickers hardness) is thought to mold around the large, hard (903MPa) zirconium particles and contacted the steel surface. As the coating is not well-adhered to the surface, formation of Fe_2Ce separates the coating and allows each individual particle to diffuse into the cerium medium. Point elemental analysis confirms that the zirconium rich cerium is not a Ce-Zr compound, rather portions of zirconium surrounded by cerium. In some of these areas it was 81 wt% zirconium, 18 wt% cerium, while in others it was 14 wt% zirconium and 84 wt% cerium.

Elemental analysis in another location on the sample shows these same effects (Figure 86(a-d)). Figure 86(b), the zirconium map, shows how the zirconium particles have detached and diffused into the cerium medium, particularly on the left side of this image. Figure 86(c), the iron map, shows there is no measurable difference in the iron diffusion and Figure 86(d) shows that cerium also diffused similarly on either side of the sample.

If the deposit were comprised of smaller particles, the diffusion path may be much different. Smaller particles may adhere better to each other and the steel surface. While coatings comprised of larger particles have connected porosity, smaller particles would greatly reduce the connected porosity and prevent or delay contact with the underlying steel. In addition, smaller particles may also exhibit higher density. Sintering may also be an option to increase adhesion and density, but it must be performed in a furnace with a very low oxygen partial pressure.

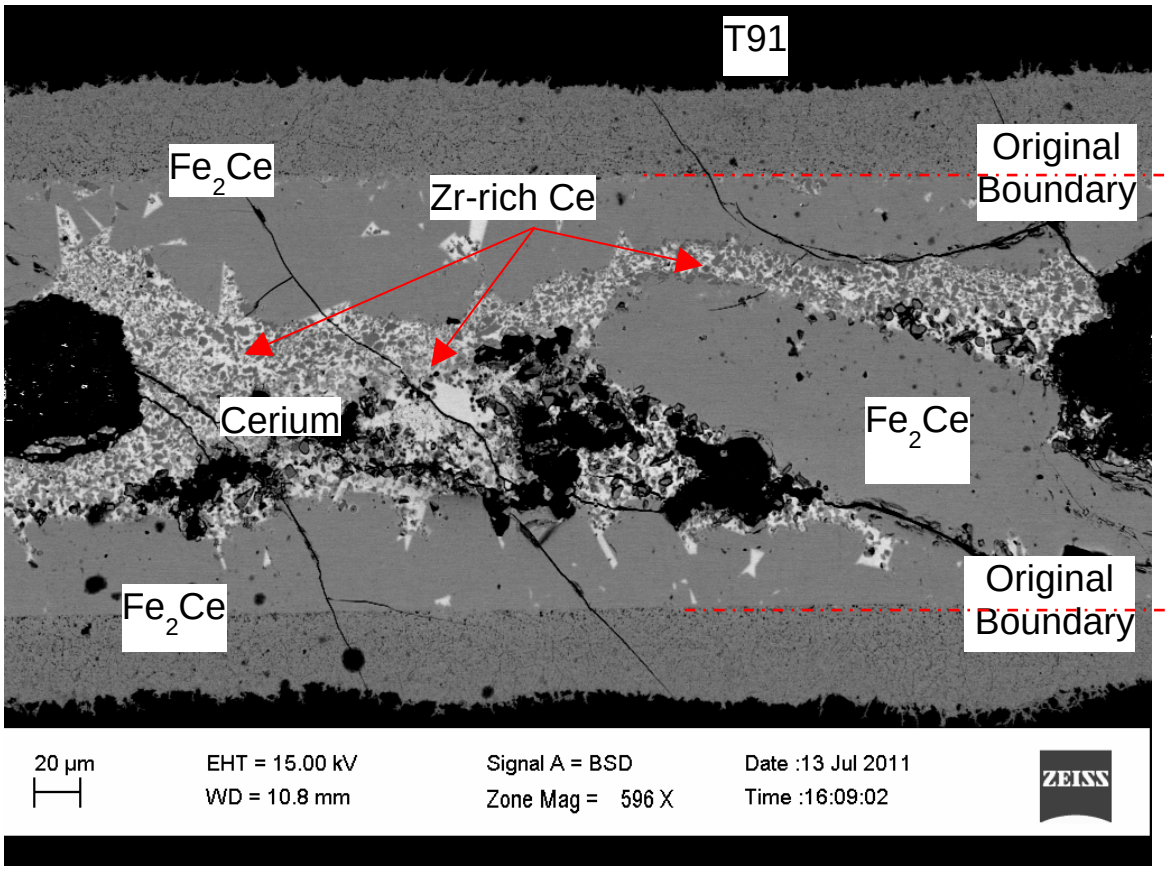

Figure 85. Backscatter SEM micrograph of a zirconium diffusion couple. The large particles comprising the coating detached from the substrate and migrated into the cerium. There was no difference in diffusion length between the coated sample (top) and uncoated sample (bottom).

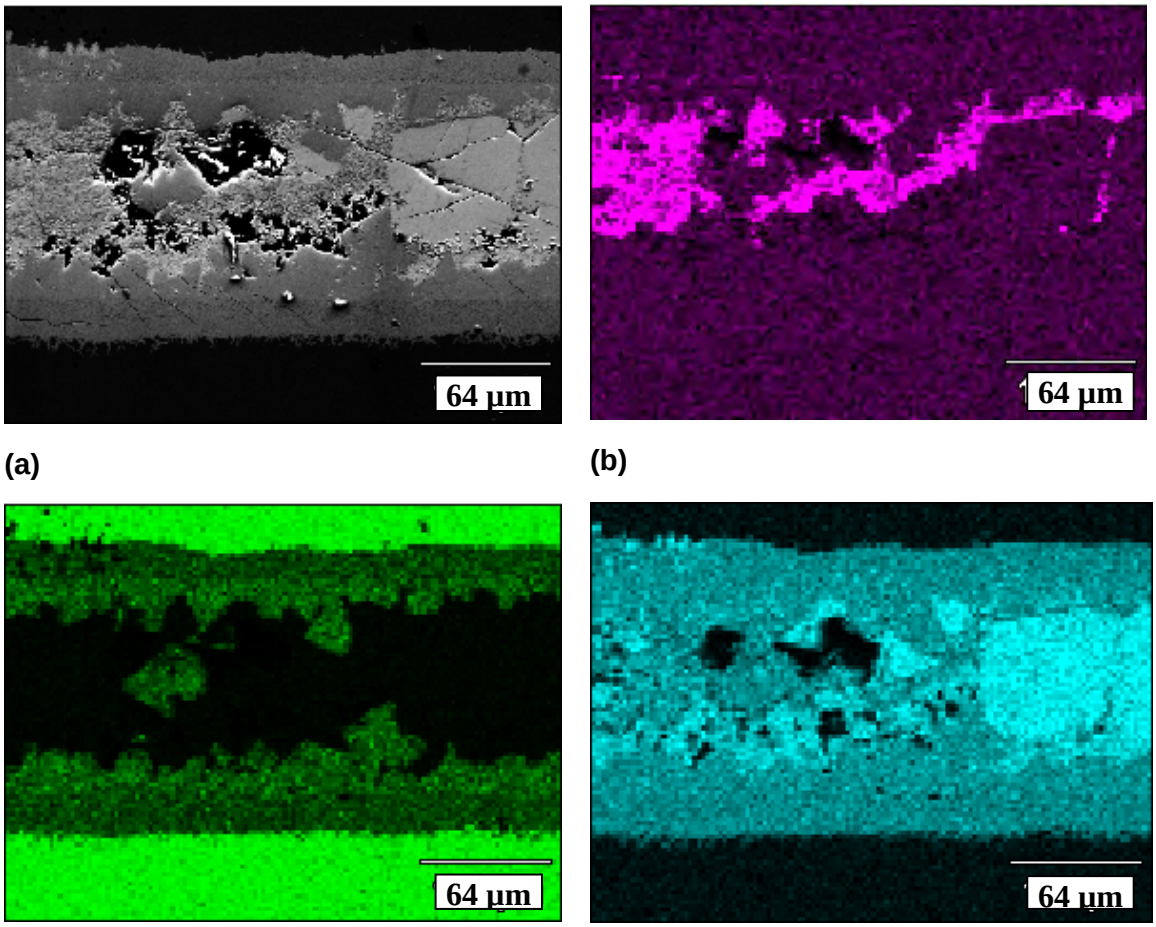

(a) (b)

(c) (d)

Figure 86. (a) SEM micrograph of as-deposited zirconium diffusion couple along with elemental EDS maps of (b) zirconium, (c) iron, and (d) cerium. The EDS maps show clearly that the zirconium coating did not remain intact or prevent diffusion.

In conclusion zirconium deposits do not provide adequate diffusion barrier properties. Nanoparticles of zirconium could provide dense and uniform coatings and may have provided for improved diffusion barrier characteristics; this area warrants further study.

Vanadium Diffusion Coatings

Two vanadium diffusion couple test were performed: one with an as-deposited 10µm vanadium coating and one with a 5µm vanadium coating that was sintered at 850ºC for 4 hours. The as-deposited coating acted as a poor diffusion barrier, with the cerium presumably seeping around the large vanadium particles and contacting the steel. The sintered sample performed much better and reduced the average diffusion length from 43.7µm to 7.4µm, an improvement factor of 5.9 (83% reduction).

Figure 87 shows a backscatter image of the as-deposited 10 µm thick vanadium coating. The diffusion length is approximately the same on either side, and it can be seen that the vanadium coating is missing in many areas. Where the vanadium is present, cerium seems to have morphed around the particles and contacted the steel substrate.

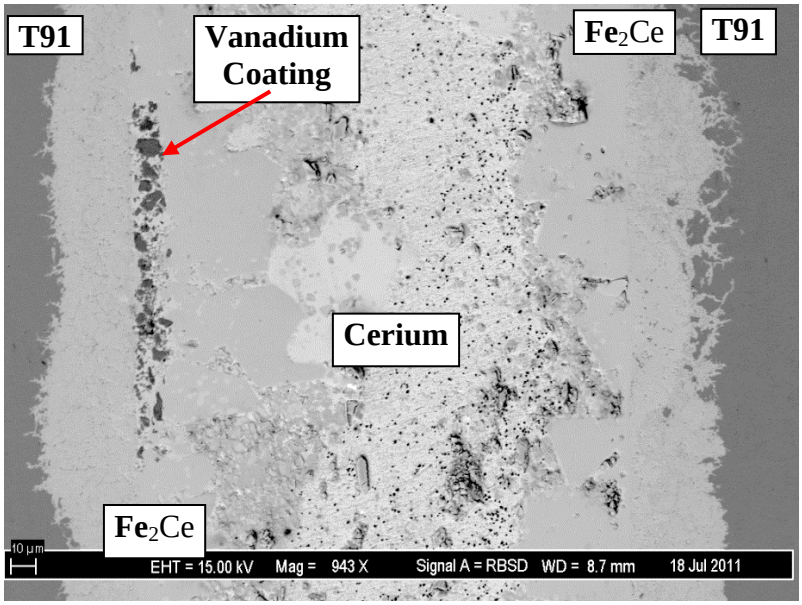

Figure 87. (a) SEM micrograph of as-deposited vanadium diffusion couple and elemental EDS maps of (b) vanadium, (c) iron, and (d) cerium. The vanadium coating did not remain intact or prevent diffusion.

The diffusion couple with sintered vanadium sample performed much better, even with the coating being only 5µm in thickness. Figure 88 shows a backscatter SEM micrograph that the vanadium coated side inhibited diffusion whereas bare T91 on the right experienced a significantly larger diffusion length. This image was analyzed by ImageJ processing and the average diffusion length was reduced from 43.7µm to 7.4µm, a factor of 6 improvement (83% decrease).

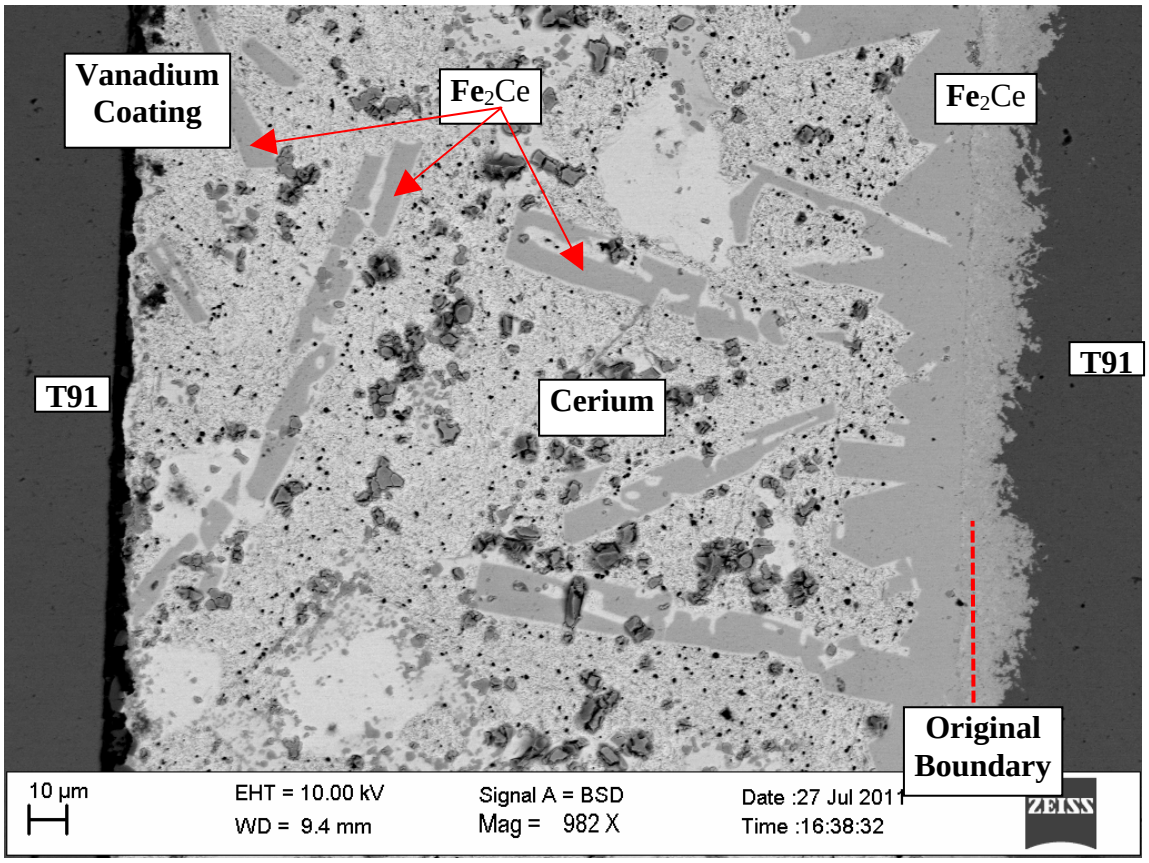

Figure 88. Backscatter micrograph of sintered vanadium diffusion couple. The sintered vanadium coating (left) only experienced a few microns of diffusion whereas the uncoated side (right) experienced tens on microns of diffusion.

Another backscatter image with corresponding elemental maps (Figure 89 a-d) confirms the location of vanadium, iron and cerium in the diffusion couple. Figure 89(b), the vanadium map, shows a slightly higher signal near the left interface, indicating the vanadium coating. Resolving the vanadium-cerium interface is very difficult as vanadium and cerium share an x-ray peak at 4.952keV and 4.839keV, respectively. Figure 89 (c) and (d) show the iron and cerium elemental maps, respectively.

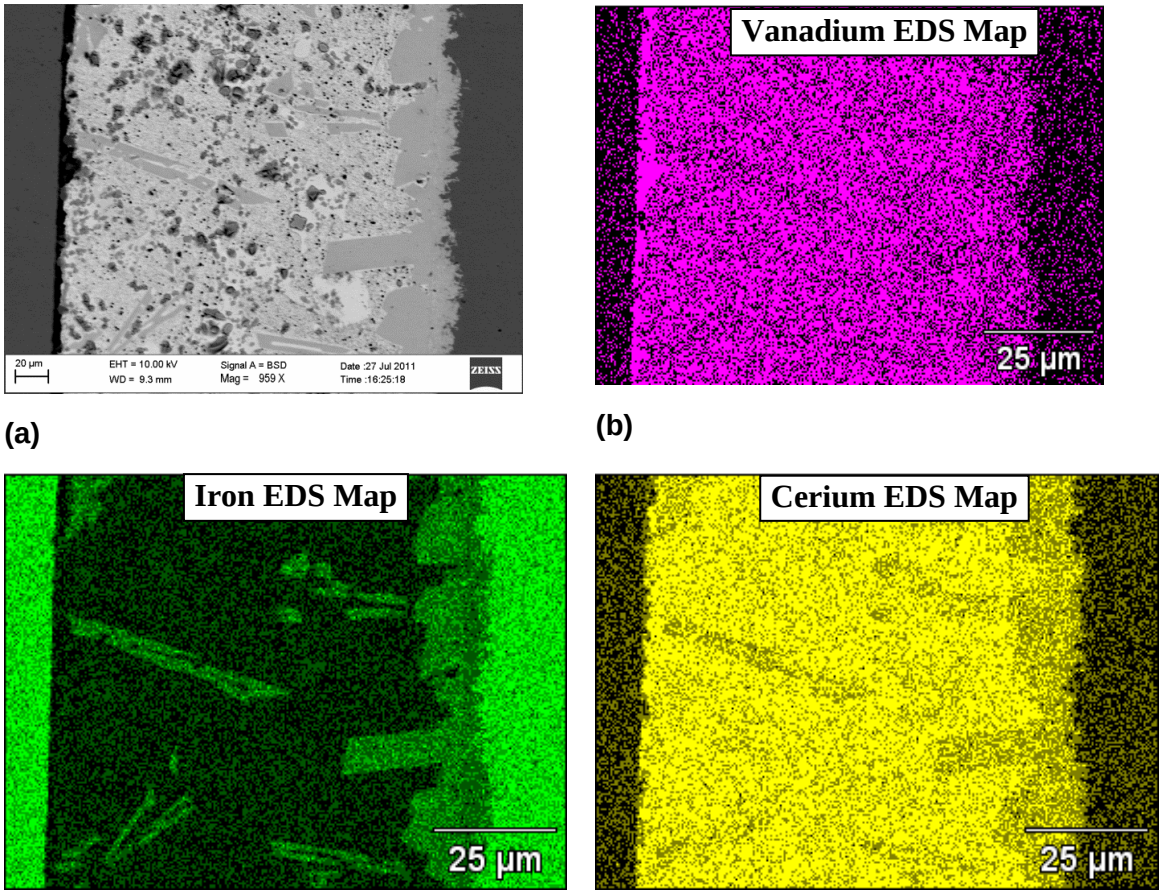

(a) **(b)**

(c) **(d)**

Figure 89. (a) SEM micrograph of sintered vanadium diffusion couple along with elemental EDS maps of (b) vanadium, (c) iron, and (d) cerium. The iron (c) and cerium (d) maps clearly indicate that the sintered vanadium coating significantly inhibits diffusion.

As-deposited vanadium acts as a poor diffusion barrier due to the large particles, connected porosity, and poor adhesion. Without sintering, the vanadium coating did not measurably inhibit diffusion. These issues were resolved with a 4 hour sintering step at 850ºC. The sintering step greatly reduced connected porosity and increased adhesion. The result was a coating that reduces diffusion from 43.7 µm to 7.4 µm, a decrease of 83%. These studies were conducted with coatings deposited using coarse vanadium particles. Deposition of coatings using nanoparticles of vanadium has considerable potential and warrants further study.

VII.E.Thermal Models

Basic Approach

An important consideration in the development of coatings for claddings is any increases in fuel center-line temperature as a result of the addition of the coating. The coating thicknesses used in this study and being proposed for the FCCI mitigation are too small to increase the fuel centerline temperature to an appreciable degree. However, this must be supported by heat transfer modeling by taking into account the thickness, thermal conductivity, density, and

composition of the coatings. Two models were applied for this purpose. One model mimics the initial configuration where the U-Zr fuel has not undergone significant swelling and sodium exists in the cladding gap (Figure . The second model assumes the fuel has swelled enough to displace the sodium and has come into direct contact with the cladding (Figure 90 and 91). The two also models are also illustrated in Figure 92. The swelled fuel model takes a conservative approach, assuming all the sodium in the gap has been displaced by the swelling fuel and is relocated in the plenum. In reality, some of the sodium will fill the pores in the coating, resulting in higher conductivity and lower fuel centerline temperature.

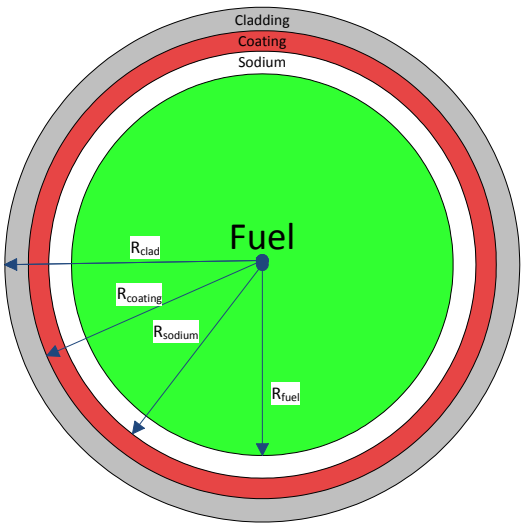

Figure 90. Initial Configuration Model: here sodium fills the gap between the fuel and coated cladding.

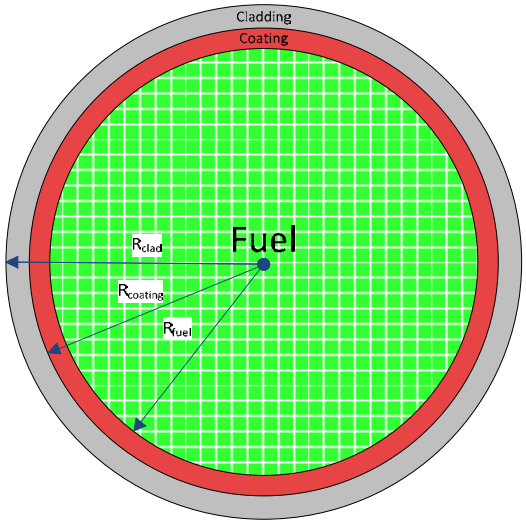

Figure 91. Swelled Fuel Model: here the fuel has swelled, displaced the sodium from the gap, and contacted the cladding.

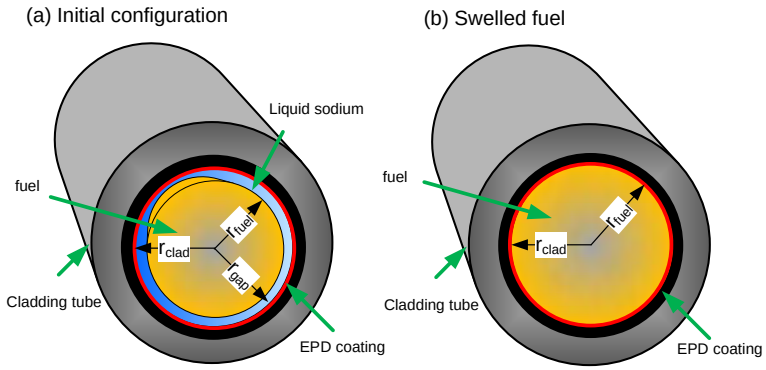

Figure 92. Schematic of configuration of the inside of fuel cladding in SFR (a) initial configuration model wher sodium fills the gap between the fuel and coated cladding and (b) swelled fuel model where the fuel has swelled, displaced the sodium from the gap, and contacted the cladding.

Initial Configuration Model

In the SFR cladding design metal fuel pins are filled with sodium to provide the thermal bond between the fuel and the cladding. Moreover, sodium is a liquid at reactor core operating temperatures and is chemically compatible with metallic fuels. Since liquid sodium has a much higher thermal conductivity than inert gas, this helps to lower the operating temperature of the metal fuel. For cylindrical configurations with concentric materials, the fuel centerline temperature is governed by equation (10) [49]. The variables are defined in Table 5 and they were obtained from various resources [50-52]. The thermal conductivity is a function of the porosity as described by equation (11) where ρ is the fractional theoretical density, K_s is the thermal conductivity of a 100% dense material, and K is the density adjusted thermal conductivity of each material (coating, fuel, etc.). According to [49], most fuel is fabricated to 75% smear density, but the fuel element itself is almost 100% dense.

$$T_{fuel} - T_{clad} = q'[\frac{\ln(\frac{r_{clad}}{r_{coating}})}{2\pi k_{clad}}] + q'[\frac{\ln(\frac{r_{coating}}{r_{gap}})}{2\pi k_{coating}}] + q'[\frac{\ln(\frac{r_{gap}}{r_{fuel}})}{2\pi k_{gap}}] + q'[\frac{1}{4\pi k_{fuel}}] \qquad \text{equation 10}$$

$$k = k_s(1-(1-\rho)^{2/3}) \qquad \text{equation 11}$$

Table 5. SFR assembly design parameters and thermophysical properties

T_{clad}	823 K (550ºC) [34-36]	r_{gap}	0.696 cm [38]
q'	40000 W/m [36]	k_{gap}	62.9 W/m.K [37]
r_{clad}	0.755 cm [38]	k_{clad}	26 W/m.K [38]
r_{fuel}	0.577 cm [38]	K_{TiO2}	11.7 W/m.K [40]

Swelled Fuel Model

Upon irradiation fuel begins to swell, closing the gap between the fuel and the cladding. This reduces the temperature difference between the inner and outer surfaces of the cladding. To accommodate for the swelling in the fuel, equation (8) is modified by omitting the term related to the liquid sodium inside the gap. The same values in literature were used as in the initial configuration model. The governed equation is presented in equation (12).

$$T_{fuel} - T_{clad} = q'[\frac{\ln(\frac{r_{clad}}{r_{coating}})}{2\pi k_{clad}}] + q'[\frac{\ln(\frac{r_{coating}}{r_{fuel}})}{2\pi k_{coating}}] + q'[\frac{1}{4\pi k_{fuel}}] \qquad \text{equation 12}$$

Several assumptions were made in the second model. As burn-up increases and the fuel swells, it displaces the sodium and comes into direct contact with the coating and cladding. The

displacement of coolant and higher amount of porosity of the fuel decrease the effective thermal conductivity of the system. It was also assumed that the coating is not compressed by the swelling fuel and therefore retains its original thickness and density. Any compression or densification of the coating will result in higher thermal conductivity and thus lower the calculated centerline temperature. The swelled fuel calculation also takes a very conservative approach, assuming all the sodium in the gap has been displaced by the swelling fuel and is redistributed in the plenum. In reality, the sodium can potentially fill the pores, resulting in higher conductivity and lower fuel centerline temperature.

Results of Modeling

Based on the above theory, increase in fuel centerline temperatures have been calculated for TiO_2 coatings and YSZ in Figures 93 and 94, respectively. As may be noted, neither coating increases the fuel center-line temperature to any extent. The fuel center-line temperature is higher for YSZ than TiO_2, owing to its lower thermal conductivity. Table 6 shows the physical parameters for various materials. The fuel centerline temperature is below 815ºC for all coatings, as shown in Figure 95 and 96 constructed using equations 13 and 14 for various coating materials. These temperatures are all well below the fuel melting temperature of approximately 1100ºC. It can be concluded that the coating will have a negligible effect as long as the coatings are kept relatively thin i.e. ~5 µm for oxide coatings and ~25 µm for metallic coatings.

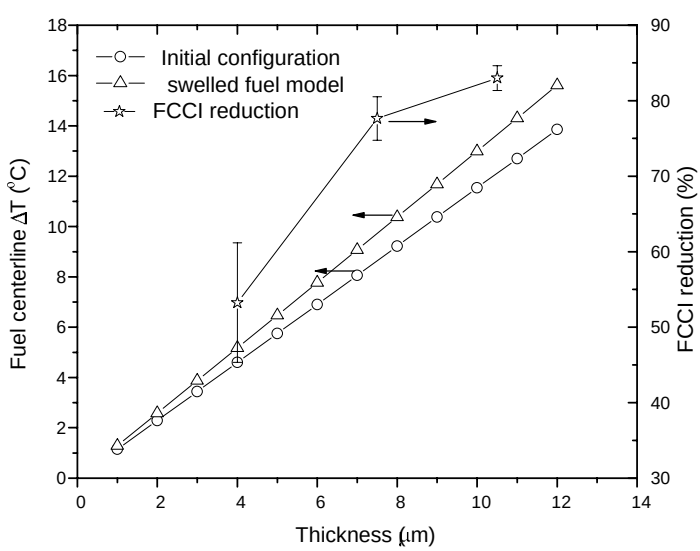

Figure 93. Temperature increase at the center of the fuel due to addition of coating (left axes) and reduction in the FCCI by addition of coating (right axes) for TiO_2 coating.

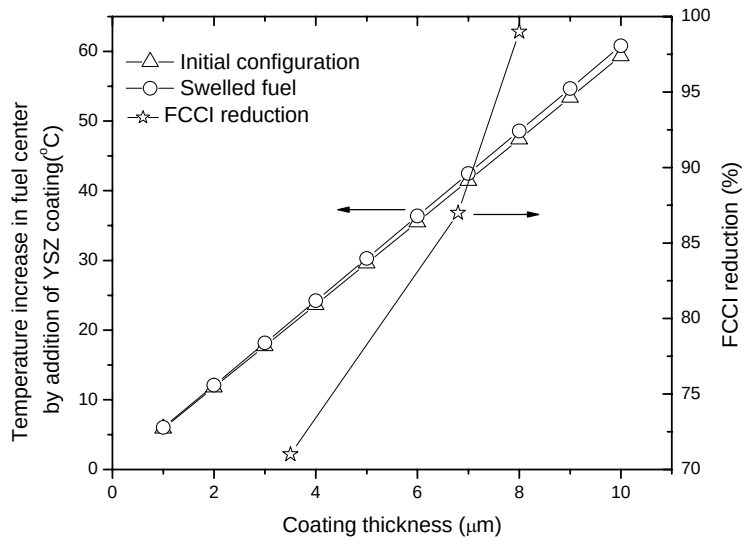

Figure 94. Temperature increase at the center of the fuel due to addition of coating (left axes) and reduction in the FCCI by addition of coating (right axes) for YSZ coating.

Table 6. Geometric values of experimental reactor and heat transfer properties [52].

Symbol	Value
T_{clad}	823 K
q'	44000 W/m
r_{fuel}	0.603 cm
r_{gap}	0.696 cm
r_{clad}	0.800 cm
k_{fuel}	28 W/m*K
k_{gap}	62.9 W/m*K
k_{clad}	26 W/m*K
k_{Ti}	21.9 W/m*K
k_{V}	30.7 W/m*K
k_{Zr}	22.6 W/m*K
k_{TiO2}	11.7 W/m*K
k_{V2O3}	5 W/m*K
k_{Zr02}	2 W/m*K

$$T_{fuel} = T_{clad} + q'\left[\frac{\ln\left(r_{clad}/r_{coating}\right)}{2\pi k_{clad}}\right] + q'\left[\frac{\ln\left(r_{coating}/r_{gap}\right)}{2\pi k_{coating}}\right] + q'\left[\frac{\ln\left(r_{gap}/r_{fuel}\right)}{2\pi k_{gap}}\right] + q'\left[\frac{1}{4\pi k_{fuel}}\right]$$

Equation (13)

$$k = k_s\left(1 - (1 - \rho)^{8/3}\right)$$ **Equation (14)**

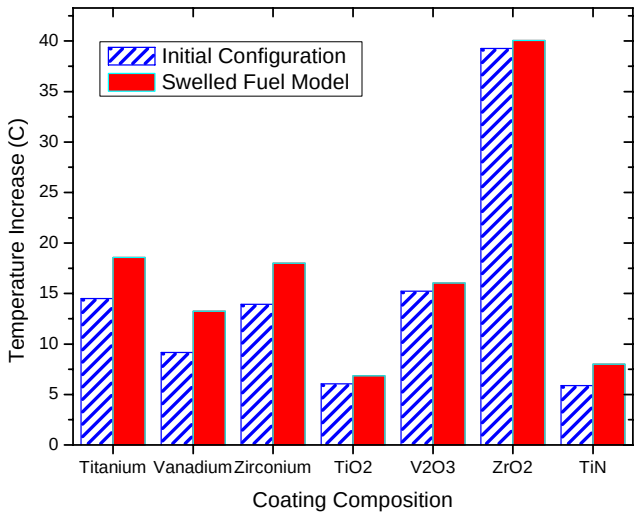

Figure 95. Increase in temperature due to FCCI barrier coating. The temperature increase is a modest 20ºC for most coatings and approximately 40ºC for zirconium oxide. Thickness is 25µm for metallic coatings and 5µm for oxide coatings.

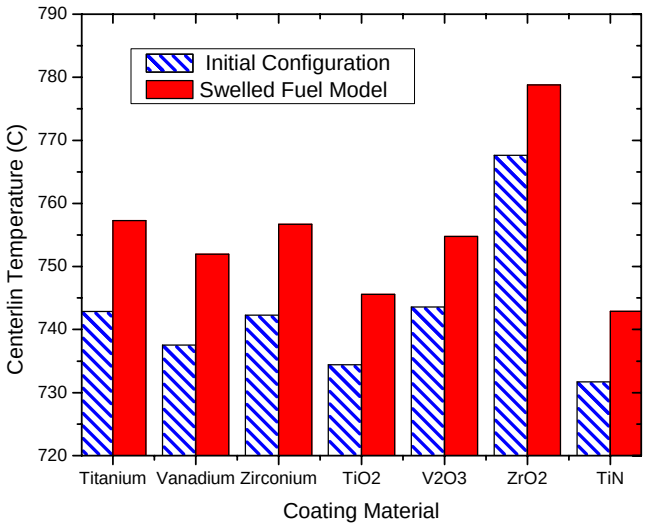

Figure 96. Maximum fuel centerline temperature. The maximum temperature is well below the fuel melting point of 1136ºC in all cases.

XII. Nanofluid Boiling Experiments to Prepare Coatings

While the project focused on the electrophoretic deposition for coatings, limited experiments were also conducted for depositing coatings by subjecting bare T91 ferritic steel samples to boiling nanofluids to deposit coatings. The nanofluid in this study consisted of a suspension of nanoparticles in deionized water. A fixture with a heater was designed that allowed for heating the sample to a desired temperature (Figure 97). Samples heated to various temperatures were immersed in nanofluids and coating mass deposited and microstructure were monitored as a function of power setting of the heater. Because water suspensions are generally unstable, a sonicator was used to create a homogeneous suspension just before each experiment.

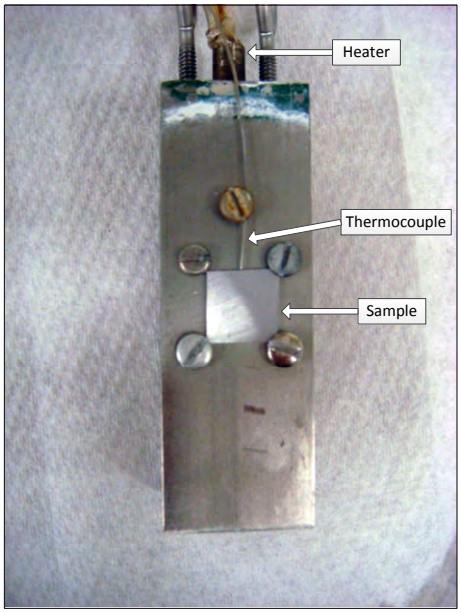

Figure 97. Fixture used for nanofluid boiling depositions.

The coatings showed deposited generally showed a fragile columnar morphology. SEM imaging of samples coated with this method indicated that a cluster of nanoparticles grew upwards from the sample substrate. Figure 98 shows a typical coating deposited using 10-30nm sized TiO_2 nanoparticles. Depending on process parameters, this cluster was relatively sparse or moderately dense.

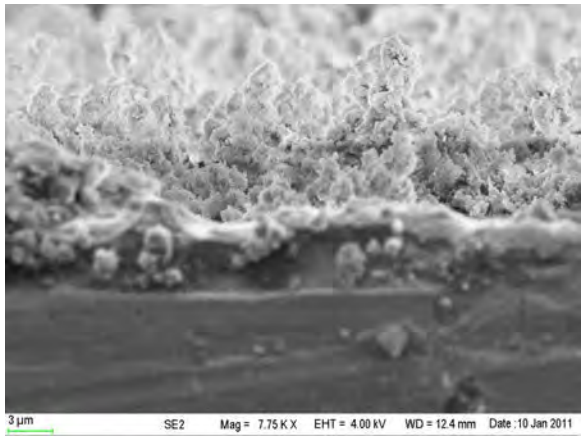

Figure 98. SEM micrograph of a coating produced by the boiling nanofluid method. Coating deposition results in the growth of clusters of nanoparticle columns.

Figure 99 shows coating deposition (expressed as mass change of the sample) as a function of heating power and TiO_2 concentration. Both heating power and concentration increase the coating deposition thickness.

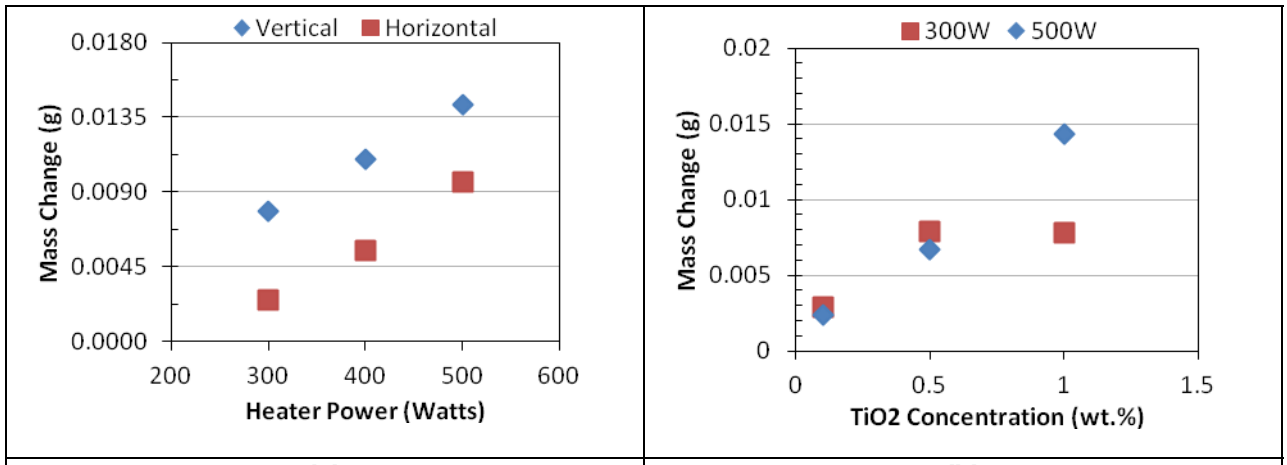

(a) **(b)**

Figure 99. Coating deposition as a function of heating power and TiO_2 concentration. 15 nm nanoparticles of anatase TiO_2 was used to prepare the nanofluid.

Coating morphology was dependent on the processing geometry. The best consistent results were observed with decreasing power and increasing nanofluid concentration. Figure 100 and 101 show the surface morphology of coatings deposited at 0.1 wt. %/500 W and 1.0 wt. %/300 W, respectively. The high power, low concentration sample displays prominent drying striations, whereas the low power, high concentration conditions result in a more uniform coating.

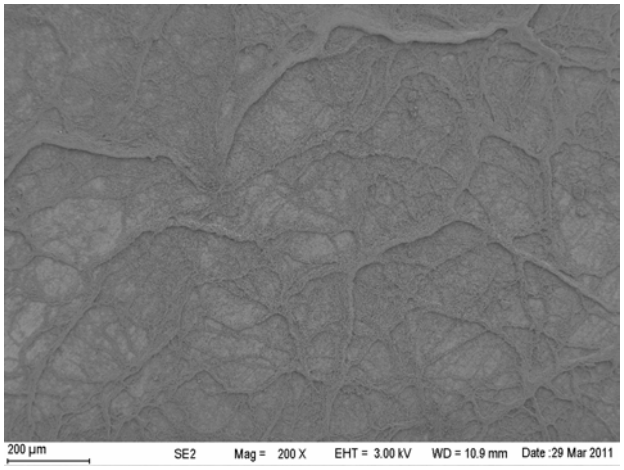

Figure 100. SEM surface image of a typical coating resulting from a boiling nanofluid deposition process using 0.1 wt. % 15nm anatase TiO_2 solution and 500 W power.

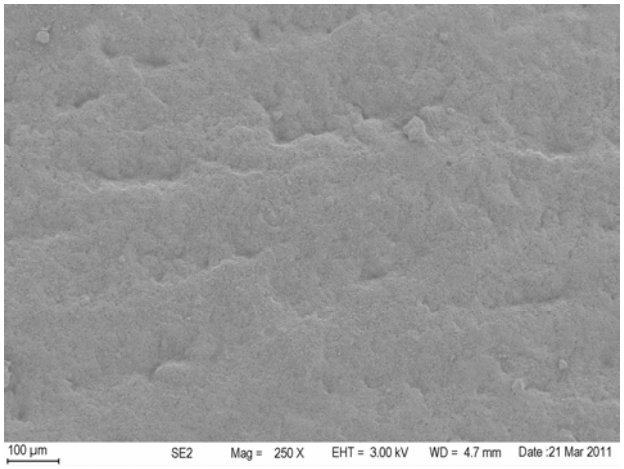

Figure 101. SEM surface image of a typical coating resulting from a boiling nanofluid deposition using 1.0 wt. % 15 nm anatase TiO_2 solution and a 300 W power.

To improve coating adhesion to the substrate the samples were subjected to a pre-oxidation step to produce a thin oxide layer to provide a more favorable substrate for coating deposition. Deposition experiments were then performed using 7 nm anatase TiO_2 in solution for 0.5 wt %. or 1.0 wt. %. It was observed that pre-oxidizing the T91 substrates prior to the boiling deposition process causes only a minor change in the amount of coating transferred to the substrate (Figure 102). The coating morphology is unaffected by the pre-processing treatment.

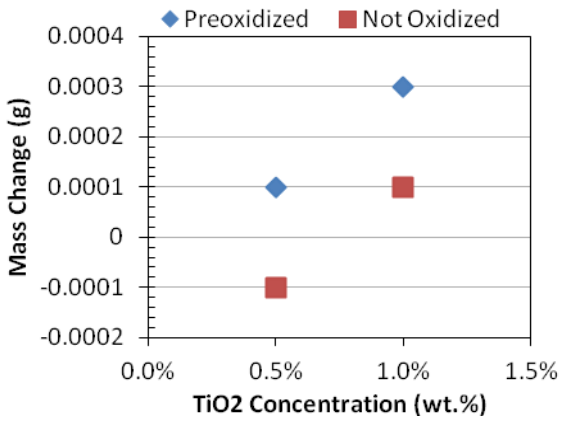

Figure 102. Comparison of the mass change from the coating for pre-oxidized and unoxidized samples.

Experiments were also performed using anatase and rutile powdres of different sizes while other conditions were kept identical (0.5% TiO_2). In general rutile phase resulted higher powder particle density (Figure 103).

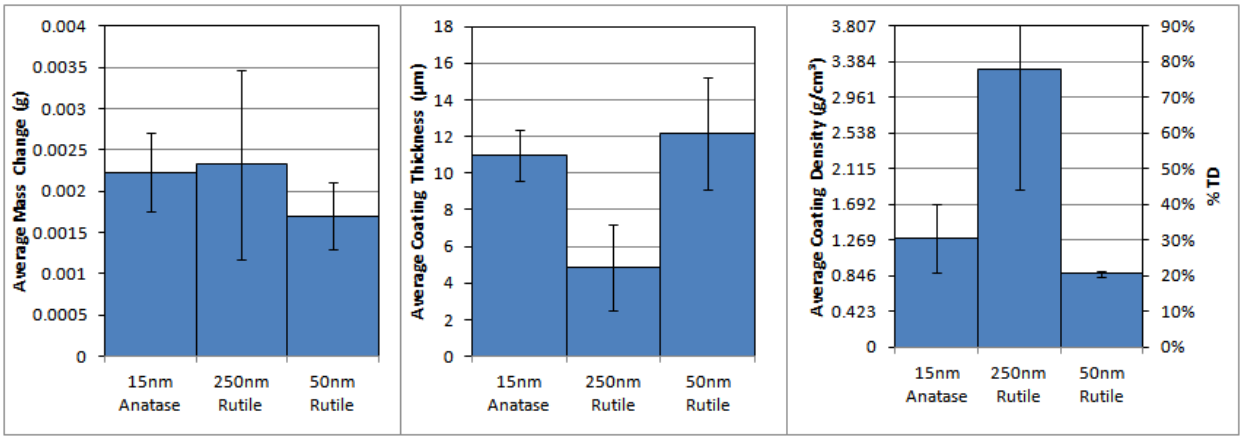

Figure 103. Comparison of the mass change, coating thickness, and calculated coating density for samples coated with a variety of TiO_2 nanoparticle sizes and phases.

Since the nanofluid is synthesized by dispersing a nanopowder into a solvent, surface chemistry should play a significant role in the nanofluid boiling deposition process. To investigate this hypothesis, we conducted depositions using nanofluids made with surface treated TiO_2 nanoparticles. TiO2 nanoparticles surface treated to be hydrophobic and hydrophilic were investigated. The hydrophobic particles were created by a layer of Al_2O_3 combined with fatty acids, while the hydrophilic condition was created by a film of SiO_2. The base TiO_2 used in the hydrophilic/hydrophobic experiments was 50nm in size and of rutile phase. These powders were tested at concentrations of 1.0 wt. % for 10 minutes, and 0.1 wt. % for 25 minutes with a 500 W heating element. To serve as a control, a nanofluid made with 50nm rutile TiO_2 nanopowder from the same manufacturer was tested. The results of the surface chemistry experiment are summarized in Figure 104. It was noted that the results fall in line with expected trends – one does not expect the hydrophobic surface to disperse well when

mixing the nanofluid, or to have a tendency to remain dispersed. Rather, one expects the hydrophobic TiO_2 nanoparticles to agglomerate in solution, while the hydrophilic nanoparticles should disperse more effectively than the uncoated nanoparticles. In the Figure 104 it is noted that the hydrophobic depositions are characterized by significantly less mass deposition, while there is no difference between the control nanofluid and the nanofluid made with a hydrophilic TiO_2 nanoparticles.

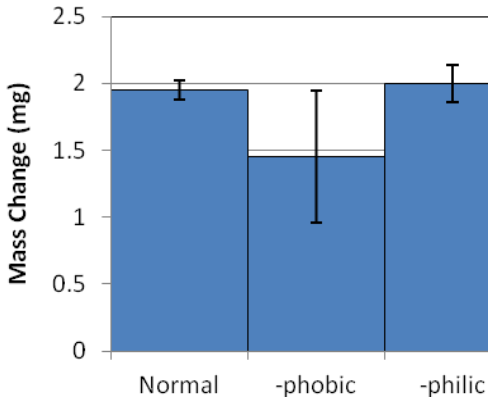

Figure 104. Comparison of the mass change following boiling nanofluid deposition using 50 nm rutile TiO_2.

VIII. References Cited

1. “Sodium Fast Reactor Evaluation: Core Materials”, Cheon, J.S., C.B., Lee and B.O., Lee. 2009, *Journal of Nuclear Materials*, Vol. 392, pp. 324-330.

2. “Ferritic/Martensitic steels for Next-Generation Reactors”, Klueh, R.L. and Nelson, A.T. 2007, *Journal of Nuclear Materials*, Vol. 371, pp. 37-52.

3. “Fuels for Sodium-Cooled Fast Reactors: US Perspective”, Crawford, D.C., Porter, D.L. and Hayes, S.L. 1-3, 2007, *Journal of Nuclear Materials*, Vol. 371, pp. 202-231.

4. “Performance of a Diffusion Barrier under a Fuel-Clad Chemical Interaction”, Kim, J.H., et al., et al. 2009, *Journal of Nuclear Materials*, Vol. 394, pp. 144-150.

5. “Performance of FCCI Barrier Foils for U-Zr-X Metallic Fuel”, Ryu, H.J. and Lee, B.O. 2009, *Journal of Nuclear Materials*, Vol. 392, pp. 206-212.

6. “Application of Electrophoretic and Electrolytic Deposition Techniques in Ceramic Processing”, Boccaccini, A and Zhitomirsky, I. 2002, *Current Opinion in Solid State & Materials Science*, pp. 251-260.

7. “Electrophoretic Deposition Forming of Porous Alumina Memebranes”, Chen, C.Y., Chen, S.Y. and Liu, D.M. 9, 1999, *Acta Materialia*, Vol. 47, pp. 2717-2726.

8. “Electrophoretic Deposition of Zirconia Layers for Thermal Barrier Coatings”, Van der Biest, O., et al., et al. 2006, *J Mater Science*, Vol. 41, pp. 8086-8092.

9. “Electrophoretic Deposition for Fabrication of Ceramic Microparts”, Bonnas, S., Ritzhaupt-Kleissl, H.J. and Haubelt, J. 2010, *Journal of the European Ceramic Society*, Vol. 30, pp. 1159-1162.

10. “Electrophoretic Deposition of Materials”, Van der Biest, O.O. and Vandeperre, L.J. 1999, *Annual Review of Material Science*, Vol. 29, pp. 327-352.

11. “Electrophoretic Deposition from Aqueous Suspensions for Near-Net Shape Manufacturing of Advanced Ceramics and Glasses – Applications”, Tabellion, J and Clasen, R. 2004, *Journal of Materials Science*, Vol. 39, pp. 803-811.

12. “Functionally Graded Ceramic/Ceramic and Metal/Ceramic Composites by Electrophoretic Deposition”, Sarkar, P., Datta, S and Nicholson, S. 1997, *Composites Part B*, Vol. 28, pp. 49-56.

13. “Nickel-Alumina Functionally Graded Materials by Electrophoretic Deposition”, Nagarajan, N. and Nicholson, P.S. 11, 2004, Journal of the American Ceramic Society, Vol. 87, pp. 2953-2057.

14. “Theory of Cast Formation in Electrophoretic Deposition”, P.M., Biesheuvel and Verweij, H. 6, 1999, *Journal of the American Ceramic Society*, Vol. 82, pp. 1451-55.

15. “A Review on Fundamentals and Applications of Electrophoretic Deposition (EPD)”, Besra, L., Liu, M. 2007, *Progress in Materials Science*, Vol. 52, pp. 1-61.

16. “Effects of pH and Particle Size on the Processing of and the Developement of Microstructure in Allumina-Zirconia Composites” Bleier, A. and Westmoreland, C.G. 12, 1991, *Journal of the American Ceramic Society*, Vol. 74, pp. 3100-3111.

17. Hunter, Robert J. Zeta, *Potential in Colloid Science: Principles and Applications*. London and New York : Academic Press, 1981. 0123619602.

18. “Zeta Potential, An Introduction in 30 Minutes”, Malvern Instruments.

19. “The Mathematical Expression for Kinetics of Electrophoretic Deposition and the Effects of Applied Voltage”, Ciou, S.J., Fung, K.Z. and Chiang, K.W. 2007, *Journal of Power Sources*, Vol. 172, pp. 358-362.

20. “Sol Electrophoretic Growth of Oxide Nanostructures - Sythesis, Properties, and Modeling”, Limmer, S.J., University of Washington, 2004, PhD Thesis.

21. “The Influence of pH on Particle Packing in YSZ Coating Electrophoretically Deposited from a Non-Aqueous Suspension”, Xu, H., Shapiro, I.P. and Xiao, P. 2010, *Journal of the European Ceramic Society*, Vol. 30, pp. 1105-1114.

22. “Preparation of Yttria-Stabilized Zirconia (YSZ) Films on La0.85Sr0.15MnO3 (LSM) and LSM-YSZ Substrates Using an Electrophoretic Deposition (EPD) Process”, Chen, F. and Liu, M. 2001, *Journal of the European Ceramic Society*, Vol. 21, pp. 127-134.

23. “A Study on the Electrophoretic Deposition of 8YSZ Coatings Using Mixture of Acetone and Ethanol Solvents”, Aruna, S.T. and Rajam, K.S. 2008, *Materials Chemistry and Physics*, Vol. 111, pp. 131-136.

24. “TiO_2 Coatings on Silicon Carbide and Carbon Fibre Substrates by Electrophoretic Deposition”, Boccaccini, A.R., Karapappas, P. and Marijuan, J.M., Kaya, C. 2004, *Journal of Materials Science*, Vol. 39, pp. 851-859.

25. “Structural and Functional Thick Ceramic Coatings by Electrophoretic Deposition”, Kaya, C., et al., et al. 2005, *Surface and Coating Technology*, Vol. 191, pp. 303-310.

26. “Microstructure of Nanocrystalline TiO_2 Films Produced by Electrophoretic Deposition on Ti06Al-7Nb Alloy”, Moskalewicz, T., Czyrska-Filemonowicz, A. and Boccaccini, A.R. 16-17, 2007, *Surface and Coatings Technology*, Vol. 201, pp. 7467-7471.

27. “Characterization of TiO_2 Nanoparticle Suspensions for Electrophoretic Deposition”, Santillan, M.J., et al., et al. 2008, *Journal of Nanoparticle Research*, Vol. 10, pp. 787-793.

28. “The Influence of Suspension Composition and Deposition Mode on the Electrophoretic Deposition of TiO_2 Nanoparticle Agglomerates”, Dor, S., et al., et al. 2009, *Colloids and Surfaces A: Physicochemical and Engineering Aspects*, Vol. 342, pp. 70-75.

29. “Electrophoretic Deposition of Ceramic Nanoparticles”, Wu, K. and Zhitomirsky, I. 2010, *International Journal of Applied Ceramic Technology*, pp. 1-8.

30. “Electrophoretic Deposition of YSZ Electrolyte Coatings for SOFCs”, Xu, Z., et al., et al. 3, 2007, *Fuel Cells Bulletin*, Vol. 2007, pp. 12-26.

31. “Electrophoretic Deposition of Electrolyte Materials for Solid Oxide Fuel Cells”, Zhitomirsky, I. and Petric, A. 2004, *Journal of Materials Science*, Vol. 39, pp. 825-831.

32. “Preparation of YSZ Film by EPD and its Application in SOFCs”, Jia, L., et al., et al. 2006, *Journal of Alloys and Compounds*, Vol. 424, pp. 299-303.

33. “Fabrication of Bilayered YSZ/SDC Electrolyte film by Electrophoretic Deposition for Reduced-Temperature Operating Anode-Supported SOFC”, Matsuda, M., et al., et al. 2007, *Journal of Power Sources*, Vol. 165, pp. 102-107.

34. “Direct EPD of YSZ Electrolyte Film onto Porous NiO-YSZ Composite Substrate for Reduced-Temperature Operating Anode-Supported SOFC”, Matsuda, M., et al., et al. 1, 2005, *Electrochemical and Solid-State Letters*, Vol. 8, pp. A8-A11.

35. “Electrophoretic Deposition for Fabrication of TSZ Electrolyte Film on Non-Conducting Porous NiO-YSZ Composite Substrate for Intermediate Temperature SOFC”, Hosomi, T., Matsuda, M. and Miyake, M. 2007, *Journal of the European Ceramic Society*, Vol. 27, pp. 173-178.

36. “Electrophoretic Deposition of YSZ Particles in Non-Conducting Porous NiO-YSZ Substrates for Solid Oxide Fuel Cell Applications”, Besra, L., Compson, C. and Liu, M. 10, 2006, *Journal of the American Ceramic Society*, Vol. 89, pp. 3003-3009.

37. “Electrophoretic Deposition on Non-Conducting Substrates: The Case of YSZ Film on NiO-YSZ Composite Substrates for Solid Oxide Fuel Cell Application”, Besra, L. and Compson, C. Liu, M. 2007, *Journal of Power Sources*, Vol. 173, pp. 130-136.

38. “Application of Electrophoretic Deposition Technique to Solid Oxide Fuel Cells”, Negishi, H., et al., et al. 5, 2000, *Journal of The Electrochemical Society*, Vol. 147, pp. 1682-1687.

39. “Colloidal Processing of a Mullite Matrix Material Suitable for Infiltrating Woven Fibre Preforms Using Electrophoretic Deposition”, Boccaccini, A.R., et al., et al. 1996, *Journal of the European Ceramic Society*, Vol. 16, pp. 1319-1327.

40. “Electrophoretic Deposition Forming of Nickel-Coated-Carbon-Fiber-Reinforced Borosilicate-Glass-Matrix Composites”, Kaya, C., Boccaccini, A.R. and Chawla, K.K. 8, 2000, *Journal of the American Ceramic Society*, Vol. 83, pp. 1885-88.

41. “Fabrication of Ceramic Composite Coatings Using Electrphoretic Deposition, Reaction Bonding and Low Temperature Sintering”, Wang, Z., Shemilt, J. and Xiao, P. 2002, *Journal of the European Ceramic Society*, Vol. 22, pp. 183-189.

42. “Fabrication of Dense Zirconia Electrolyte Films for Tubular Solid Oxide Fuel Celss by Electrophoretic Deposition”, Basu, R.N., Randall, C.A. and Mayo, M.J. 2001, *Journal of the American Ceramic Society*, Vol. 84, pp. 33-40.

43. “Electrophoretic Deposition of Vanadium Oxide and the Radiation Stability of TiN Coatings for Mitigating Fuel Cladding Chemical Interactions”, Shea, J., M.S. Thesis, Nuclear Engineering and Engineering Physics, University of Wisconsin - Madison. 2008.

44. “V2O5 Nanoparticles Obtained from a Synthetic Barandite-like Vanadium Oxide: Synthesis, Characterization and Electrochemical Behavior in an Ionic Liquid”, Menezes, W.G., et al., et al. 2009, *Journal of Colloid and Interface Science*, Vol. 337, pp. 586-593.

45. “Electrophoretic Deposition of Metals”< Pearlstein, F., Wick, R. and Gallaccio, A. 7, 1963, *Journal of the Electrochemical Society*, Vol. 110, pp. 843-846.

46. “Electrophoretic Deposition: A Versatile Coating Method”, Gutierrez, C.P., Mosley, J.R. and Wallace, T.C. 1962, *Journal of the Electrochemical Society*, Vol. 109, pp. 923-927.

47. “A Highly Stable Nonaqueous Suspension for the Electrophoretic Deposition of Powdered Substances”, Mizuguchi, J., Sumi, K. and Muchi, T. 9, 1983, *Journal of the Electrochemical Soci*ety, Vol. 130, pp. 1819-1825.

48. “Production and Properties of Seamless Modified 9Cr-1Mo Steel Boiler Tubes”, Sasaki, T., et al., et al. September 1991, *Kawasaki Steel Techinical Report*, pp. 78-87.

49. J. J. Duderstadt, L. J. Hamilton, *Nuclear Reactor Analysis*, John Wiley and Sons,

Chapter 12, (1976) 467-514.

50. “Advance Burner Test Reactor Preconceptual Design Report” Y.I. Chang, P.J. Finck, and C. Grandy, Nuclear Engineering Division, Argonne National Lab (2006).

51. “Fast Reactor Fuel Type and Reactor Safety Performance”, R. Wigeland and J. Cahalan, *Proceedings of Global 2009*, Paris, France, September 6-11, 2009 Paper 9445.

52. Generation IV Nuclear Energy Systems Idaho National Lab Technical Documents, Appendix 5:Sodium-Cooled Fast Reactor, (2005) A5-1-A5-12.